MOLECULAR DYNAMICS SIMULATION ON THE DEFORMATION BEHAVIOR OF COPPER(CU)/ZIRCONIUM(ZR) METALLIC GLASS UNDER MULTIAXIAL STRESS STATES

CUI WANG

(B.Eng., Harbin Institute of Technology)

A THESIS SUBMITTED

FOR THE DEGREE OF DOCTOR OF PHILOSOPHY

DEPARTMENT OF MATERIALS SCIENCE & ENGINEERING

NATIONAL UNIVERSITY OF SINGAPORE

2016

DECLARATION

I hereby declare that the thesis is my original work and it has been written by me in its entirety. I have duly acknowledged all the sources of information which have been used in the thesis.

This thesis has also not been submitted for any degree in any university previously.

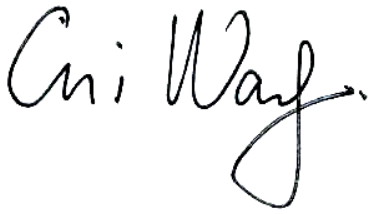

Cui Wang
10 August 2016

Acknowledgements

First and foremost, I would like to express my sincerest gratitude to my supervisor Professor Li Yi and Associate Professor Daniel John Blackwood, for their invaluable wisdom, guidance and encouragement through all these four years. Professor Li Yi is an excellent advisor, successful scientist and passionate person. His patient teaching guides me to think logically, critically and professionally, and I have benefited tremendously from it. It has been a great honor to study in this group.

I would like to thank my group members, Dr. Pan Jie, Dr. Wang Yinxiao, Dr. Aaron Ong and Mr. Zuo Lianyong, for their continuous help, support, and insightful suggestions for my research. It is wonderful to work with these people.

I would like to extend my gratitude to the staff members and laboratory technologists of the Materials Science and Engineering Department for their kindness and help. I would like to thank National University of Singapore for the financial support.

I am also very grateful to my parents and my fiancée He Xi for their endless support, understanding and love throughout all my years of study and through the process of researching.

Table of Contents

Summary

Molecular dynamics (MD) simulation has been performed based on the embedded atom method (EAM) potential using the Large-scale Atomic/Molecular Massively Parallel Simulator (LAMMPS) codes, in order to investigate the deformation mechanism and atomic-level structural evolution in the Cu-Zr metallic glasses (MGs) under multiaxial stress states.

For this purpose, $Cu_{64}Zr_{36}$ metallic glass was chosen as a model system. The melt-quenching process of this glass was successfully simulated and structural analysis revealed that a fully amorphous structure was formed. The cooling rate effect on the short-range-order (SRO) structure of the simulated glass was studied and a relatively slow quenching rate of 5×10^{10}K/s stood out for it can create a more ordered short-range structure.

Based on the small configuration containing 13,500 atoms, large cylinder samples containing ~600,000 atoms were constructed by replications of the small configurations. Unnotched samples with a diameter of 20 nm in X- and Y- directions and length of 30 nm in Z- direction were built-up as references. Notched samples with notch depth from 1 to 5 nm, in an ascending order of 1 nm were created by eliminating atoms and were adopted to produce the multiaxial stress states in the center of the notch. The focus was put on the

notched samples under uniaxial tensile simulation to investigate the effect of multiaxial stress state on the deformation mechanism of CuZr metallic glass. Different notch depths, tensile strain rates and loading temperatures were treated as key elements in determining the mechanical behaviors of MG.

A Voronoi volume annihilation phenomenon was monitored on deep-notched samples during the plastic deformation process. This observation is contrary to the previous Voronoi volume generation inside the shear band on unnotched samples associated with strain softening and structure disordering. Instead, in the center of the deep-notched samples, significant local shear strain alleviation and Voronoi volume reduction was demonstrated, accompanied by the recovery of Cu-centered full-icosahedra (FI) fraction and decrease in local temperature.

In order to investigate the strain rate effect on the deformation behavior of CuZr MGs, cylindrical samples with and without notch were applied under different strain rates. With the increase in strain rate, an increase in yielding stress was demonstrated and cooperative shear model (CSM) theory was adopted to well explain such a phenomenon. In the deep-notched samples, the high-strain-rate could lead to an alleviated reduction of cross sectional area. More importantly, local shear strain alleviation, the annihilation of Voronoi volume, the recovery of Cu-centered FI fraction and decrease in local temperature during the plastic deformation were found to only exist under low-strain-rates. While under high-

strain-rates, these indications of structure ordering process could diminish or vanish. It was proved that rapid loading can cause the rate of free volume generation to be higher than its annihilation rate assisted by multiaxial stress state.

Furthermore, the effect of temperature on the deformation behavior of $Cu_{64}Zr_{36}$ MGs was investigated. A decrease in engineering yielding stress and structure softening phenomena were observed when temperature was increased. The mechanical properties of samples under different temperatures were proved to exhibit good agreement with CSM theory. The results showed that in the center of the deep-notched samples, only a low loading temperature can lead to the local shear strain alleviation, Voronoi volume annihilation and Cu-centered FI fraction recovery. While a high loading temperature can only result in a structural disordering process as the free volume generation rate surpassed its annihilation rate.

The results presented in this thesis have revealed the atomic-level mechanism and structural evolution of CuZr metallic glass under multiaxial stress state. MD simulation is demonstrated to well explain the densification and strain hardening phenomena found in previous experimental studies. This work enriches our understanding of the structure-property relationship of MGs.

List of Tables

List of Figures

List of Abbreviations

MGs	Metallic glasses
MD	Molecular dynamics
EAM	Embedded atom method
LAMMPS	Large-scale Atomic/Molecular Massively Parallel Simulator
CSM	Cooperative shear model
FI	Full-icosahedra
BMGs	Bulk metallic glasses
GFA	Glass-forming ability
SRO	Short-range-order
MRO	Medium-range-order
DRPHS	Dense random packing of hard spheres
SCD	Stereo-chemically defined
DCP	Dense cluster packing
ST	Shear transformation
STZs	Shear transformation zones
Tg	Glass transition temperature
NVT	Constant number of particles-volume-temperature
FDT	Fluctuation-dissipation-theorem
DFT	Density-functional-theory
MEAM	Modified embedded atom method
F-S	Finnis-Sinclair potential

SMA-TB	Second-moment approximation of tight-binding potential
PBC	Periodic boundary condition
GPL	GNU Public License
PDF	Pair distribution function
CN	Coordination number
TEM	Transmission electron microscope
XRD	X-ray diffraction
VMD	Visual Molecular Dynamics
OVITO	Open Visualization Tool

Chapter 1 Introduction

Amorphous metals are materials having a random arrangement of atoms. Unlike common crystalline metals whose atomic structure can be easily described in terms of lattice constants and crystal symmetries, amorphous metals lack long-range atomic periodicity [1]. A sub-class of this type of material is called metallic glasses (MGs) which production involves rapidly quenching an equilibrium liquid to a certain temperature (glass transition temperature) at which the sample becomes configurationally frozen [2]. Due to this unusual configuration compared to their crystalline counterparts, MGs show very unique properties, such as superior mechanical strength and hardness, reduced sliding friction, improved corrosion resistance, and low magnetic energy loss [3-6]. Since its first synthesis in the 1960s [7], MGs have attracted broad attentions. In the early 1990s, glassy systems based on multi-component alloys were discovered to give rise to the bulk metallic glasses (BMGs) [8, 9]. Despite the intense studies into the BMGs, some key issues still remain unresolved, such as understanding of local atomic configuration [10, 11], the relationship between local atomic structure and their plastic behavior [12-14] and the effect of strain rate and temperature on the deformation mechanisms [15]. In this chapter, an overview of MGs is briefly provided, including their history and wide applications. Previous studies on the atomic structure and deformation mechanisms of metallic glasses are presented. Finally, remaining issues, the

motivations and objective of this thesis are listed.

1.1 Overview of metallic glasses

1.1.1 The history of the development of metallic glasses

The formation of metallic glass from liquid involves inhibiting the formation of the equilibrium crystalline phase which requires an adequately high cooling rate, thereby freezing the liquid configuration in the solid state and remaining disordered [16]. This assumption was first experimentally proved by scientists at Caltech in 1959 [17]. By using splat quenching, they successfully fabricated a glassy alloy with a composition of $Au_{75}Si_{25}$ [17]. According to the X-ray diffraction pattern, diffraction peaks corresponding to the crystalline structure had disappeared and the formation of a highly disordered arrangement of the atoms was observed. Since then, rapid research progresses have been made in search of new MGs and a variety of MGs with various alloy compositions soon followed [5]. However, these glass-forming systems all required cooling rate of $10^5 \sim 10^7$ K/s, which is not easy to achieve even in laboratory conditions. The inventions of melt spinning method accelerated the discovery of MGs[18]. This technique can quench liquid alloys to ribbons with $10 \sim 50$ μm in thickness at a cooling rate of $10^3 \sim 10^6$ K/s. During the early age of studies on MGs, because of the rapid cooling rates needed to produce MGs, sample dimensions have been limited to ribbons and thin sheets, therefore limiting their wide applications.

In the early 1980s, several multi-component alloys such as Pd-Cu-Si and Pd-Ni-P have been found to exhibit a considerably lower critical cooling rate of ~ 10 K/s [19-22] for glass formation. These alloy systems with extraordinary glass-forming ability (GFA) allow formation of metallic glass samples up to bulk sizes of ~ 10 mm in thickness. This new category of amorphous metal alloys called bulk metallic glasses was soon developed and many new systems have been found such as Zr-Al-Ni-Cu [23, 24]. In 1993, scientists Johnson and Peker from Caltech reported a superior multicomponent bulk metallic glass with a composition of $Zr_{41.2}Ti_{13.8}Cu_{12.5}Ni_{10.0}Be_{22.5}$, which is famous as the first commercially available metallic glass product named Vitreloy [9]. Nowadays, numerous MGs with different compositions have been fabricated and the intense studies into their properties still continue. Table 1.1 and Table 1.2 list some typical MGs based on their constituent elements and binary prototypes.

Table 1.1 Classification of common constituent elements in MGs

Abbreviation	*Description*	*Examples*
AM	Alkali and alkaline-earth metals (group IA and IIA)	Mg, Ca, Be*
SM	Semi- or simple metals (Group IIIA and IVA)	Al, Ga
ETM	Early transition metals (Group IVB and VIIB)	Ti, Zr, Hf, Nb, Ta, Cr, Mo, Mn
LTM	Late transition metals (Group IB, IIB and VIIIB)	Fe, Co, Ni, Cu, Pd, Pt, Au, Zn
RE	Rare-earth metals	
	Lanthanides + Sc, Y	
-	Actinide metals	U
NM	Metalloids and nonmetals	B, C, P, Si, Ge

*Although the element Be is an AM in this classification, its role in metallic glass formation is special, associated with its small size. (Reprinted from Cheng and Ma [25] with permission from Elsevier.)

Table 1.2 Classification of typical MGs based on binary prototypes

Prototype	*Base metal*	*Examples*
LTM + NM	LTM	Ni-P, Pd-Si, Au-Si-Ge, Pd-Ni-Cu-P, Fe-Cr-Mo-P-C-B
ETM + NM	ETM	Ti-Si
ETM + LTM	ETM or LTM	Zr-Cu, Ni-Zr, Ni-Nb, Ti-Ni, Zr-Cu-Ni-Al, Zr-Ti-Cu-Ni-Be
RE + LTM	RE	Gd-Fe
SM + RE	SM or RE	Al-La, Ce-Al, Al-La-Ni-Co, La-(Al, Ga)-Cu-Ni
AM + LTM	AM	Mg-Cu, Ca-Mg-Zn, Ca-Mg-Cu
U + LTM	U	U-Co

(Reprinted from Cheng and Ma [25] with permission from Elsevier.)

1.1.2 Applications of MGs

Over the last decades, MGs have developed from a laboratory observation to an extensive class of alloys. Owning to their exceptional mechanical, physical and magnetic properties, the application of MGs has been extended to various fields for industrial and military purposes.

Currently, one of the most important applications of MGs uses the low magnetization loss of some ferromagnetic metallic glasses. Their unique magnetic properties can be quite useful in the production of high efficiency transformers [26, 27]. These amorphous metal transformers have been proved to have open circuit losses 70~80% less than the traditional silicon steel ones. In developing countries, such as China and India, these kinds of transformers have now been widely used, and are estimated to save 25~30 TWh electric energy every year, as well as an annual reduction in carbon dioxide release up to twenty to thirty million tons [28].

Other applications of BMGs into the market use their superior mechanical properties. One example presents in the sporting field such as golf club [5, 29], where the high elastic limit means they do not deform permanently, and so are able to store and return more energy to the golf ball, allowing it to fly further. Other researchers in US have developed high strength and lightweight metallic glass tank-armor penetrator rounds in order to substitute currently used depleted

uranium penetrator without sacrificing the reliability [30]. In 2001, NASA launched the Genesis spacecraft, equipped with five circular passive collector arrays with a diameter of 1 m coated with amorphous Zr-Nb-Cu-Ni-Al alloys, aiming to absorb the noble gases of He and Ne in solar wind [31]. For biomaterial area, scientists have found that some MGs can exhibit excellent biocompatible, non-allergic properties while at the meantime, have superior strength, which can be used as an artificial finger joint [32].

Table 1.3 lists some representative metallic glasses with their properties and applications. In the near future, metallic glasses will play a more and more important role in our daily life as new discoveries in this field are being made by a deeper understanding of this class of material.

Table 1.3 Representative metallic glasses, their properties and applications

Metallic	*Salient properties*	*Potential applications*
Zr-Ti-Cu-Ni-	High glass-forming ability	Molding, structural components
Fe-Co-Zr-Si-C	Soft ferromagnetism	Transformer cores
Co-Si-P-Fe-Ni	High hardness and wear resistance	Coatings
Ce-Al-Cu	Low glass-transition temperature	Metallic plastics
Pd-Ag-P-Si-	High strength-toughness	Damage-tolerant materials
Mg-Zn-Ca	Biodegradable	Bone implants

(Reprinted from Greer at al. [13] with permission from Elsevier.)

1.2 Atomic-level structure

Due to the absence of long-range-order structure and the variety of possible structural configuration that amorphous metals can adopt, one of the long-standing issues in the metallic glasses field is their atomic-level structure. Different from crystalline metals where the atomic arrangement is strictly periodic, metallic glasses do not have translational or orientational order. However, short-range order (SRO) commonly occurs in MGs. Compared to that in the liquid state where SRO can exist but thermal energy and entropy can enable the atomic motion and breakdown of SRO, the atoms in MGs are for the most part frozen in position so that the SRO can be reserved. Additionally, a certain degree of medium-range order (MRO) exists as well [33]. Many simulation studies [34-36] and experimental works [33, 37-40] have been carried out to support the existence of both SRO and MRO. Understanding the atomic structure will be vital to correctly describe the mechanical behavior of MGs as their structures directly determines their mechanical properties. Over the years, several models [33, 41-43] have been proposed to describe the atomic structure of MGs including dense-random packing of hard spheres model [42], stereo-chemically defined model [41] and dense cluster packing model [44-46].

1.2.1 Dense random packing of hard spheres model

In the early history of amorphous metals studies, Bernal proposed the widely

used dense random packing of hard spheres (DRPHS) model to describe the structure of amorphous solids [42]. This model is purely based on the spatial arrangement of hard spheres according to the ratio of their atomic radii and ignores any chemical effects on atomic packing. DRPHS model fairly explains the radial distribution functions in MGs and successfully describes the splitting feature of the second peak in the radial distribution function, which is the significant feature of MGs [47, 48]. Despite its relative simplicity, this DRPHS model, provides a satisfactory description of monoatomic systems and alloys with comparable atomic sizes.

However, the disadvantages of this model are obvious. First, the assumption of hard spheres representing realistic atoms cannot be true for all alloy systems. Secondly, DRPHS model cannot match metallic glass systems which often contain atoms with significant size differences, such as metal-metalloid glasses and multi-component glassy systems. Moreover, the SRO and MRO that are frequently observed in many binary MGs cannot be explained by using this model [35, 42].

1.2.2 Stereo-chemically defined model

The stereo-chemically defined (SCD) model was proposed by Gaskell [41, 44]. He assumed that the local atomic arrangement in amorphous alloys shares the same motif as their crystalline compound counterparts with similar composition.

These unique local structures are then interconnecting with each other with an edge or face sharing arrangement to form a continuous random network. The SCD model first establishes a realistic connection between the short-range structure and the medium-range structure of MGs and shows a reasonable agreement with neutron scattering data for metal-metalloid glasses. However, in the case of metal-metal glasses, the applicability of this model was not confirmed [4].

1.2.3 Dense cluster packing model

The dense cluster packing (DCP) model was proposed by Miracle in 2004 [45, 46, 49] based on the previous studies. He suggested that solute-centered quasi-equivalent clusters are the local structural motif in solute lean metallic glasses, which is defined in terms of a given atomic ratio and used as a local representative structural element in MGs. A medium-range structure is generated by packing the solute centered clusters (α) in face centered cubic (fcc) configuration which only extend to a few cluster diameters (~ 1 nm) due to internal strains packing frustration. As illustrated in Figure 1.1, two additional solute sites with different sizes exist in the fcc lattice: the octahedral site (β) and the tetrahedral site (γ). The preferred coordination number (CN) and size of the solute-centered cluster is determined by the size ratio (R) relative to the solvent (Ω) for each solute (α, β, γ). The final efficient packing of solute-centered

clusters can be designated as $<CN_{\alpha}, CN_{\beta}, CN_{\gamma}>_{fcc}$ [46]. This model can accurately predict the number of solute atoms in the first coordination shell. Also, it convincingly reproduces the atomic configurations in a wide range of metallic glasses.

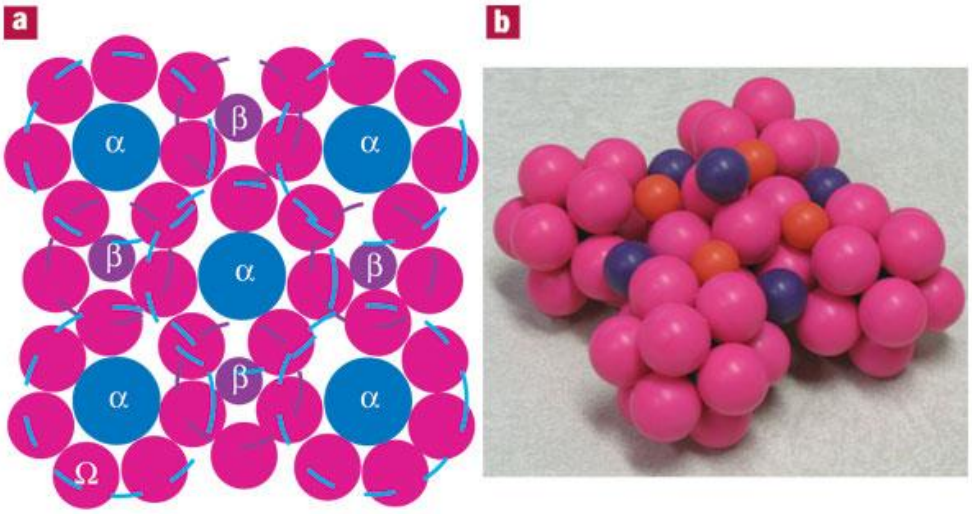

Figure 1.1 (a) Two-dimensional representation of the dense cluster-packing structure. (b) A portion of a cluster unit cell of a <12, 10, 9> model system. [46] (Reprinted with permission from Nature Publishing Group)

A refined model was proposed by Sheng et al. in 2006 which absorbs the structure concepts proposed in the previous models [33]. As shown in Figure 1.2, their model indicated that a number of differently coordinated solute-centered quasi-equivalent clusters would form according to the strong chemical orderings. The intra-cluster packing presents topological SRO, and efficiently forms coordination polyhedra packed for the specific atomic radius ratios [43, 49, 50]. To efficiently fill the 3D space, the inter-cluster connection within the metallic glass adopts dense random packing arrangements of the clusters via

vertex sharing, edge sharing and face sharing schemes, which constitute different types of MRO [33]. The dominant MRO is that of dense random packing of clusters with icosahedral-like character. This model has been proved to successfully describe several binary MGs [38] and provide a possible way to analyze multi-component MGs.

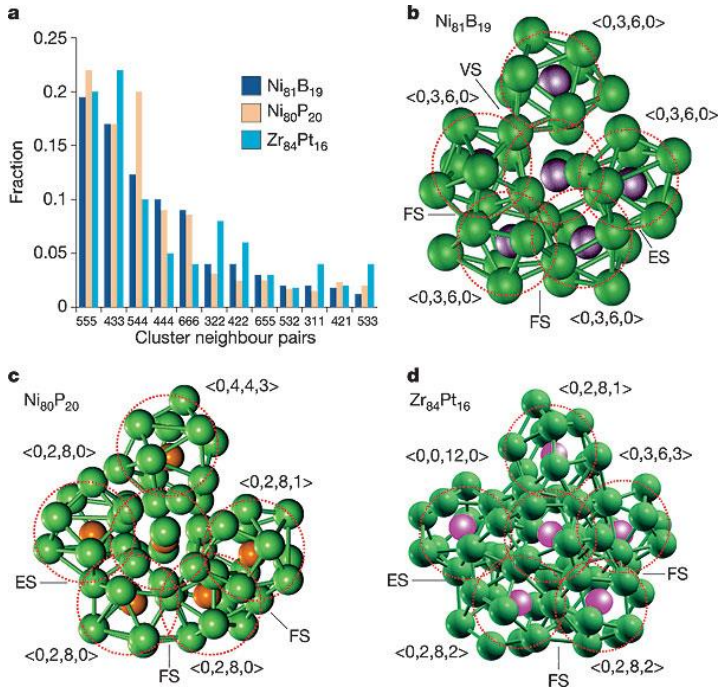

Figure 1.2 Solute-centered clusters in several binary MGs and their efficient packing characterized fivefold and icosahedral-like feature. [33] (Reprinted with permission from Nature Publishing Group.)

These two idealized cluster packing models have provided insights on the SRO and MRO in MGs. However, the dense packing of single-solute centered clusters can only be used to describe the structure of alloys with a low solute concentration [37]. Furthermore, these packing schemes will break down beyond a length scale of a few clusters. The realistic structural picture of MGs

still remains somewhat a mystery and more study will be needed in the future to better describe the structural features among amorphous alloys.

1.2.4 Atomic structure of Cu-Zr metallic glasses

Cu-Zr binary alloy system, with a good GFA over a wide range of composition from $Cu_{30}Zr_{70}$ to $Cu_{70}Zr_{30}$, has received much attention recently [51-53]. Since the Cu-Zr metallic glass system is studied in this thesis, it is necessary to address the detailed description of the structure of CuZr system.

First of all, Cu and Zr atoms have different atomic size, therefore, CuZr MGs with different composition would exhibit different structures. Many experiments [54-57] have proved that the mass/atomic density of Cu-Zr MGs with various compositions roughly follows the rule of mixtures, meaning that their density line as a function of Cu/Zr contents is roughly parallel to the density line of their crystalline alloy counterparts. However, a recent experiment performed by Li et al. [58] detected that there exist subtle deviations of the density from the linear density line. By using microcantilevers and a combinatorial deposition method, they were able to find three density peaks which correspond to the three compositions with the best GFA in the Cu-Zr binary system, as shown in Figure 1.3. This interesting finding suggests that at these three particular composition, special atomic-level structures can be formed.

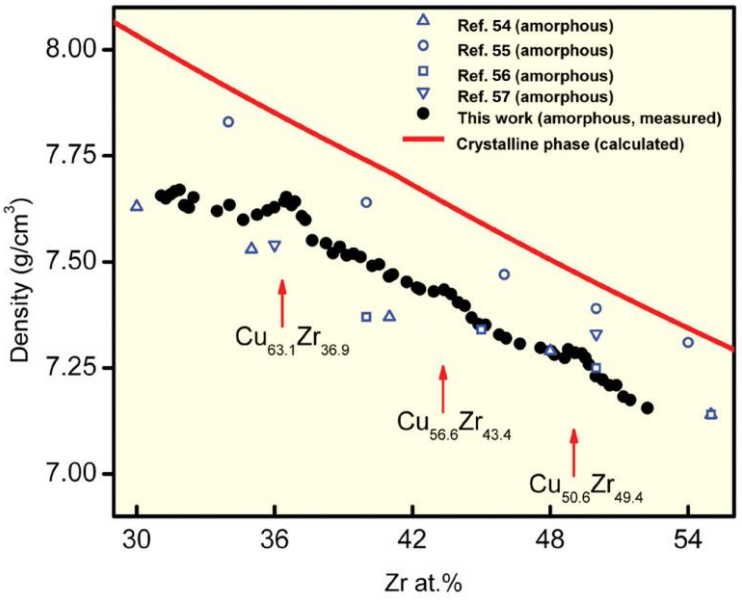

Figure 1.3 Density plot for different compositions in the binary Cu-Zr system and the density data for Cu-Zr metallic glasses reported in the literatures ([54-57]) [58]. (Reprinted with permission from The American Association for the Advancement of Science.)

Others have used partial CNs examination through neutron diffraction and XRD to further investigate the composition dependence of Cu-Zr MG structures [59, 60] and found that the composition dependence in Cu-Zr MGs is consistent. The same trend is also proved by Cheng et al. [34] by using MD simulation method, as shown in Figure 1.4. The partial coordination numbers of Cu-Cu and Zr-Cu pair increase with increasing the Cu content; while the CNs of Cu-Zr and Zr-Zr pairs decrease. Moreover, Ma et al. [60] further found that with the given partial CNs, the packing around Cu atoms can nearly achieve the highest possible packing efficiency. However, the packing around Zr is less efficient. Such results suggest that the atomic structure of Cu-Zr MGs can be best illustrated from the view of Cu-centered clusters.

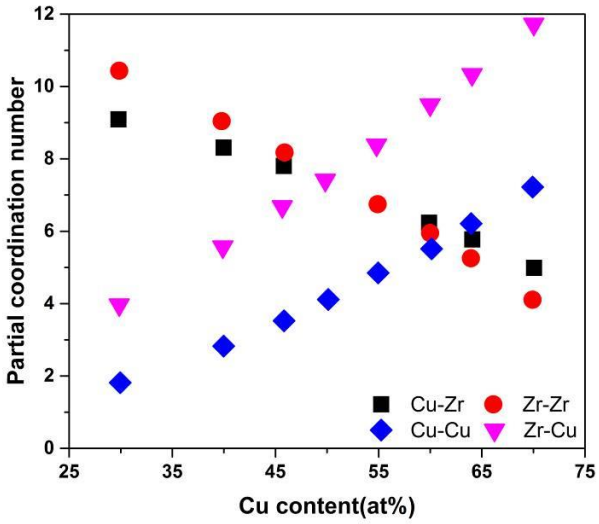

Figure 1.4 Cu content effect on the Partial CNs for MD simulated Cu-Zr MGs. [25] (Reprinted with permission from Elsevier.)

Additional information related to the atomic structure of Cu-Zr MGs can be obtained by conducting Voronoi method analyzes [34, 36, 61]. As proved by Cheng et al. [34, 62], for the short-range structure, Cu-centered five-edged faces polyhedra clusters have been found to be the dominant topological feature in the Cu-Zr system. The fraction of these dominant cluster types can approach to nearly 80% of all Cu atoms. As illustrated in Figure 1.5, from Zr-rich part to Cu-rich part, the CN gradually changes and the dominant Voronoi polyhedra also change. Among all the popular polyhedra around Cu atom, the Cu-centered full-icosahedra (FI), with a Voronoi index of <0,0,12,0>, appears to be special. The increase in their fraction with increasing Cu constituent is much more drastic than other types of polyhedra, as illustrated in Figure 1.5. This Cu-centered FI has been found to have many superior properties such as high

packing density [63], low configurational enthalpy and entropy [36], high shear resistance and lower atomic mobility [34]. On the other hand, the behavior of the Zr-centered packing environment is rather featureless and their distribution of polyhedra types is broad and no evidence of dominant types of polyhedra [34]. This again proves that it is better to examine the Cu-centered clusters to understand the atomic structure of Cu-Zr MGs.

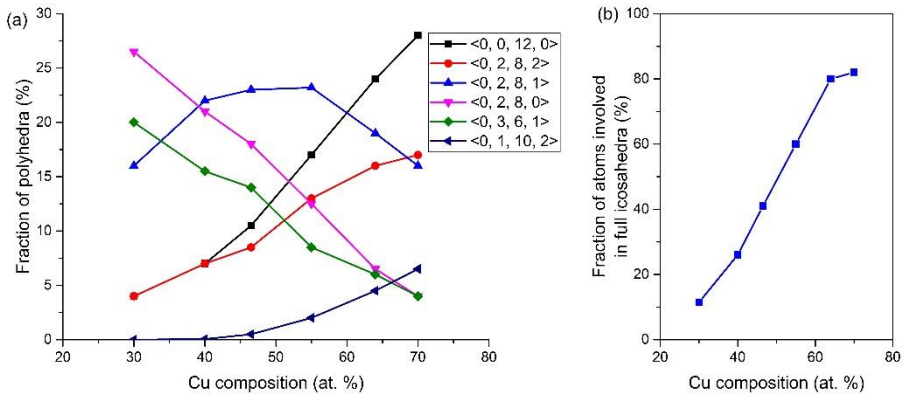

Figure 1.5 (a) Fraction of different types of polyhedra in Cu_xZr_{100-x} metallic glass system. (b) Fraction of atoms involved in full-icosahedra depended on composition. [62] (Reprinted with permission from Elsevier.)

For the medium-range correlation of Cu-Zr binary system, it has been recently found by Li et al. [37] that the distribution of Cu-centered FI in the metallic glass is not completely random. Instead, these can connect with each other to form a string-like network of interpenetrating FI-clusters to play a significant role during the deformation process of this metallic glass.

1.3 Plastic deformation of metallic glasses

Compared to traditional crystalline materials, metallic glasses exhibit excellent fracture strength. However, the lack of plasticity at room-temperature before failure hugely limits their wider applications [64, 65]. Over the last twenty years, a few approaches have been attempted in order to enhance the toughness and plasticity of MGs, including increasing Poisson's ratio [66, 67], introduction of microstructural heterogeneities [68-71], and intake of free volume [72, 73]. However, due to the intrinsic fragility that MGs possess, they are still generally considered to be fragile materials. Enhancing the plasticity of MGs would greatly enlarge their applied range. Therefore, understanding the plastic deformation behavior of MGs will be vital to our knowledge of metallic glasses.

1.3.1 General aspects

Unlike normal crystalline metallic materials whose deformation is usually driven by the movement of dislocations, shear banding with large plastic strain is known as the dominant plastic deformation mode for MGs at room temperature [74]. The spontaneous strain localization takes place in the early stage of the loading and then act as concentrator for plastic strain, leading to the formation of a highly localized deformation in the shear band. The rapid propagation of shear band causes premature failure of MGs. Shear banding mechanism exists among many metallic glass systems and it shares some

common features [13]:

- They form approximately along the plane with maximum shear stress
- They are considered to be caused by local disordering associated with dilatation, often assumed to be the free volume generation.
- Shear bands appear to be quite thin (~20 nm)
- A vein pattern often shows on fracture surface associated with instability in a liquid-like layer

Therefore, understanding the shear banding initiation mechanisms and conditions of shear band are crucial in explaining the plastic deformation of MGs and the constriction of shear band propagation would be the major way to enhance the plasticity of MGs.

1.3.2 Atomistic deformation mechanisms

With the development of metallic glasses, a number of theories have been developed in order to explain the heterogeneous nature of plasticity in MGs. In the 1977, Spaepen [75] proposed a flow mechanism in which the general idea is that under an applied shear stress, plastic deformation in MGs is driven by individual atomic jumps in the presence of free volume sites. The shear induced structural disordering will create excess free volume which leads to strain

softening, decrease in viscosity and finally strong shear localization. However, this model fails to explain the atomic processes inside shear bands during plastic flow. Moreover, some recent simulation results demonstrated that the deformation mechanism of MGs involves multiple atoms [76, 77].

In 1979, Argon [78] introduced the concept of shear transformation zones (STZ) as the fundamental process of plastic flow, which has been widely used to explain plastic deformation in MGs. Shear transformation is defined as a thermally activated defect in a metallic glass and usually consists of a group of atoms within a distance of about five atomic diameters. Under an applied shear stress, this shear transformation will initiate around excess volume sites (free volume). By extending these theories, Falk [76] and Langner [79] have proposed a dynamic theory of STZs. Their studies revealed that multiple local shear event is the origin of plastic deformation in MGs. They suggested that cooperative shear motion of STZs determines the yield strength of a MG, and when the global instability achieved by a certain fraction of unstable STZs, the yielding will occur.

In all these theories and models, free volume is considered to play a vital part in the plastic deformation of MGs. As illustrated in Figure 1.6, under shear stress, free volume is formed by forcing the atoms to jump into smaller interstitial spaces in their immediate neighborhood. The deformation in the MG is induced

by series of these discrete atomic jumps. The net forward atomic movements in the direction of applied stress can result in the macroscopic plastic flow. Therefore, determine the free volume inside the MG will be crucial to understand the plastic deformation process of MGs.

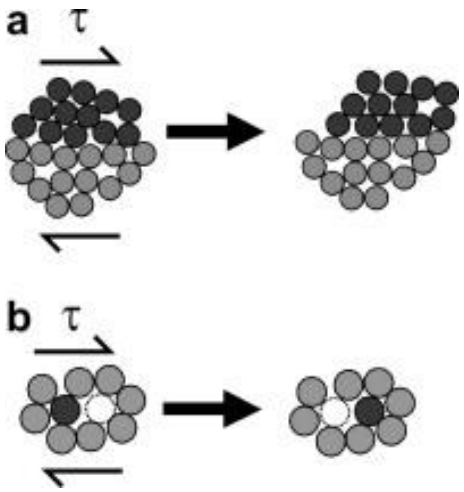

Figure 1.6 Two dimensional schematic illustration of (a) shear transformation zone (STZ) deformation mechanism, and (b) a local atomic jump (free volume deformation mechanism) [80] (Reprinted with permission from Elsevier.)

1.3.3 Free volume

Cohen and Turnbull originally proposed the concept of free volume to model the transport processes in liquid of hard spheres [81-83]. It can be simply defined as:

$$v_f = \bar{v} - v_0 \tag{1.1}$$

where $\bar{v}$ represents the average volume per molecule in the liquid and v_0 represents the Van der Waals volume of the molecule [81]. And its concentration

can be expressed as:

$$c_f = \exp\left(-\frac{\gamma v^*}{v_f}\right) = \exp(-\frac{1}{x}) \tag{1.2}$$

where γ is a geometrical factor, the quantity $x=-\gamma v^*/v_f$ is the reduced free volume, v_f is the average free volume per atom and v^* is the critical volume.

Spaepen [75] further adopted and developed this concept in order to model the diffusion and plastic flow in MGs under different levels of external stress. In metallic glasses, the evolution of free volume can be treated as two competing processes. One is the free volume generation process which can be accelerated by shear deformation [78, 84], and the other is a free volume annihilation process which caused by diffusional relaxation [75, 85, 86].

According to Spaepen's model [87], shear deformation can increase the free volume generation rate as:

$$\Delta^+ \dot{x} = \frac{f}{\gamma}\exp\left(-\frac{\Delta G^m}{kT}\right)\exp\left(-\frac{1}{x}\right)\left[\cosh\left(\frac{\tau\Omega}{2kT}\right)-1\right]\frac{2kT}{xSv^*} \tag{1.3}$$

where f is an attempt frequency, Ω is atomic volume, ΔG^m is the activation energy, k is the Boltzmann's constant, τ is the shear stress, T is the temperature, and $S=2\mu(1+\nu)/3(1-\nu)$ with μ the shear modulus and ν the Poisson's ratio.

On the other hand, diffusion is also affected by applied stress. According to the bimolecular model of the diffusional free volume annihilation process in metallic glass, the annihilation rate of free volume can be expressed as [85, 88]:

$$(\frac{dc_f}{dt})^- = -k_r c_f (c_f - c_{eq}) \tag{1.4}$$

where c_{eq} is the equilibrium defect concentration. k_r is a temperature and stress dependent constant, which relates to the kinetics of diffusion and can be defined as [89]:

$$k_r = f \cdot \exp(-\frac{\Delta G^m - \sigma_m V}{kT}) \tag{1.5}$$

where σ_m is the mean stress, and V is the activation volume varied between 0.6 Ω and 1 Ω [90, 91].

Combining equations (1.2) and (1.5) with equation (1.4), the rate of free volume annihilation due to diffusional relaxation can be calculated as:

$$\Delta^- \dot{x} = -f \cdot x^2 \cdot \left[\exp\left(-\frac{1}{x}\right) - \exp\left(-\frac{1}{x_{eq}}\right)\right] \cdot \exp(-\frac{\Delta G^m - \sigma_m V}{kT}) \tag{1.6}$$

Equations (1.3) and (1.6) are used to estimate the rate of free volume production and annihilation, respectively. These two disordering (free volume generation) and ordering (free volume annihilation) processes combine to control the plastic deformation of MGs. In deformation under room temperature, free volume

generation rate is often much larger than that of its annihilation, so that strain softening and localization are expected. Since the diffusion rate is a function of temperature, at high temperatures close to glass transition temperature (Tg), the rate of free volume annihilation can surpass its generation and metallic glasses can deform homogenously [15, 92, 93].

In addition to temperature, tensile mean stress can also significantly enhance the diffusion process in solids [90, 94-96]. Thus, even at room temperature, a high stress state could possibly induce considerable diffusion in metallic glasses. In such a condition, during loading, free volume annihilation can surpass its accumulation, and may cause hardening in metallic glass instead of softening, as shown in Figure 1.7. Using free volume theory, Wang et al. [97] showed that there exists a hypothetical triaxial stress condition at which the rate of free volume annihilation can surpass its generation, leading to strain hardening in metallic glasses. As shown in Figure 1.7, such a condition is achieved in the center of cylinder samples of Zr-based metallic glass by creating notch geometry [97].

Under uniaxial stress state, $\sigma_1 = \sigma$, $\sigma_2 = 0$, $\sigma_3 = 0$, $\sigma_m = \frac{1}{3}(\sigma_1 + \sigma_2 + \sigma_3) = \frac{1}{3}\sigma$ with σ_1, σ_2 and σ_3 are the three normal stress in x, y and Z directions. And the shearing stress $\tau = \frac{\sigma}{\sqrt{3}}$. The calculated results for the rate of free volume changes for accumulation (equation (1.3)) and relaxation (equation

(1.6) are shown in Figure 1.7 (b).

However, under triaxial loading, such as notched tension, the triaxial stress state can be estimated by using Neuber's analytical expression [98] for the stresses in a parabolically notched sample. In the center of the notch, the three principle stresses can be calculated as:

$$\sigma_u = 2\mathrm{B} - \alpha\mathrm{C} - \mathrm{A} \tag{1.7}$$

$$\sigma_v = \frac{A}{2} - \mathrm{B} + (\alpha - 2)\mathrm{C} \tag{1.8}$$

$$\sigma_w = \frac{A}{2} - \mathrm{B} + (\alpha - 2)\mathrm{C} \tag{1.9}$$

$$\text{with } \mathrm{C} = -\frac{\sigma_0}{2}\frac{1+\cos v_0}{1+(2-\alpha)\cos\upsilon_0+\cos^2 v_0} \tag{1.10}$$

$$\mathrm{A} = \mathrm{C}(\alpha - 1)(1 + \cos v_0) \tag{1.11}$$

$$\mathrm{B} = \mathrm{A} - \mathrm{C}\cos^2 v_0 \tag{1.12}$$

In these equations, $\alpha = 1(1 - \upsilon_p)$ and $cosv_0 = \sqrt{\frac{\rho}{\rho+\frac{d}{2}}}$

where υ_p is the Poisson's ratio; ρ is the radius of the notch and d is the diameter of the final minimum bar. And applying the notch geometry in Wang et al.'s experiments [97] and υ_p = 0.377, the tensile mean stress and shear stress can be figured out: $\sigma_m = \frac{1}{3}(\sigma_u + \sigma_v + \sigma_w) = 0.442\sigma$ and $\tau =$

0.116σ. Therefore, the notched geometry can create a substantially higher mean stress and a substantially lower shear stress, and then may lead to a higher free volume annihilation then its generation, as shown in Figure 1.7.

Further experiments performed by Wang et al. [97] confirmed the strain hardening phenomenon of the notched sample and ordering or densification in the notch region. This work revealed a possible way to design tough glasses based on their flow properties. However, considering the spatial and temporal limitations of experimental techniques on measuring the free volume evolutions, it is still difficult to directly demonstrate the atomic level structural changes during mechanical deformation. Meanwhile, molecular dynamics (MD) simulation method can provide us a detailed observation inside the deformed region to uncover the relationship between mechanical responses and structure.

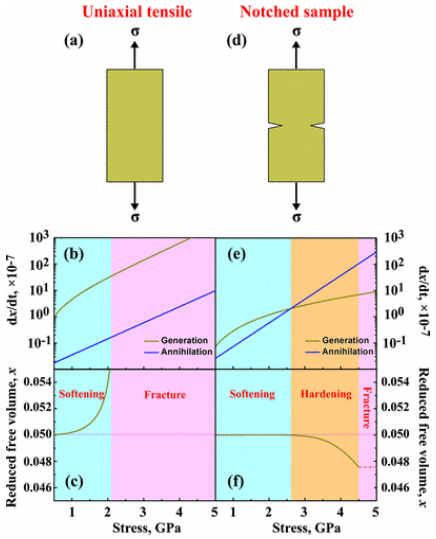

Figure 1.7 The effect of stress state on the free volume generation and annihilation rates in a metallic glass under tension. [97] (Reprinted with permission from American Physical Society.)

1.3.4 Molecular dynamics approaches

Various experimental techniques have been used to investigate the free volume change induced by plastic deformation such as direct density measurements [99, 100], positron annihilation [101, 102], and TEM (transmission electron microscope) observations [103]. However, these experimental techniques do have spatial and temporal limitations on measuring the free volume changes inside the sample. First, most characterizations have to be conducted after sample failure and quantitative *in-situ* measurements become a challenge. Second, experiments can only measure volume changes weighted by the volume of the entire sample, while the subtle evolutions inside the shear band are beyond experimental measurements. Meanwhile, molecular dynamic (MD) simulations can provide us a detailed atomic level analysis during the mechanical deformation. Several parameters can be monitored by using MD simulation, such as system energy, enthalpy and entropy, atomic volume, and local bonding environment.

One of the commonly studied parameters is the atomic volume evolution during plastic deformation. As defined by Cohen and Turnbull, free volume is the "critical excess" on a per atom basis [81], relative to a critical atomic volume for an ideal glass with zero free volume. Under simulation conditions, such "excess volume" dilation or shrinkage cannot be easily calculated and are often

be substituted by the Voronoi volume of an atom subtracting the volume of the atomic core. Thus, the excess volume can be expressed as:

$$v_{excess} = v_{voro} - v_{atom} \tag{1.13}$$

If we assume that the atomic core volumes are constant (which is the general case for metallic atoms), the Voronoi volume will then be directly related to the excess volume and also the Turnbull free volume [14, 104]. Therefore, Voronoi volume can be used sufficiently to represent the volumetric changes during mechanical deformation.

Many simulation studies have been carried out using this method to investigate the structural changes in MGs during mechanical deformation [105-108]. Cao et al. [108] found that the Voronoi volume increases in the localized shear band accompanied by breakdown of full-icosahedra and increases in local temperature under uniaxial tensile simulation; Li and Li [109] proved the local volumetric evolution or free volume generation during shear deformation; The work by Ritter and Albe [110] testified an increase in excess volume inside the shear band for both Cu-rich and Zr-rich CuZr MGs. Different simulation conditions, composition and loading parameters have been used among these MD studies, which results in different Voronoi volume changes. However, they all showed a clear trend of Voronoi volume generation during mechanical

deformation, which is consistent with many previous experimental observations [111-115].

Besides the perspective of free volume evolution during plastic deformation, another research direction has been proposed to study the local bonding environment of MGs during mechanical deformation. Several authors have investigated the short-range order structure in MGs, and discovered that they are directly related to the plastic deformation process. Cao et al. [108] identified the breakdown of full-icosahedra clusters as the structural signature of shear localization, and shear transformations and local strain are both influenced by FI ordering, as shown in Figure 1.8.

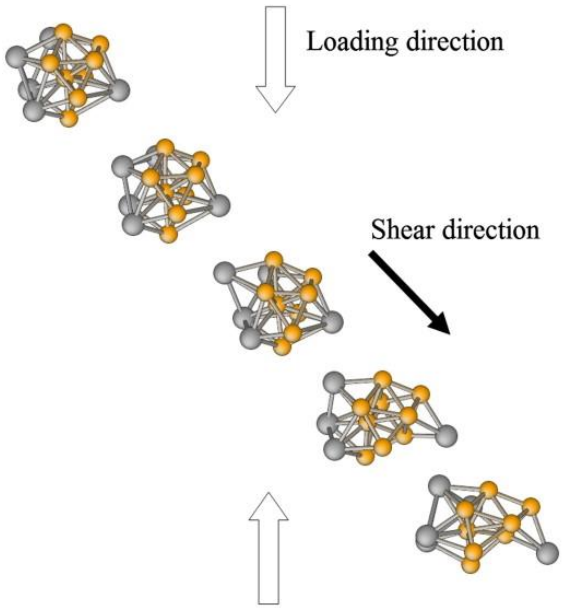

Figure 1.8 The destruction of a full-icosahedra cluster, upon joining the localized deformation band. [108] (Reprinted with permission from Elsevier.)

Cheng et al. [62] studied the role of FI clusters in shear transformation in a wide

range of cooling history and alloy composition. They identified the fertile and resistant structural entities controlling deformation. These simulation works proposed another atomic level aspect of the deformation mechanism of MGs and have proved to be effective for MGs under uniaxial and shear stress.

However, as mentioned before, the mechanical behavior of MGs under multiaxial stress state is a quite different situation and few MD simulation works have been performed to study this area. Moreover, experiments have observed the strain hardening and densification of MG under multiaxial tension at room temperature [97], there is a pressing need to analyze this phenomenon in the view of atomic level and use simulation methods to investigate the mechanism beneath it.

1.3.5 Strain rate effect on the deformation mechanism of MGs

Similar to crystalline metals, metallic glasses also exhibit strain rate sensitivity, which means their mechanical properties are dependent on the applied strain rate. Many experiments have been carried out to study their mechanical behavior dependence on strain rate. Due to the various alloy systems and atomic structures that MGs can adopt, the effect of strain rate on their mechanical behaviors are also quite distinctive. Liu et al. [116] determined that the strain rate has little effect on the macroscopic shear strength, but can greatly influence the initiation of shear band and final fracture. Others have found that the

mechanical behavior of Vitreloy 1 BMG is relatively insensitive to strain rate [15, 117, 118]. Some metallic glass systems, like Nd-based and Zr-based metallic system, showed positive strain-rate sensitivity [119-122]; while studies of other metallic systems such as Zr-based MGs proved the negative strain-rate sensitivity on many BMGs, meaning that the fracture stress decreases when the strain rate increases [123-129]. Table 1.4 concludes some previous literatures on strain rate effect of MGs.

Table 1.4 Selected previous literatures of the strain rate effect on MGs

Strain rate effect	*Metallic glass composition*
Negative strain-rate sensitivity	$Pd_{40}Ni_{40}P_{20}$ [130]
	$Zr_{41.5}Ti_{13.5}Ni_{10}Cu_{12.5}Be_{22.5}$ [131]
	$(Hf_xZr_{1-x})_{52.5}Ti_5Ni_{14.6}Cu_{17.9}Al_{10}$ [124]
	$Zr_{52.5}Ti_5Cu_{17.9}Ni_{14.6}Al_{10}$ [126]
	Dy_3Al_2 [132]
Positive strain-rate sensitivity	$Nd_{60}Al_{10}Fe_{20}Co_{10}$ [119]
	$Zr_{65}Al_{10}Ni_{10}Cu_{15}$ [120]
	$Ti_{45}Zr_{16}Ni_9Cu_{10}Be_{20}$ [121]
	$Ti_{40}Zr_{25}Ni_8Cu_9Be_{18}$ [122]
Strain-rate insensitive	Vitreloy 1 [117]

Since BMGs do not have the same atomic structure as their crystalline counterparts, it is hard to directly apply conventional theories of strain-rate sensitivity to them. Previous studies have used several alternative hypotheses to explain the influence of strain rate on the yield stress. Gu et al. [128] discovered the negative strain-rate sensitivity on many BMGs, focused on (Hf,Zr)–Ti–Cu–Ni–Al alloy system, as shown in Figure 1.9. They made mechanistic explanation

[128] that for these materials, adiabatic processes occur during the failure of BMGs which is favored by higher strain rates. Therefore, at higher strain rates, a lower failure strength can occur when such adiabatic processes are more prevalent.

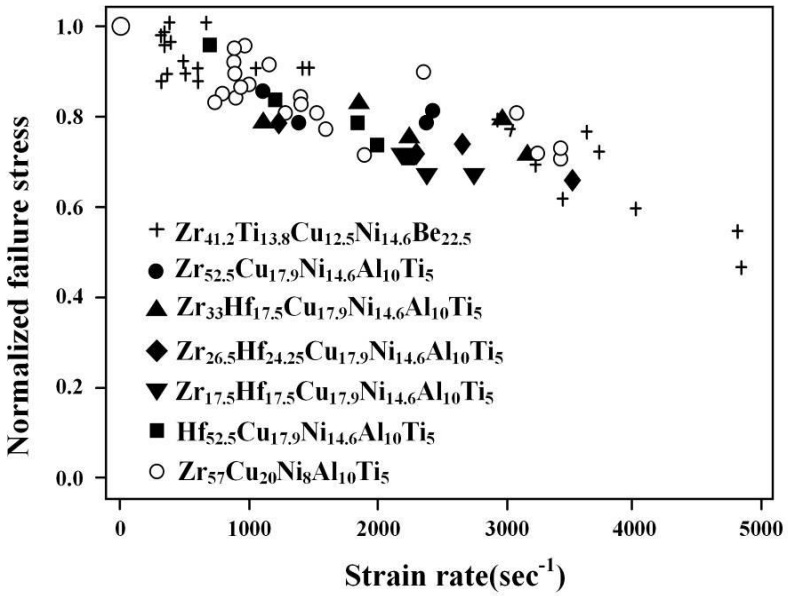

Figure 1.9 Normalized failure stress as a function of strain rate of various MGs, showing negative strain rate sensitivity. [128] (Reprinted with permission from Elsevier.)

Other studies performed by Xue et al. [133] found that in Zr-based materials exhibit negative strain-rate sensitivity. The high strain rates can suppress the serrated flow, which is common at quasi-static strain rates. They [133] pointed out that under dynamic loading, substantive voids are spontaneously created due to the coalescence of a larger number of net free volume. Consequently, multiple shear band formation spontaneously initiated, forming microcracks or micro shear bands, which would promote failure at a lower stress. Therefore, specimen

under dynamic loadings will yield earlier with no serrated flow shown.

Contrast to the Zr-based BMGs mentioned above, Ti-based BMGs have been shown to present positive strain-rate sensitivity [121, 122]. This is attributed to the different microstructure on the atomic scale of Ti-Based alloys compared to other alloys [121] and the existence of a micro-crystalline structure is also responsible for the positive strain rate sensitivity.

Some previous simulation works have been carried out to investigate the strain rate effect on MGs. Cheng and Ma [134] have determined that the maximum shear stress of Cu-Zr metallic glass increases as increasing the strain-rate, and this phenomenon can be well explained by using the cooperative shear model (CSM) [135, 136]. Guan et al. [137] also found this increase in shear stress in the Cu-Zr-Al system under pure shear condition. By using the Lenard-Jones potential, Rottler and Robbins [138] have studied the strain rate effect on the shear yielding of amorphous glassy solids.

However, it should be noted that little research has been done on the metallic glass under uniaxial loading, not to mention that the geometry influences (such as notch condition) on the strain-rate sensitivity of MGs. The local structural transformations inside the shear band or plastic deformed region under different strain rate remain a mystery. Therefore, it is important to investigate this situation using MD simulation methods for a better understanding of MGs.

1.3.6 Temperature effect on the deformation mechanism of MGs

Apart from the influence of strain rate on the mechanical behaviors of MGs, temperature can also influence the deformation behavior of MGs. It is known that at elevated temperature, BMGs will show homogeneous flow at low strain rate; while shear localization can be observed at high strain rate [13]. The boundaries separating these different deformation modes corresponding to strain rate and temperature are shown in Figure 1.10. At room temperature, the critical strain rate to avoid shear localization is imaginably high; however, at high temperature, an achievable strain rate can induce the homogenous flow of metallic glass. Many experiments have been performed to testify this phenomenon [15, 139-141] with different metallic glass compositions.

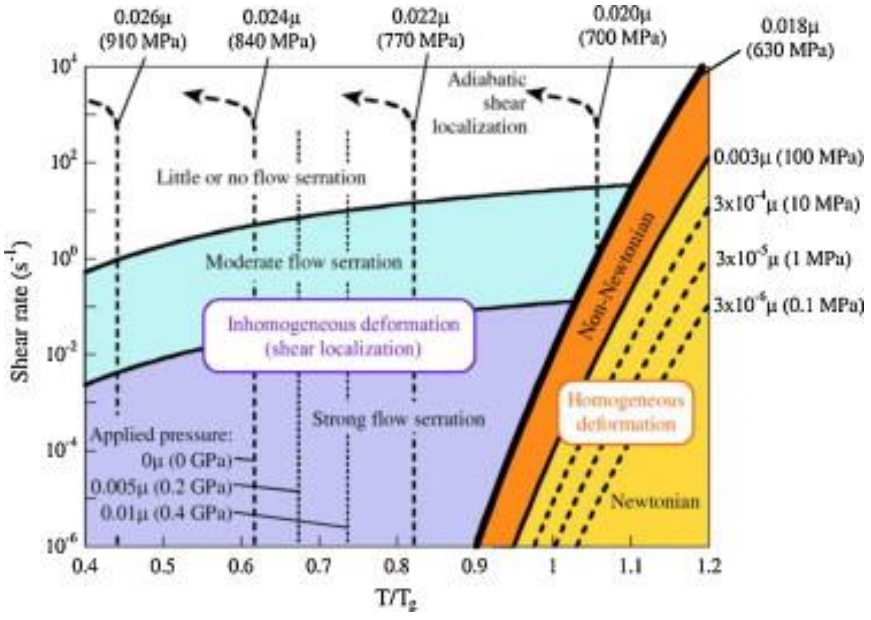

Figure 1.10 Deformation mechanism map for metallic-glass samples. [13] (Reprinted with permission from Elsevier.)

Dalla Torre [142] has studied the effect of strain rate and temperature on the deformation mechanism of Zr-based MGs. By conducting compressive experiments between 77 and 300 K, he found that flow serrations decrease severely with strain rate and decreasing temperature increases, while at the same time, the speed of the stress drops increase. A decrease in steady-state strain-rate sensitivity, which is defined as $m = \left\{\frac{\delta \ln \sigma}{\delta \ln(d\varepsilon/dt)}\right\}_{\varepsilon}$, is observed, as illustrated in Figure 1.11. They pointed out that the fundamental difference in the deformation mechanism together with shear band evolution cause the change in strain-rate sensitivity [142].

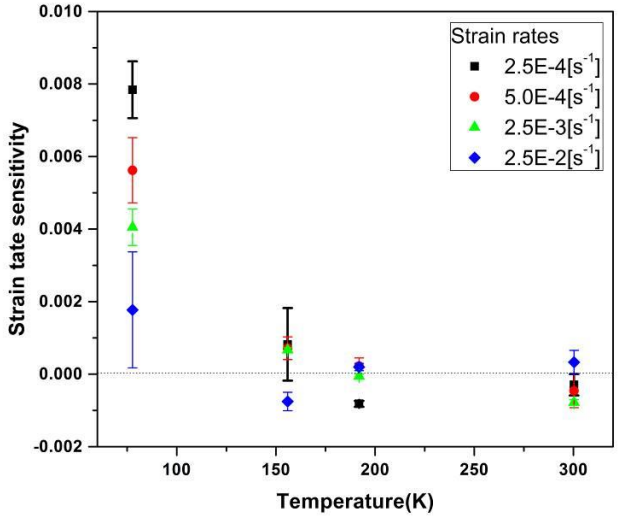

Figure 1.11 Strain rate sensitivity as a function of temperature for different mean strain rates for a $Zr_{50}Cu_{50}$ BMG. [143] (Reprinted with permission from Elsevier.)

Scientists and Engineers have also used simulation methods to study the mechanisms beneath this phenomenon. According to a simulation performed by

Cheng and Ma [134], under pure shear condition, as the temperature rises, the maximum shear stress of $Cu_{64}Zr_{36}$ metallic glass will decrease. They have successfully used CSM theory to explain this situation under shear deformation. However, few papers have mentioned the reaction of the deformation mechanism of MGs under multiaxial stress states to the temperature. Since temperature can influence both the free volume generation and annihilation rate [75, 81, 85], one may wonder whether the strain hardening phenomenon found by Wang et al. [97] can apply at different temperature. Thus it is necessary to investigate the deformation behavior of CuZr metallic glass under multiaxial stress state at different temperatures and analyze the influences of temperature on the atomic level mechanisms.

1.4 Motivations and objectives

In view of the above review, despite intense researches into the MGs, some key issues remain unresolved.

- First, the atomic-level structure of CuZr metallic glasses still remains somewhat unclear. The influences of cooling history on the atomic structure have not yet been fully uncovered.

- Experimental works have confirmed that a notch geometry and multiaxial stress state can lead to strain hardening and annihilation of free volume in

metallic glasses. However, local structure evolution and deformation mechanism on atomic level during the plastic deformation under these conditions still need to be investigated.

- The strain rate sensitivity of MGs remains one of the most important outstanding questions, and both free volume generation and its annihilation can be hugely dependent on strain rate. Therefore, it is necessary to discuss the effect of strain rate on the deformation mechanism of CuZr metallic glasses, especially those under multiaxial stress states.

- Both the generation of free volume and its annihilation is greatly influenced by temperature. Thus, the effect of temperature on the atomic structure evolution during plastic deformation must be investigated.

Molecular Dynamics simulation can offer an atomic-level view for understanding the structural evolution of MGs within nanosecond regimes. By using MD simulation, we can investigate the atomic-level mechanisms underlying the issues mentioned above.

The specific objectives of this research were to:

- Simulate $Cu_{64}Zr_{36}$ metallic glass by using EAM potential and LAMMPS code. Analyze the quenching rate effects on the simulated samples.

- Investigate the influences of notch geometry and multiaxial stress states on the deformation mechanism of the prepared $Cu_{64}Zr_{36}$ glass samples. Use detailed structural analysis to reveal the atomic evolution during the plastic deformation and the changes in Voronoi volume, Cu-centered polyhedra and local temperature.

- Reveal the effect of strain rate and temperature on the unnotched and notched samples with different geometry. Using CSM theory to explain their mechanical properties and discover the atomic structural evolution under various environments.

The results of this present study may offer a clear and simple explanation for the mechanical properties of MGs under various situations such as different geometry and stress states, different strain rates, as well as different temperatures. Using Voronoi tessellation methods, it is discovered that the multiaxial stress state can lead to the strengthening of metallic glass, accompanied by the annihilation of Voronoi volume, recovery of full-icosahedra fraction and decrease in local temperature. Such strengthening phenomenon has been found to only exist under low strain rate and low temperature conditions. These findings will have significant implications for understanding the intrinsic structure and mechanical properties of MGs.

Chapter 2 Molecular dynamics simulation

2.1 Introduction

Molecular dynamics simulation has been proved to provide unique insights into the atomic-scale processes applicable to problems from material science to condensed matter physics [144-147]. With the fast development of computer hardware and high-efficiency algorithms, more and more interatomic potentials have been precisely described and testified by laboratory or experimental results. These give rise to a wider application of MD simulation in predicting and analyzing the mechanical and physical properties and behaviors of many materials. For metallic glasses, MD simulation has been testified to be a useful tool for elucidating the local topology, the structural evolution, and atomic-level relationship between structure and properties [11, 148-150].

The initial idea of MD simulation was first brought by Fermi in 1955 [151]. In 1957, Alder and Wainwright [152, 153] used MD methods to study the phase transition of a hard sphere system, which is considered as the first successful application of MD methods in physics and chemistry. In the 1970s, MD simulation method thrived with the introduction of fluctuation-dissipation-theorem (FDT), density-functional-theory (DFT), etc. [146]. Now, it can be catalogued as Equilibrium Molecular Dynamics, Non-equilibrium Molecular Dynamics, ab-initio Molecular Dynamics, Large Scale Molecular Dynamics,

etc. [154].

Although MD simulation has efficiency and convenience compared to experimental methods, it does have spatial and temporal deficiencies that have not yet been conquered. First, the number of particles of the simulated model is limited. Usually, it can only simulate up to 10 million particles with a dimension up to nano-scale, which is still too small compared to the particles in macroscopic samples which can contain on the order of 10^{23} atoms/cm^3. The most effective way to limit the influence of boundary conditions and improve the data accuracy is to increase the simulation scale, but thus can significantly burden the calculability. Second, in order to precisely track the movement of particles and ensure the stability of simulation, a small timestep is needed, which is commonly in the order of femtoseconds or picoseconds. Thus, a common MD simulation can only predict the movement of objects in a timescale up to a few nano seconds. Many approaches have been applied to solve these issues, involving periodic boundary conditions, parallel large scale simulation and GPU-accelerated simulation. Despite these deficiencies, MD simulations can still offer a distinctive vision into the atomic level behavior of materials that we studied with good coincidence with experimental results. Thus it has become more and more important in the field of material science.

In this chapter, the basic principle of MD simulation will be introduced, along

with the parameters and conditions involved in this work. The characterization method will be described in details.

2.2 Basic principles

The basic idea of MD simulation is rather straightforward. Given a N particles classical system in a confined volume with periodical boundary condition, the movement of particles is governed by the classical mechanic's equations of the motion, i.e. Newton's equation. For this N particles system, the total energy is equal to the summation of kinetic energy and potential energy of each particle. The kinetic energy is determined by velocity of particles while potential energy can be expressed as a function of particle position as:

$$U = U_k + U_p = \sum_{i=1}^{N} \frac{1}{2} m_i {v_i}^2 + U_p(\overrightarrow{r_1}, \overrightarrow{r_2}, \dots, \overrightarrow{r_N}) \quad (2.1)$$

where, U_k is the system kinetic energy; U_p is the system potential energy; m_i and v_i are the mass and velocity of atom i, respectively; $\overrightarrow{r_i}$ is the position vector of atom i.

According to classical physics, the force applied on any atom i can be expressed as the change of gradient on potential energy:

$$a_i = \frac{\overrightarrow{F_i}}{m_i} \quad (2.2)$$

After time integration, the position and velocity of atom i after δt can be described as:

$$\vec{r_i}(\delta t) = \vec{r_i} + \vec{v_i}t + \frac{1}{2}\vec{a_i}\delta t^2 \quad (2.3)$$

$$\vec{v_i}(\delta t) = \vec{v_i} + \vec{a_i}\delta t \quad (2.4)$$

By solving the motion equation of all involved particles, the MD simulation can give the trajectory of each individual particle.

2.3 The potential energy

The interatomic potential is the most important input of any MD simulation. It describes the principles that govern the interaction of atoms in the system, due to that the forces applied on each atom can be calculated from the interaction function. The accuracy of the interatomic potentials entirely controls the veracity of the simulation in reproducing the experimental observations. Consequently, huge efforts have been made to develop the interatomic potentials. During the development of MD simulation, several models have been proposed to fit different material systems.

2.3.1 Pair potential

In the early period of MD simulation, several pair potentials were proposed to

mainly describe inert gases or liquid systems. The most widely used are Lennard-Jones (LJ) potential and Morse potential.

Lennard-Jones [155, 156] potential is often used in describing the acting force in gas and water system, and can be expressed as:

$$\Phi(r_{ij}) = 4\varepsilon\left[\left(\frac{\sigma}{r_{ij}}\right)^2 - \left(\frac{\sigma}{r_{ij}}\right)^6\right] \quad (2.5)$$

where ε and σ are the energy and distance parameters, respectively. $\left(\frac{\sigma}{r_{ij}}\right)^2$ stands for the short-range rejection force and $\left(\frac{\sigma}{r_{ij}}\right)^6$ stands for the long-range attraction force.

Morse potential [157] is commonly used in describing inert gas or simple metals, and can be expressed as:

$$\Phi(r_{ij}) = A\left[e^{-2\alpha(r_{ij}-r_0)} - e^{-\alpha(r_{ij}-r_0)}\right] \quad (2.6)$$

where A represents the binding energy and r_0 represents the balance distance.

These two potentials can be efficiently used to study simple systems such as an inert gas or simple metals; whereas for complex systems, their credibility is in doubt.

2.3.2 Embedded atom method potential

Daw and Baskes proposed the embedded atom method (EAM) in the 1980s [158, 159]. The basic principle of the EAM potential is that in the system, each atom can be treated as an impurity embedded in all other atoms, so that the system energy can be expressed as the summation of embedding energy and interatomic potential energy. According to the quasiatom model, the energy of the system containing N atoms can be given as:

$$E_{total} = \sum F_i(\rho_h) \tag{2.7}$$

where ρ_h is the electron density of the host at the position of atom i but without atom i and $F_i(\rho_h)$ is the embedding energy of atom i.

In this model, each atom is assumed to be merged in a local uniform electron gas. The embedding energy thereby is defined as the energy of this atom in the electron gas relative to an atom separated from the electron gas [158]. However, such an assumption of an extreme locality and a complete uniformity cannot reflect the realistic situation. Thus, two correlations have been made to the equation (2.7). The first is to use local density $\rho_{h,i}$ to replace the average density ρ_h in the embedding function. The second is to add an additional term to the equation (2.7) to correct the core-core repulsion. The total energy of the system can then be described as:

$$E_{total} = \sum_i F_i(\rho_{h,i}) + \frac{1}{2}\sum_{j\neq i} \phi_{ij}(r_{ij}) \quad (2.8)$$

where ϕ_{ij} is the short-range pair potential and r_{ij} is the distance between atom i and j. $\rho_{h,i}$ is the local density of the host at the position of atom i. Further simplifications have been made to assume that the host density $\rho_{h,i}$ is approximated by a linear superposition of the contributions from the neighboring atoms.

$$\rho_{h,i} = \sum_{j\neq i} \psi_j(r_{ij}) \quad (2.9)$$

where $\psi_j(r_{ij})$ is the contribution from atom j to the density $\rho_{h,i}$.

The EAM potential can effectively describe and predict many alloy systems and has been widely used in the MD simulation studies of metallic glasses [160-163]. The potential used in this study is the EAM potential of Cu-Zr binary system proposed by Sheng et al. [25].

2.3.3 Other Potential Energy Methods

Besides EAM, other methods like modified embedded atom method (MEAM) potential [164, 165], the Finnis-Sinclair potential (F-S) [166], and the second-moment approximation of tight-binding potential (SMA-TB) [167-169] have been developed in computational material science. Even if these models share similar analytical forms, there exist vast differences in the procedures to build

the potential functions, which usually result in rather different parameterizations for the same material.

2.4 Ensemble and thermostat

2.4.1 Ensemble

MD simulations deal with many-body systems. However, due to the limitation of computation capability, particles inside the simulated system are always confined, which is quite different to experimental conditions. Different from common statistical physics which mainly studies the gas phase, the main object of MD is liquid or solid phase. In liquid or solid phase, the interaction between atoms is very strong, which is quite different from ideal gas where only collisions and no other interactions are considered. However, the principle of statistical physics still applies in MD simulation and the particle system in MD must obey the rule of the particle ensemble.

An ensemble is a collection of all possible microstates that have the same macroscopic properties of a thermodynamic system in which we are interested. In typical MD simulations, the parameters commonly involve number of atoms N, volume V, energy E, temperature T and pressure P. During MD simulation, appropriate ensemble should be chosen according to the practical conditions. For example, a closed isothermal system and an isolated system correspond to

the canonical (constant N, V and T) and microcanonical (constant N, V and E) ensemble, respectively.

In the work for this thesis, both canonical (constant N, V and T) and isothermal–isobaric (constant N, P and T) ensembles have been used in different simulation conditions.

2.4.2 Thermostat

The adjustment of temperature in MD simulation can be approached by adding a correction factor. The present temperature is calculated by the present velocity of all particles, as:

$$T_{cal} = \frac{\sum_{i=1}^{N} m_i(v_{x,i}{}^2+v_{y,i}{}^2+v_{y,i}{}^2)}{3NK_B} \tag{2.10}$$

where m_i is the mass for atom i, $v_{x,i}$, $v_{y,i}$ and $v_{z,i}$ are the velocity component in three coordinates. N for the number of atoms and K_B is the Boltzmann constant.

Typically, the temperature range allowed is:

$$0.9 \leq \frac{T_{set}}{T_{cal}} \leq 1.1 \tag{2.11}$$

If the temperature calculated is above this range, then a correction factor should be multiplied to the velocity of each atom:

$$f = \sqrt{\frac{T_{set}}{T_{set}}} \tag{2.12}$$

where T_{set} is setting temperature and T_{cal} is the calculated temperature.

Combining equation (2.11) and (2.12), we can get the corrected temperature as:

$$\frac{\sum_{i=1}^{N}[(v_{x,i}f)^2+(v_{y,i}f)^2+(v_{z,i}f)^2]}{3NK_B} = T_{cal}\left(\frac{T_{set}}{T_{cal}}\right)^2 = T_{set} \tag{2.13}$$

This method is rather straightforward and usually used in the microcanonical (constant N, V and E) ensemble. For ensembles that need more accurate thermostat, like canonical (constant N, V and T) and isothermal–isobaric (constant N, P and T) ensemble, more appropriate adjustment like Nose-Hoove thermal bath has to be introduced [170, 171].

In the Nose-Hoove thermal bath method, the constant temperature condition is achieved by coupling the momenta of the atoms to an external heat bath. Another degree of freedom S to adjust the momentum is introduced in order to thermostat the system. The physical parameter after adjustment can be expressed as:

$$\frac{d\vec{r}_i}{dt} = \frac{\vec{P}_i}{m_i} \tag{2.14}$$

$$\frac{d\vec{P}_i}{dt} = -\nabla_i U - \xi\vec{P}_i \tag{2.15}$$

$$\frac{d\xi}{dt} = \left(\sum_{i=1}^{N} \frac{p_i^2}{m_i} - \frac{3N}{K_B T}\right) \Big/ Q \tag{2.16}$$

$$\frac{ds}{dt} \Big/ s = \xi \tag{2.17}$$

where U is the potential energy function of the system, Q is an imaginary mass which should be chosen carefully along with the systems; ξ is the coupling parameter which determines how tightly the bath and the system are coupled together.

2.5 Periodic boundary condition (PBC)

Due to the computation limitation of computers, MD simulation can only deal with systems in the nano-scale. Increasing the particle numbers will hugely increase the calculation time. Although by adopting parallel-computation, one can somehow increase the power of MD simulation, yet the communication between each computation core can give rise to other problems, as illustrated below, which still limit the size of system we need to simulate.

Consider a system with 1000 atoms arranged in a $10 \times 10 \times 10$ cube. About 50% of the all atoms will be positioned on the surface area, which would have a huge impact on the measured physical properties. Even for 10^6 atoms, up to 7% of the atoms are amount the surface atoms, which is still nontrivial. Thus, periodic boundary conditions are introduced to solve this problem and make

MD simulation suitable for larger or even macro-scale systems. An atom that leaves the simulation box would be considered to reenter the box on the other side as an incoming atom. In this way, the small simulation box will be considered as being surrounded by replicas of itself. Of course, it should be noted that this method is only suitable for systems with short-range potential; while in systems with long-range potential this method would cause serious miscalculation, for example charged or dipolar systems [172, 173].

2.6 Large-scale Atomic/Molecular Massively Parallel Simulator

In the present work, MD simulations were performed based on EAM potentials in the NVT and NPT ensembles using the Large-scale Atomic/Molecular Massively Parallel Simulator (LAMMPS) code [174]. This code was developed by Sandia National Laboratories, a US Department of Energy facility. LAMMPS is a classical molecular dynamics code which can process simulations on solid-state materials (metals, semiconductors) and soft matter (biomolecules, polymers) and coarse-grained or mesoscopic systems [174]. It is distributed as an open source code under the terms of the GNU Public License (GPL).

In the most general sense [174], LAMMPS integrates Newton's equations of motion for collections of atoms, molecules, or macroscopic particles that interact via short- or long-range forces with a variety of initial and/or boundary

conditions. To improve the computational efficiency, neighbor lists are used to keep track of nearby particles. The lists are optimized for systems with particles that are repulsive at short distances, so that the local density of particles never becomes too large.

The basic flowchart of MD simulation based on LAMMPS can be expressed as shown in Figure 2.1.

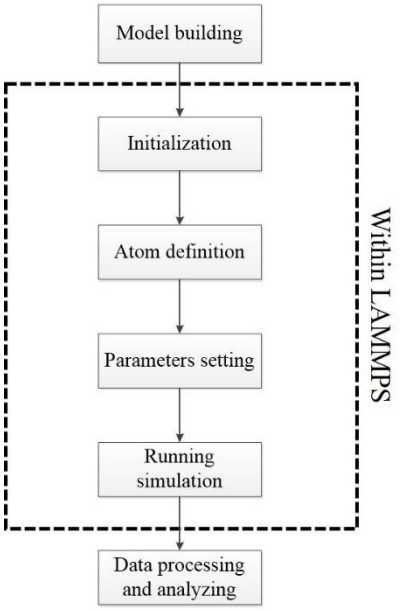

Figure 2.1 The flowchart of MD simulation based on LAMMPS

2.7 Characterization

One of the major challenges when studying metallic glasses is the effective characterization of the amorphous structure and to extract the key features that are closely relevant for the physical and mechanical properties [21]. Unlike crystalline materials whose atomic structure can be easily identified in terms of

lattice constants and crystal symmetries, we have to use alternative measurements to describe amorphous structures.

2.7.1 Pair distribution function

Pair distribution function (PDF) is defined as a pair correlation representing the probability of finding atoms as a function of distance r from an average center atom [25]. The PDF of a liquid/glass can reflect the distribution of interatomic distances, the shell-like structure in the radial direction, and their fading out with increasing distance. The partial PDF can be defined as:

$$g_{\alpha\beta}(r) = \frac{N}{4\pi r^2 \rho N_\alpha N_\beta} \sum_{i=1}^{N_\alpha} \sum_{j=1}^{N_\beta} \delta(r - |\vec{r}_{ij}|) \quad (2.18)$$

where ρ is the number density of atoms in the system of N atoms, N_α and N_β are the number of atoms of type α and β, respectively [175]. $|\vec{r}_{ij}|$ is the interatomic distance between two atom i (of type α) and atom j (of type β). If α and β are the same species of atoms, this can be simplified as:

$$g(r) = \frac{1}{4\pi r^2 \rho N} \sum_{i=1}^{N} \sum_{j=1, j\neq i}^{N} \delta\left(r - |\vec{r}_{ij}|\right) \quad (2.19)$$

For metallic glasses, structure information can be derived from the peak position, peak widths, and relative intensity. It is believed that the short-range order contributes to the first peak, and the structural features from the first peak to the distance of r=1 ~ 2 nm described the medium-range-order [25]. Beyond this

distance range, the PDF gradually converges to unity, suggesting the absence of long-range-order [25]. However, this approach cannot be used to establish the precise description of a real 3D atomic configuration, since the PDF is only a statistical average projection of the structure in one dimension [21].

In this thesis, PDF is calculated by using the analysis tools provide by open-source packages Visual Molecular Dynamics (VMD) [176].

2.7.2 Local atomic strain

For visualization and analyzing the shear transformation zone in the deformed metallic glasses, we use the local shear strain η_i^{Mises}, as introduced by Shimizu et al. [177]. For each atom i, two configurations are required to calculate the η_i^{Mises}: the current and one reference. First, a local transformation matrix J_i is needed, which best maps:

$$\{d_{ji}^0\} \rightarrow \{d_{ji}\}, \quad \forall j \in N_i^0 \tag{2.20}$$

where d's are vector separations (row vector) between atom j and i. j is one of the nearest neighbors of atom i. N_i^0 is the total number of neighbor of atom i, at the reference configuration. J_i is determined by minimizing [76]

$$\sum_{j\in N_i^0} \left| d_{ji}^0 J_i - d_{ji} \right|^2 \rightarrow J_i = \left(\sum_{j\in N_i^0} d_{ji}^{0T} d_{ji}^0 \right)^{-1} \left(\sum_{j\in N_i^0} d_{ji}^{0T} d_{ji} \right) \tag{2.21}$$

For each J_i, the local Lagrangian strain matrix is calculated as:

$$\eta_i = \frac{1}{2}(J_i J_i^T - I) \quad (2.22)$$

Thus the atom i's local shear invariant can be calculated as

$$\eta^{Mises} = \sqrt{\eta_{yz}^2 + \eta_{xz}^2 + \eta_{xy}^2 + \frac{(\eta_{yy}-\eta_{zz})^2+(\eta_{xx}-\eta_{zz})^2+(\eta_{xx}-\eta_{yy})^2}{6}} \quad (2.23)$$

In this thesis, the local atomic strain is calculated by using open-source codes provided by Ju Li's group [177].

2.7.3 Voronoi Tessellation method

In this work, the short-range order and packing density of Cu-Zr metallic glasses are measured by using the Voronoi Tessellation method [178, 179]. The Voronoi Tessellation method gives a possible way to partition the space around an atom by bisecting planes to the nearest neighbors of the given atom [178]. A unique polyhedron associated with each atom can be determined by the perpendicular bisecting planes of the vectors between every atomic pair. Those polyhedra are known as Voronoi polyhedra and each encloses the part of space that is closer to the center atom than any other atoms[25].

By using Voronoi Tessellation method, we can unambiguously determine the Coordination number (CN) of an atom without the need of a cutoff: the number

of faces of the Voronoi polyhedra equals the geometric CN of the center atom. The shape of Voronoi polyhedra reflects the arrangement of all neighbors of a given atom, which can be characterized by the Voronoi index [n_3, n_4, n_5, n_6, …], where n_i denotes the number of i-edged faces of the Voronoi polyhedra. This method has been commonly used for characterizing the local topology in MD simulated amorphous structures [180-182]. Figure 2.2 shows a sample of the Voronoi Tessellation method and a sample of Voronoi polyhedra. In this thesis, the Voronoi volume and Voronoi index calculation is performed by using open-source Voro++ codes [183].

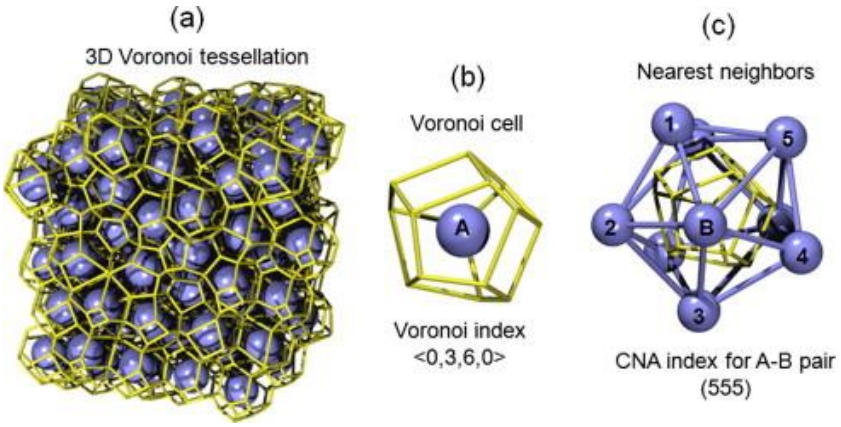

Figure 2.2 (a) Voronoi tessellation method of a configuration of an amorphous structure. (b) Voronoi polyhedra of center atom A with index of <0, 3, 6, 0>, meaning that it has three quadrangular faces and six pentagonal faces. (c) the nine nearest neighbors surrounding the center atom A [25]. (Reprinted with permission from Elsevier.)

2.7.4 Visualization tools

In order to get an insight into the atomic configuration and analyze the physical phenomenon of the MGs, a powerful visualization technique is needed. The task

the visualization tools is to translate the atomic coordinates from MD simulation into meaningful and observable graphical representations while at the same time, provide useful topological information related to atomic structures. There have been several packages designed for visualization of atomic and molecular structures, such as (Visual Molecular Dynamics) VMD [176], Open Visualization Tool (OVITO) [184], Materials Studio [185], and Atomeye [186]. In this thesis, all the atomistic visualization is presented by using open-source visualization tool Atomeye.

Chapter 3 CuZr metallic glasses preparation and its characterization

3.1 Introduction

As reviewed in the introductory chapter, the atomic structure of Cu-Zr metallic glasses is still not yet fully revealed. Therefore, it is important to create appropriate structural models for computer simulations. However, due to the lack of long range translational and orientational order in metallic glasses, these cannot be easily modeled as crystalline materials using replication of crystalline units according to the specific translational symmetry, and other approaches have to be attempted to synthesize the computational models. The most common technique to simulate glassy systems is by mimicking experiments, namely the melt-quenching process. Due to the limited spatial and temporal scales accessible to MD simulation, the simulated quenching rates are several orders of magnitude high than that in experiments. The quenching rate plays a vital role in determining the atomic structure of the concerned glass. It is, therefore, necessary to characterize the simulated MGs and study the cooling rate's influences on its atomic configuration. Meanwhile, we need to find the most appropriate glass for further mechanical deformation simulations.

In this chapter, the preparation of adequate metallic glass samples will be

presented, followed by a detailed structural characterization. The effect of quenching rate on the atomic structure and short-range order of CuZr metallic glass is discussed.

3.2 Simulation details

MD simulations in this study are built on the EAM potential using LAMMPS code. The CuZr MGs with a composition of $Cu_{64}Zr_{36}$ is chosen for its good glass forming ability as reported in the literature [51, 187]. A small box of 13,500 atoms with periodic boundary conditions (PBCs) in three directions is first selected. To simulate the random alloy of given composition, appropriate amount of Cu atoms are randomly substituted with the same number of Zr atoms in the initial structure ($Cu_{64}Zr_{36}$). The simulation box is melted for equilibration at 2000 K for 2ns, and then quenched to the glass state (1 K) with different MD cooling rate ranging from 5×10^{10}K/s to 5×10^{12} K/s at zero external pressure. NPT ensemble and Nose-Hoover thermostat and barostat methods are employed and the conjugated gradient method is used to finally optimize the inherent structure. Simulations are carried out five times with different initial configuration to ensure data accuracy. The obtained metallic glass sample configuration is illustrated in Figure 3.1.

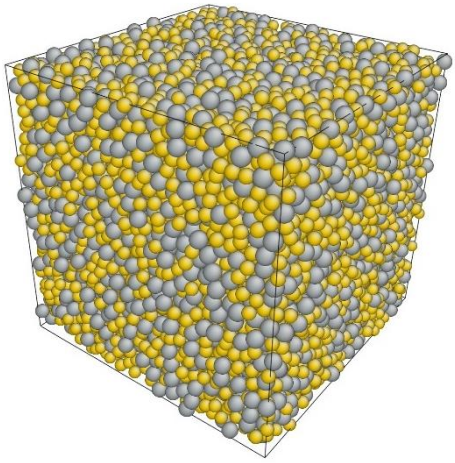

Figure 3.1 Configuration of $Cu_{64}Zr_{36}$ metallic glass sample. Yellow particles represent Cu atoms and gray for Zr atoms.

3.3 Results

3.3.1 Atomic energy and volume evolution

Figure 3.2 displays the evolution of average energy per atom and atomic volume of $Cu_{64}Zr_{36}$ metallic glass during quenching at various rates. The first thing which stands out is that a change of gradient is observed in both energy-temperature and volume-temperature evolution curves, which spans over an extended temperature interval of about 200K, from 900K to 700K. The energy and volume curves show a typical glass forming pattern and this gradient transition is consistent with the reported glass transition temperature of 746 K [188]. Under a fast quenching rate of 5×10^{12}K/s, as illustrated in Figure 3.2, the step of gradient change seems to be missing. While for slower cooling rates, like 5×10^{10}K/s, this gradient change is more obvious which suggests a larger

transition on both system energy and atomic volume and is more similar to the experimental glass formation [52, 58, 189].

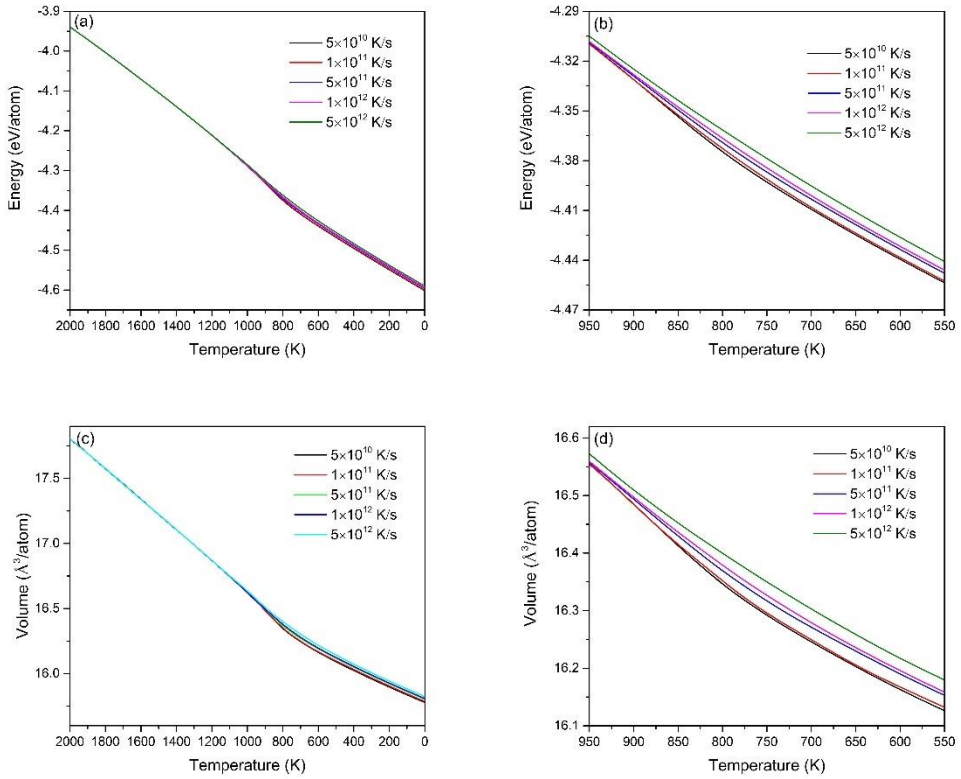

Figure 3.2 Evolution of energy (a), (b) and volume (c), (d) during melt-quenching of $Cu_{64}Zr_{36}$ under different cooling rates. (b) and (d) show the detail changes around the glass transition temperature of 746 K.

3.3.2 Pair distribution functions

In order to characterize the phase transformation during the quenching process and clarify whether a crystalline phase forms in the sample, the PDF of both Cu-Zr, Cu-Cu and Zr-Zr pairs with different cooling rates are presented in Figure 3.3 . As we can see, both samples are fully amorphous and no indication

or presence of a crystalline phase appears. The first peak at around 3 angstroms indicates that the sample has short-range ordered structure. The second peak pops up at around 5 angstroms and the PDF patterns converge to unity at a distance above 8 angstroms, indicating the absence of any long-range order. Figure 3.4 Partial radial distribution functions for (a-c) Cu36Zr64 and (d-f) Cu64Zr36 MGs obtained with different cooling rates. Figure 3.4 presents the simulated partial distribution functions obtained by Ritter [110]. As a comparison, a good agreement has been found with the simulated results done by this work and literature (Figure 3.4 (d), (e) and (f)), indicating that the simulation parameters used here is credible.

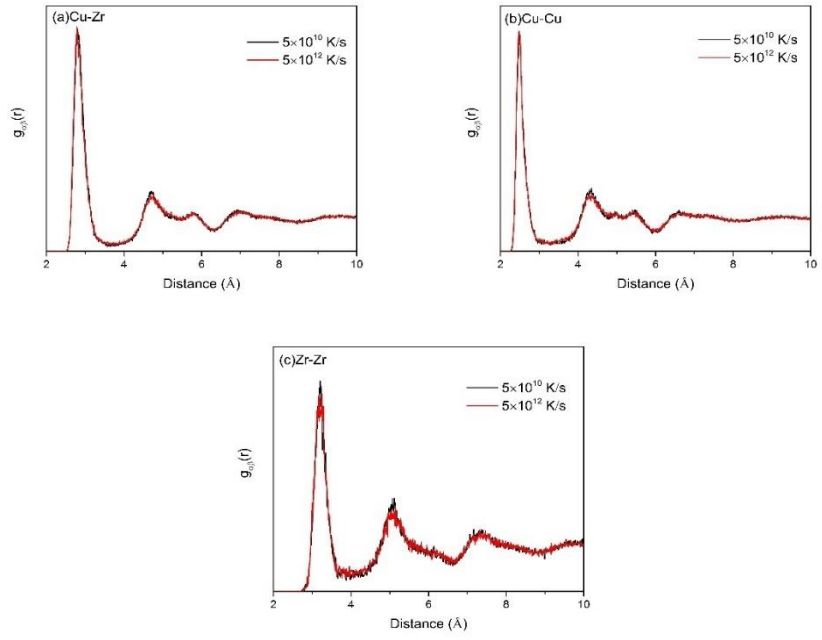

Figure 3.3 Simulated partial distribution functions for (a) Cu-Zr, (b) Cu-Cu and (c) Zr-Zr pairs of $Cu_{64}Zr_{36}$ glasses quenched with cooling rates of 5×10^{10} K/s and 5×10^{12} K/s, respectively.

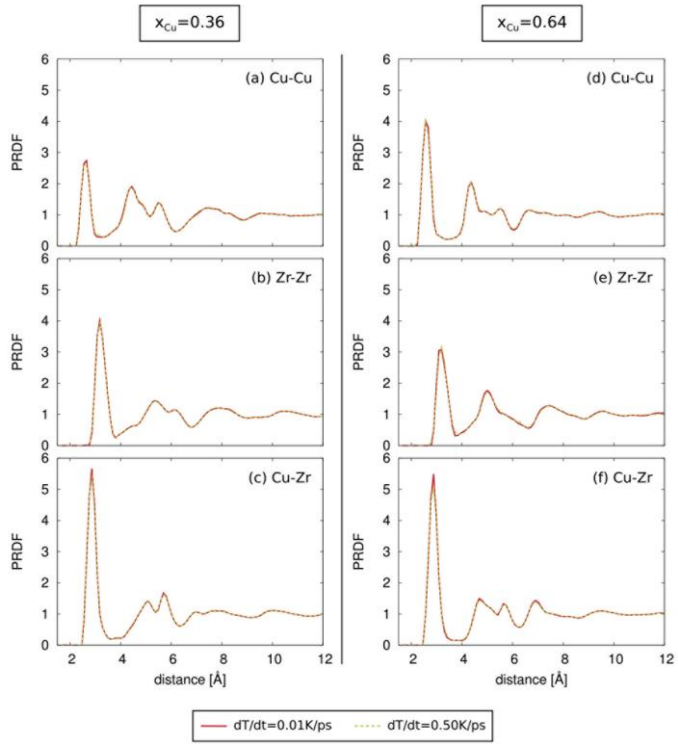

Figure 3.4 Partial radial distribution functions for (a-c) Cu36Zr64 and (d-f) Cu64Zr36 MGs obtained with different cooling rates.

In order to explicitly uncover the characteristics of glass forming during quenching, we calculated the PDF of $Cu_{64}Zr_{36}$ with a low quenching rate of 5×10^{10} K/s at different temperature, as shown in Figure 3.5. According to the figure, a sharpening of the first peak and a splitting of the second peak are shown around 800 K, which are the typical indicators for the formation of a glass phase [190, 191]. The glass transition temperature is in good agreement with the energy per atom, atomic volume changes and also the value reported in the literature (746 K) [51, 52].

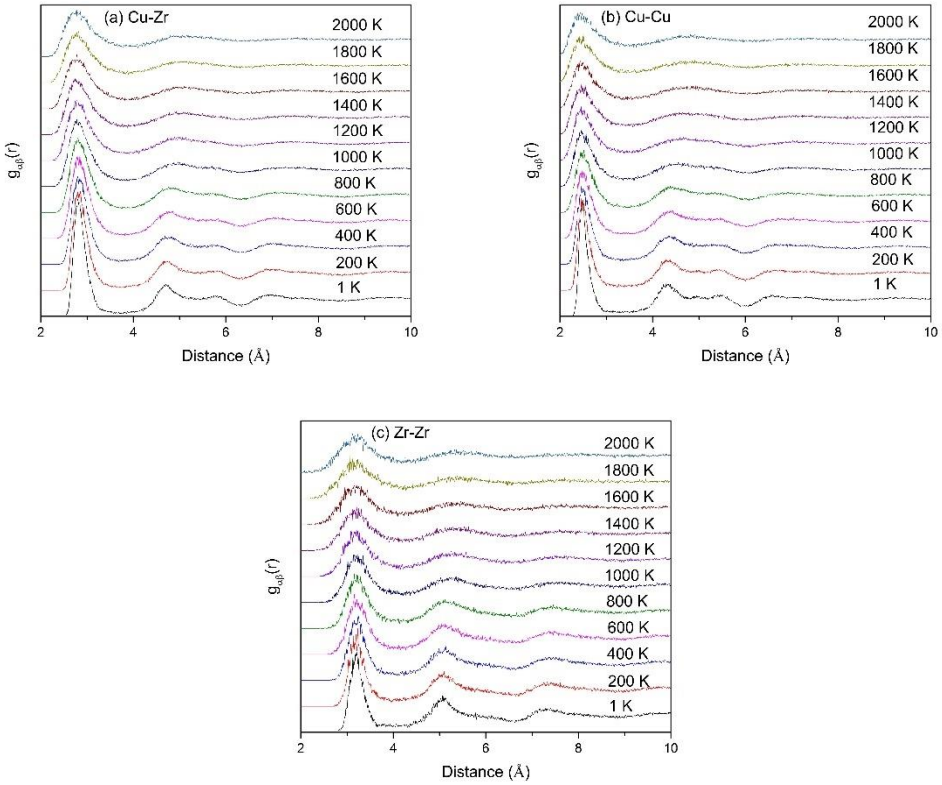

Figure 3.5 Partial distribution functions for different temperatures during the formation of $Cu_{64}Zr_{36}$ glasses. The cooling rate is 5×10^{10} K/s.

3.3.3 Voronoi method analysis

Figure 3.6 presents the evolution of popular Cu-centered polyhedra during quenching process with a cooling rate of 5×10^{10} K/s. These polyhedra dominant above 50% of all the Cu-center polyhedra in the system. As we can see, the fraction of these popular Cu-centered polyhedra all increase with decreasing temperature. However, the evolution of polyhedra with a Voronoi index of <0,0,12,0>, namely Full-Icosahedra (FI), is much more drastic compared to others. This dramatic increase of the FI fraction starts at a temperature of around

800 K, which is again close to the glass transition temperature. In fully quenched sample, the fraction of FI can take over 20% of all the Cu-centered polyhedra. This observation is consistent with other simulation works [11, 35] and directly demonstrates the SRO inside the obtained glass sample.

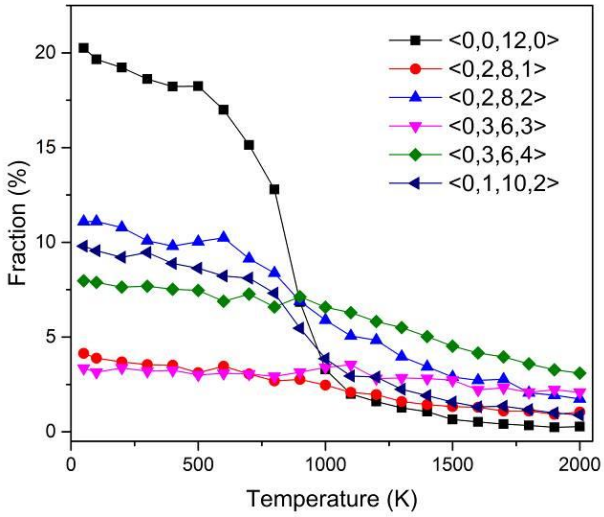

Figure 3.6 Evolution of popular Cu-centered polyhedra during quenching process with a cooling rate of 5×10^{10} K/s.

Next, the number and fraction of Cu-centered full-icosahedra in the simulated glass samples is compared at different quenching rates, as has been illustrated in Figure 3.7. It is obvious that the sample with the lowest quenching rate, i.e. 5×10^{10} K/s has a more FI fraction (above 20% among all the Cu-centered polyhedra) than that of the sample with the highest quenching rate, i.e. 5×10^{12} K/s (about 13% among all the Cu-centered polyhedra).

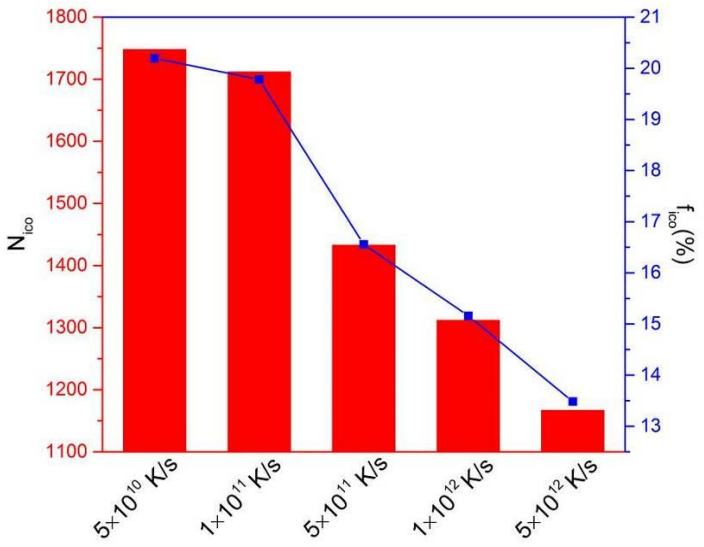

Figure 3.7 The number and fraction of full-icosahedra with different cooling rates.

However, as illustrated in Figure 3.8, for other types of Cu-centered Voronoi polyhedra and Zr-centered Voronoi polyhedra, the effect of quenching rate is not obvious. In fact, as we can see, under different quenching rates, the fraction of these popular polyhedra in the final simulated metallic glass samples basically remains unchanged. For example, the Cu-centered polyhedra with Voronoi index of <0, 2, 8 ,2> under the lowest and highest cooling rate is 11.3% and 11%, respectively; and the Zr-centered polyhedra with Voronoi index of <0, 1, 10 ,5> under the lowest and highest cooling rate is 12% and 10.6%, respectively. No significant variation is observed under different cooling rates.

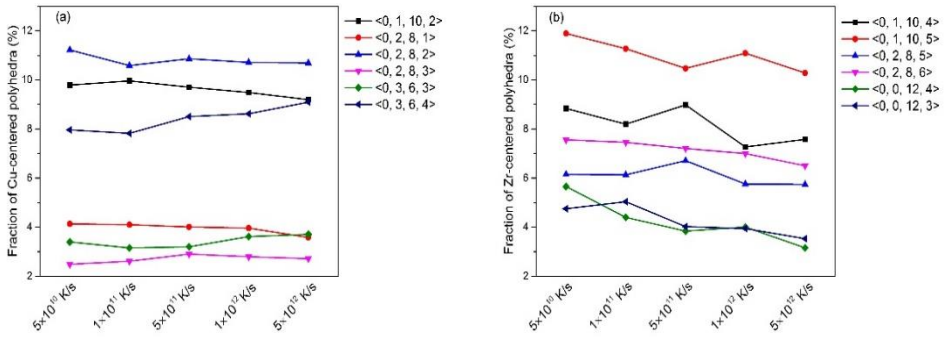

Figure 3.8 Fraction of other popular Voronoi cells around Cu (a) and Zr (b) atoms in the simulated $Cu_{64}Zr_{36}$ MGs under different quenching rates.

3.4 Discussions

3.4.1 Energy changes during glass formation

From Figure 3.2, it is clear that the sample under a lower quenching rate suffered a more obvious change in atomic energy during the glass formation. This sudden change in energy around the glass formation temperature suggests a transformation in atomic structure during this temperature range. This is in agreement with Frank's hypothesis [192] who suggest that metallic melts have a tendency for ordering which enables them to be undercooled. However, the degree of ordering correspond to the particular temperature is often too hard for the metallic melt to achieve when under a high cooling rate. Apparently, in this work, a quenching rate of 5×10^{12}K/s is so high that the decrease in temperature is faster than the kinetic for ordering. Yet under a lower quenching rate of 5×10^{10}K/s, the considerable high driving force for ordering in the supercooled

melt can lead to a sudden creation of SRO. Such an ordering process can be reflected in Figure 3.6, the strong increase of FI fraction between 1100 K and 500 K. And for the sample with cooling rate of 5×10^{12}K/s, the increase in FI fraction is far less, as can be seen in Figure 3.7, as the ordering process cannot take place. Therefore, the change of gradient in the energy curve can be explained.

3.4.2 PDF analysis

In Figure 3.3, there exists a slight difference of first peak position in the PDF pattern among Cu-Cu, Cu-Zr and Zr-Zr pairs. The Cu-Cu pair exhibits the nearest first peak position while Zr-Zr pair exhibits the farthest. This could be simply explained due to the different atomic volume. Since the atomic volume of Cu atom is smaller than that of the Zr atom, the pair of two atoms with smaller volumes will has a nearer first peak position. It is further interesting to note that the PDF patterns of glasses prepared with different cooling rates look quite similar, despite the intensity of both the first and the second peaks. For the slow-quenching sample, the peak intensities in the PDF pattern are sharper; while for fast-quenching sample, the peaks appear to be broader. This phenomenon has been observed by previous studies and it is assumed to be caused by the reduction of disclination density [193-195] and leads to a more ordered structure. However, as discussed in Chapter 2.7.1, PDF is only a statistical average

projection of the structure on one dimension [21], thus a more detailed structural analysis like Voronoi Tessellation method is needed to reveal their differences.

Comparing the PDF patterns of different pairs in Figure 3.5, it is interesting to note that the first peak of Cu-Zr pairs (unlike pairs) is sharper than those of Zr-Zr and Cu-Cu pairs (like pairs). According to Waseda and Chen [196], this suggests a preferred interaction of unlike atom pairs in the $Cu_{64}Zr_{36}$ metallic glass during the quenching. As the temperature decreases, the strong interactions between unlike atom pairs tend to destroy the intrinsic Cu-Cu pair and lead Cu atoms to bond with Zr atoms, resulting in a sharpening of PDF patterns of Cu-Zr pairs.

Based on the volume evolution curves and PDF patterns of obtained glasses, we can calculate many physical parameters such as atomic density, mass density and mean nearest neighbor distance and then compare these with other simulations and experimental works. The mean nearest neighbor distance r_{ij}, with i, j = Cu and Zr, is extracted from the PDF pattern according to the position of the first peak. These results are presented in Table 3.1, along with experimental data from the work of Mattern et al. [39]. The resulting densities are ρ_0 = 63.38 nm^{-3} and ρ = 7.73 $g.cm^{-3}$, showing a good consistency with both simulated and experimental data. This suggests that simulated glasses in this work are credible.

Table 3.1 Atomic density, mass density and mean nearest neighbor distance r_{ij} extracted from PDF patterns for simulated and laboratory-made glasses.

	ρ_0 [nm^{-3}]	ρ [g.cm^{-3}]	r_{CuZr}	r_{CuCu}	r_{ZrZr}	Ref.
$Cu_{64}Zr_{36}$ (Sim.)	63.38	7.73	2.805	2.52	3.17	This
$Cu_{64}Zr_{36}$ (Sim.)	61.9	7.57	2.87	2.61	3.16	[197]
$Cu_{65}Zr_{35}$ (Exp.)	63.7	7.75	2.75	2.63	3.08	[39]

3.4.3 Short-range-order analysis

In Figure 3.6, the drastic increase of Cu-centered full-icosahedra during glass formation is confirmed. As have discussed in Chapter 1.2.4, the Cu-centered <0, 0, 12, 0> clusters have a lower average configurational potential energy than other clusters [36]; therefore, the sudden increase in FI fraction can corroborate to the precipitate drop in atomic energy curve in Figure 3.2. Also, Cheng et al. [34] have studied the influence of Cu-centered full-icosahedra on the local atomic mobility. They found that the majority of particles in the immobile regions are confirmed to be associated with the <0, 0, 12, 0>icosahedra, while the fraction of <0, 0, 12, 0> icosahedra is minimal in the mobile regions. Therefore, the degree of Cu-centered FI order and its evolution with cooling appears to be the structural signature of the thermodynamic and kinetic behaviors of $Cu_{64}Zr_{36}$ supercooled liquids [25].

Figure 3.7 demonstrates the cooling rate effect on the Cu-centered FI fraction. The obvious difference among samples with different quenching rates means

that cooling rate can have a vital influence on the local structure of the simulated samples despite the similarity of PDF patterns. Samples with lower cooling rates have more organized local configuration and more efficient packing of atoms because the system has more time to react in order to reduce the total energy when the cooling is slow [33]. However, the evolution of Zr-centered polyhedra is mainly insensitive to the cooling rate. Compared to the drastic changes of Cu-centered FI under different quenching rates, it is obvious that Cu-centered FI is more sensitive to the cooling rate. This finding is consistent with the experimental observations made by Ma et al. [60], and justifies the approach to examine the Cu-Zr metallic glasses structure from the perspective of Cu-centered full-icosahedra.

3.5 Conclusions

In this chapter, the melt-quenching of $Cu_{64}Zr_{36}$ glass with different cooling rates was successfully simulated. When quenched with a lower rate, a change of gradient on both energy-temperature and volume-temperature curves is detected; while under a faster cooling rate, this feature gradually disappears. Referencing to the PDF patterns, a fully amorphous structure is observed. The typical glass formation signatures of sharpening of the first peak and splitting of the second appear during the glass transition temperature region. The atomic density, mass density and mean nearest neighbor distance extracted from PDF patterns are

found to agree well with those reported in literatures. Local structure analysis shows an increase in popular Cu-centered polyhedra during the quenching process. The analysis on the effect of cooling rate on the fraction and number of Cu-centered and Zr-centered polyhedra reveals that the Cu-centered FI is most sensitive to the quenching rate. While for other Cu-centered polyhedra and all Zr-centered polyhedra, the dependence of cooling rate is not as obvious. This also suggests that samples with lower cooling rate have more ordered short-range structures compared to those with higher cooling rates.

Based on the above analysis, it has been proved that the $Cu_{64}Zr_{36}$ metallic glass with a cooling rate of 5×10^{10}K/s simulated in this study has a more ordered structure: the energy and volume changes during the quenching is more similar to that of the experimental observations; and the structural characterization reveals a more ordered structure. Thus, in the following chapters, this small configuration containing 13,500 atoms will be used to construct larger samples which will then be used in the tensile simulations.

Chapter 4 Effect of notch geometry on the deformation behavior of CuZr metallic glasses

4.1 Introduction

The deformation mechanism of metallic glasses has always been a research hotspot since the beginning of metallic glasses development. Although MGs have been found to have superior strength, the lack of plasticity at room temperature has greatly restricted their applications. The formation of shear bands has been widely accepted as the main cause of the limited plastic strain and therefore ways to prevent rapid propagation of shear bands and promote multiple shear bands have been major approaches to enhance the plasticity, such as to introduce micrometer-size ductile crystalline phase [198], to increase the Poisson's ratio [66, 67] and to form nano-size structural heterogeneity [69, 71].

Many simulation works have paid attention to the shear localization process of metallic glasses under uniaxial tensile loading and shear loading. The local strain distribution and structural evolution have been thoroughly discussed in previous research [199-202]. However, few papers have covered the deformation mechanism of metallic glass under multiaxial stress state and local structure evolutions. As mentioned in Chapter 1.3.3, it is possible that, under multiaxial stress state, a strain-hardening phenomenon can appear when the

annihilation of free volume surpasses its generation. Therefore, it is necessary to use MD simulation to study the plastic deformation behavior of MGs and support these experimental results. To achieve the multiaxial stress states needed, simulation samples with different notch depth are created in order to perform uniaxial tensile loading where the stress states around notch part is one of the triaxial stress state and compare these with notch free samples. The deformation mechanism, involving local free volume evolution, local structure transformation and local temperature evolution are discussed in this chapter.

4.2 Simulation details

For the mechanical simulation, large pillar samples containing ~ 600,000 atoms were constructed by replications of the small configurations (13,500 atoms) as in the previous chapter. A cooling rate of 5×10^{10}K/s with annealing for 200 ps was used. Notches were created by eliminating atoms in the center of the samples. The final pillar sample has a diameter of 20 nm in X- and Y- directions and length of 30 nm in the Z-direction, with a notch depth from 0 to 6 nm, in ascending order of 1 nm, as illustrated in Figure 4.1. The notch width is 3 nm for each sample. PBCs were applied in the Z-direction while free surface was used in the X- and Y- directions to allow shear band to take place. Uniaxial loading was employed in the Z-direction with a constant strain rate of 10^8 s^{-1} (relatively slow for MD simulations). The stress is calculated from the normal

tensor component of virial stress along the loading Z-direction. Atomic configurations analysis was done by using Voronoi Tessellation method for full icosahedra statistics and Voronoi volume calculations. For each geometry, simulations were carried out five times and a different initial configuration was used each time to ensure the data accuracy. The summary of the simulation samples discussed in this chapter are listed in Table 4.1.

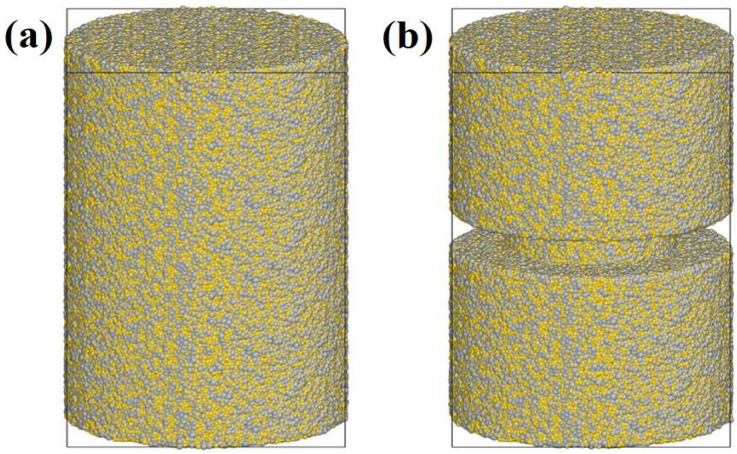

Figure 4.1 The configuration of unnotched (a) and 3 nm notched sample (b). The grey atoms represent Zr atoms and yellow for Cu atoms.

Table 4.1 Summary of simulation setups in Chapter 4

Code	Notch depth	Strain rate
TC0	0	10^8 s^{-1}
TC2	2 nm	10^8 s^{-1}
TC3	3 nm	10^8 s^{-1}
TC4	4 nm	10^8 s^{-1}
TC5	5 nm	10^8 s^{-1}

4.3 Results

4.3.1 Stress-strain curves

Figure 4.2 shows the engineering stress (σ) –strain (ε) curve of samples with different depth of notches. The engineering stress here is defined as $F(t)/S$, where $F(t)$ is the current load, t is the loading time and S is the initial cross sectional area of the specimen, which is $10 \times 10 \times \pi$ nm^2 in this case. Engineering strain here is defined as $(L(t) - L)/L$ with L and $L(t)$ for the initial and current length in the Z-direction, respectively. For the sample without notch, it shows a linear increase in engineering stress in the initial elastic loading stage up to $\varepsilon = 0.04$. With further deformation, the curve deviates from linearity and follows by a sudden drop of stress observed at $\varepsilon \sim 0.06$, showing a yielding stress of about 2.0 GPa. While for the notched samples, the yielding loading is significantly reduced. With increasing notch depth, the yielding stress decreases accordingly. For the sample with a 5 nm notch, the yielding stress reduced to only 0.75 GPa.

To uncover the true mechanical behavior of notched MGs, Figure 4.3 shows the true stress-strain curves for unnotched and different notched samples. True stress here is defined as $F(t)/S(t)$ where $S(t)$ is the current cross sectional area of the specimen during loading. The true strain is defined as $(S - S(t))/S$ [203]. The 4 nm notched specimen in Figure 4.3 reveals a linear elastic stage until true

strain reaches 0.04, and then plastic deformation takes place, and a maximum strength of 3.25 GPa was observed at a true strain of 0.13. Compared to the unnotched sample whose true stress reaches its peak at strain equal to 0.06, there is an obvious increase in both true failure strength and strain [97].

Figure 4.4 indicates the cross sectional area change of a 4 nm notched sample during loading. We can see that at the early stage, the reduction in $S(t)$ is insignificant up to an engineering strain $\varepsilon = 0.04$, from 112 nm^2 to 103 nm^2, which corresponds to the linear elastic stage. After that $S(t)$ drops quickly to 55 nm^2 at engineering strain equals to 0.1, showing an obvious necking phenomenon.

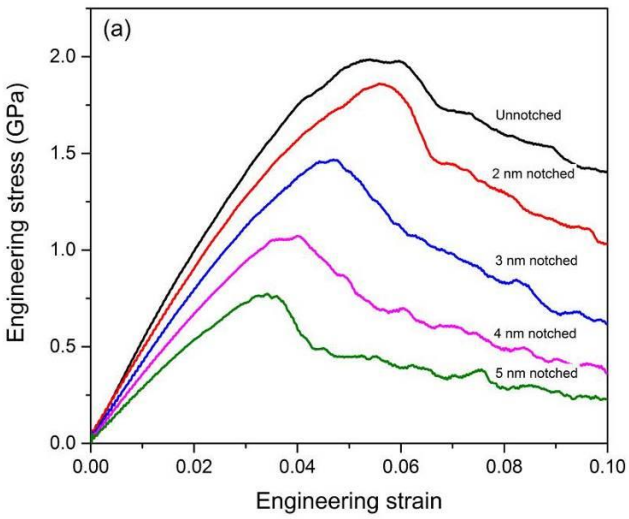

Figure 4.2 The engineering stress-strain curves of cylinder pillar samples with different notch depth. The diameter of unnotched sample is 20 nm and four samples with depth in ascending order (2 nm, 3 nm, 4 nm and 5 nm) are marked in separate colors.

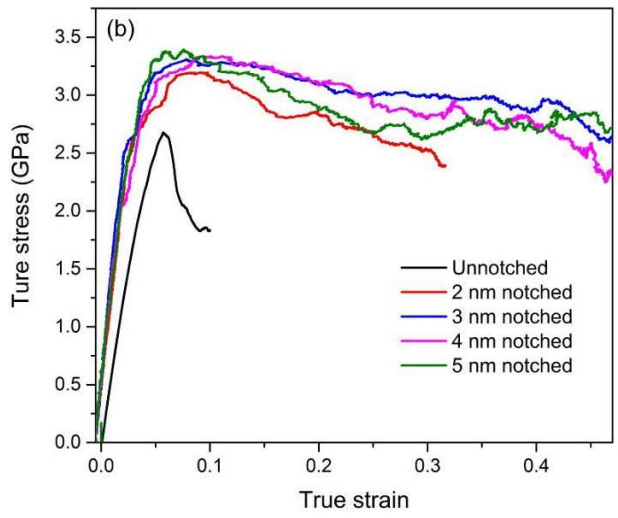

Figure 4.3 The true stress-strain curves for unnotched and samples with different notch depth.

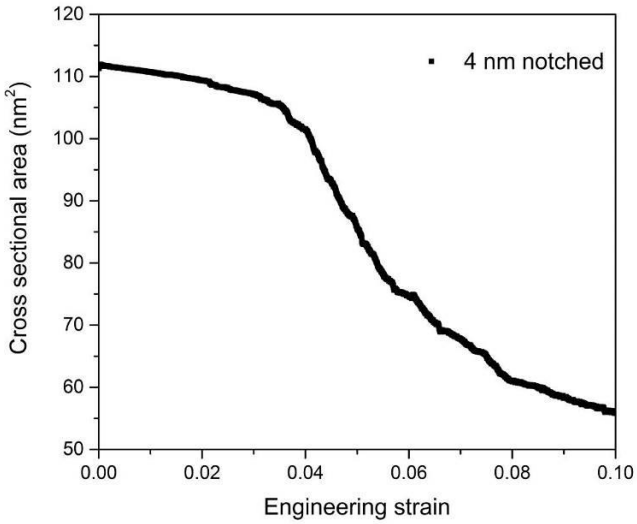

Figure 4.4 The change of a cross sectional area of 4 nm notched sample during loading.

4.3.2 Local strain distributions

Atomic local shear strain η_i^{mises} was used to analyze the deformation process

[177], with the relaxed glass prior to loading as reference. Figure 4.5 directly shows the different deformation mode between notched and unnotched samples during the tensile deformation. For the unnotched sample, a single shear band is formed by the higher η_i^{mises} strain monitored, penetrating across the entire sample, at approximately 45° relative to the loading direction. The sample is entirely tilted parallel to the Z-direction due to the free surface boundary condition we applied to X and Y directions, showing a typical MG deformation. For samples with relatively low notch depth (2 nm), two narrow shear bands starting from the notch tip and interacting in the lower middle part of the sample are shown in Figure 4.5 (b), forming a V-shaped plastic deformed region. This observation corresponds the experimental results by Zhao et al. [204]. When the notch depth increases to 5 nm, as showed in Figure 4.5 (c), the deformation mode changed to necking, similar to the experimental finding by Wang et al. [97]. Deformation only takes place inside the notch, leaving the rest of the area barely deformed. The plastic deformation starts earlier on the 5 nm notched sample (at $\varepsilon = 0.04$), compared to the 2 nm notched and unnotched sample (at $\varepsilon = 0.06$), which is consistent with what has been shown in the engineering stress-strain curves.

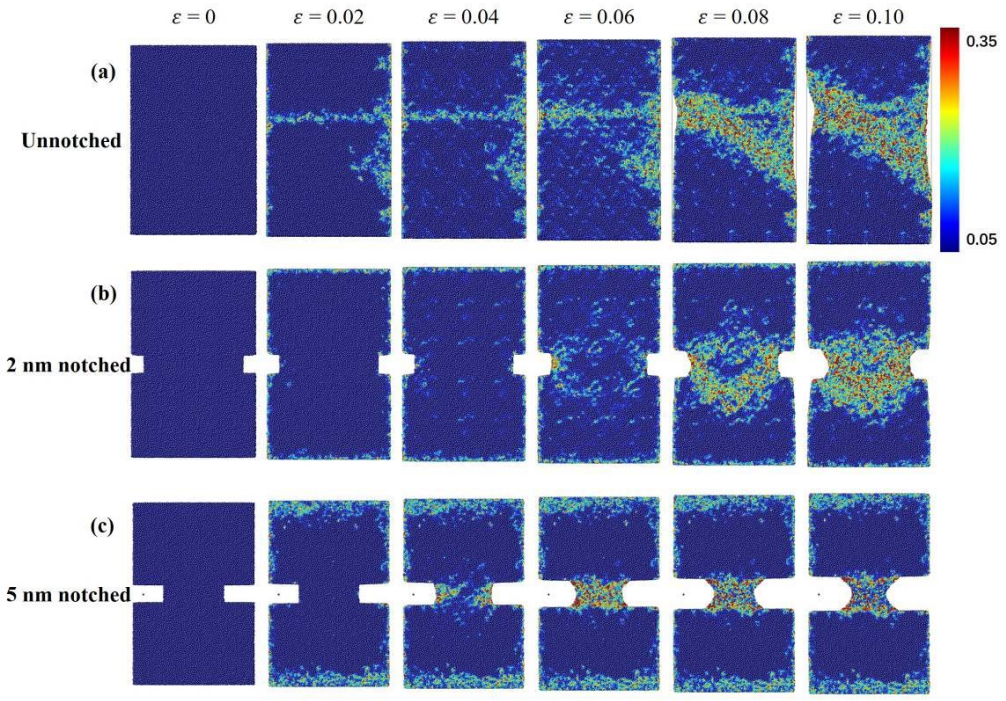

Figure 4.5 Projected views of the atom configurations at different engineering strain, showing the deformation mode of unnotched sample (a) and 2 nm (b), 5 nm (c) notched sample, respectively. The color indicates the local Von Mises strain.

The further tensile simulations of 2 nm and 5 nm notched samples up to ε = 0.2 were also performed. For the 2 nm notched sample, since the two small shear bands interact with each other to the region outside the notch part, during further growth, these plastic deformed regions will merge and penetrate across the sample, forming a shear-band-like region, as shown in Figure 4.6 (a). While for 5 nm notched sample, the necking continues until the sample nearly fractures, as shown in Figure 4.6 (b). The plastic deformation concentrate in the necking region.

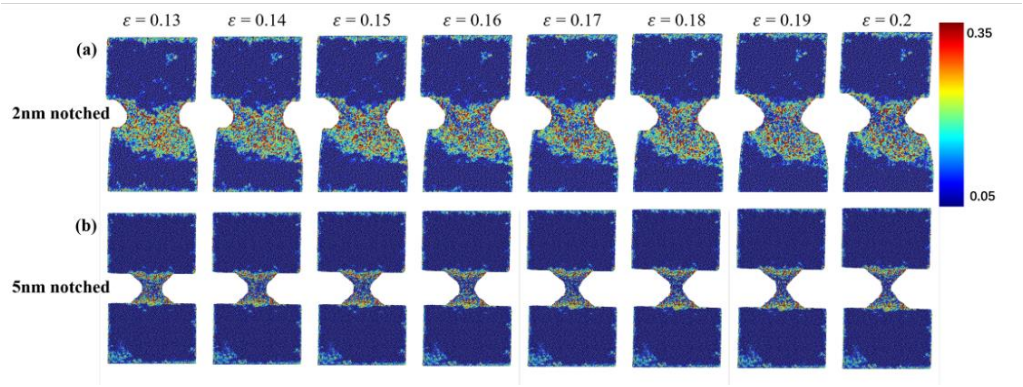

Figure 4.6 Further plastic deformation of 2 nm (a) and 5 nm (b) notched sample up to engineering strain equals to 0.2.

4.3.3 Voronoi volume evolutions

In order to investigate the structural evolution of the severely deformed region in various samples, we have calculated the Voronoi volume changes during tensile elongation. Figure 4.7 shows the mean Voronoi volume evolution of Cu-atoms and Zr-atoms among unnotched and notched samples with different geometries. We can see that for the unnotched sample, the mean Voronoi volume inside the shear band continuously increases with the tensile strain, which is consistent with many previous studies [108, 109, 205]; while for the deep notched samples (3 nm, 4 nm and 5 nm), the average Voronoi volume first increases to its peak value and then shows a clear decreasing trend. For the shallow notched sample (2 nm), in the notch center part, no single shear band or necking region is formed and the notch center is barely deformed compared to the shear localized region, which leads to a much gentler and almost linear increase in Voronoi Volume. Compared to the significant Voronoi volume

increase in shear band on the unnotched sample, the total increase in the Voronoi volume in the notch center of 2 nm notched sample is alleviated, suggesting that during plastic deformation, the local strain in the notch center is similar to the barely deformed matrix.

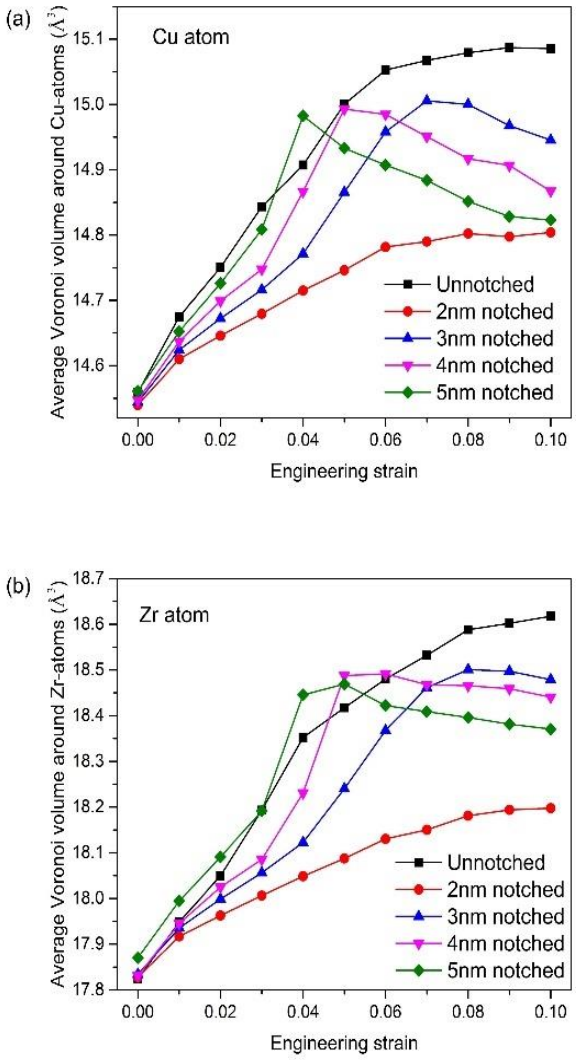

Figure 4.7 Average Voronoi volume around (a) Cu-atoms and (b) Zr-atoms during tensile deformation. For the unnotched sample, a 4 nm × 4 nm × 4 nm cubic region inside the shear band is selected for calculation; while for the notched sample, a cubic region with the same size is selected in the notch center for each sample.

4.3.4 Voronoi tessellation analysis

Figure 4.8 presents the evolution of five types of popular Cu-center polyhedra including FI for unnotched, 2 nm notched and 5 nm notched samples. The region selected here is the same with that in Figure 4.7. As we can see, only the full-icosahedra shows a distinctive change during the deformation while for others types of polyhedra, like <0, 2, 8, 1> or <0, 1, 10, 2>, the difference before and after the deformation is hardly noticeable.

For unnotched sample, the fraction of FI inside the shear band drops significantly from 20% to 9% during the entire tensile deformation. This trend is consistent with many previous works mentioned above [13, 105, 108]. For 2 nm notched sample, since the notch center undergoes a much gentler plastic deformation, the fraction of FI basically remains unchanged, similar to that in the matrix. While for 5 nm notched sample, the fraction of FI reaches its minimum of ~ 9% at an engineering strain equals to 0.06, and then recovers afterwards to ~ 11% at an engineering strain of 0.1. For other types of Cu-center polyhedra, the change of fraction is unnoticeable.

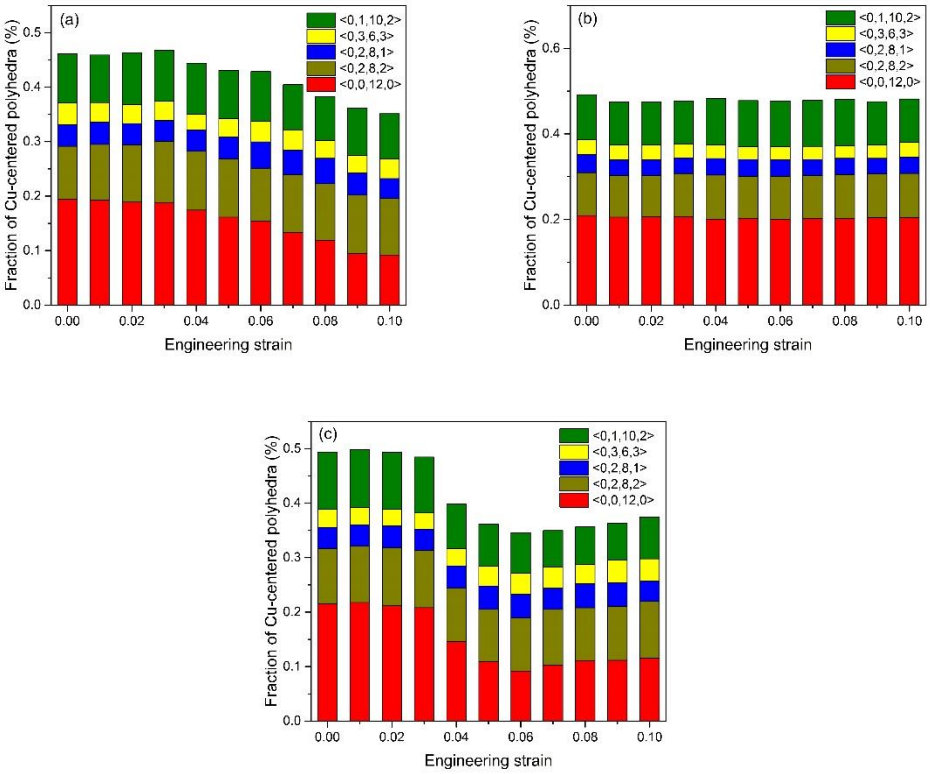

Figure 4.8 The popular Cu-centered polyhedra fraction in the shear band or notch center during the deformation of unnotched (a) 2 nm notched (b) and 5 nm notched (c) samples, respectively. The region selected here is the same as that selected in Figure 4.7.

4.3.5 Local temperature evolution

The temperature rises inside the sample during deformation was calculated, as shown in Figure 4.9. For the local temperature calculation, each atom is surrounded with a small box with dimensions of 1 nm × 1 nm × 1 nm, and the temperature is obtained by averaging the kinetic energy of atoms inside the box and then normalizing to give a temperature in Kelvin. We can see that the local temperature evolution is consistent with local shear strain distribution, as local

temperature is higher in the plastic deformed region (shear band and notch region) than that of the matrix. For unnotched sample, the local temperature rise inside the shear band is much gentler compared to that in the notched samples. For 5 nm notched sample, the local temperature in the notch center reaches its peak around an engineering strain equal to 0.04 and somewhat alleviates during plastic deformation, as further calculated in Figure 4.10. The local temperature in the center of the notch climbs up to 14 K at the beginning of plastic deformation and then gradually cools down as the plastic deformation continues.

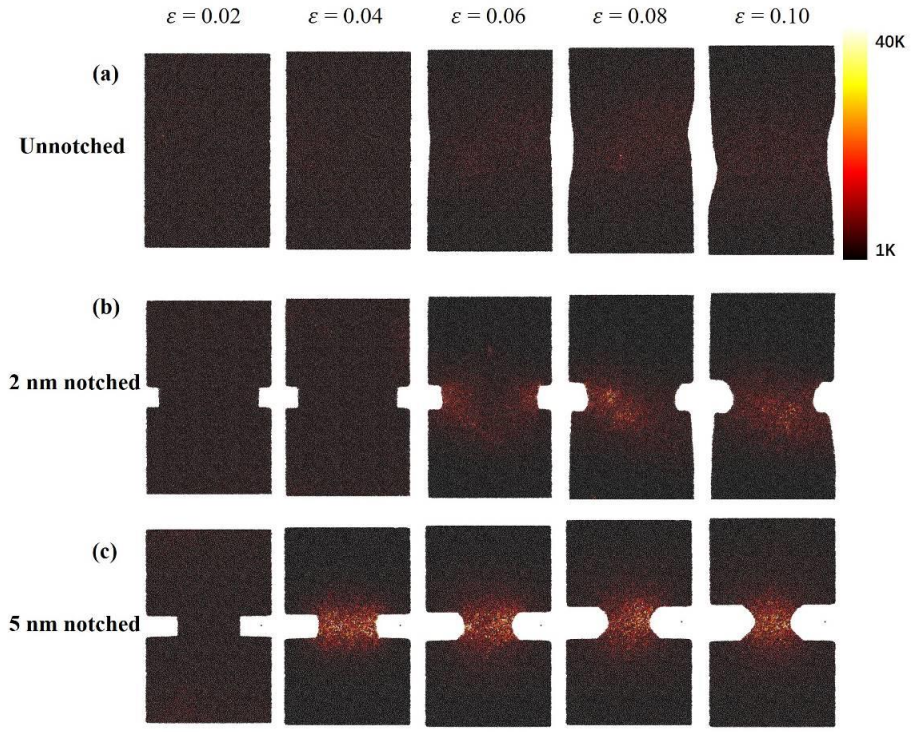

Figure 4.9 The local temperature rises in the plastic deformation region during tensile simulation. Temperature is calculated for each atom with a small box around it. The box size is 1 nm × 1 nm × 1 nm and the temperature is obtained by averaging the kinetic energy of the atoms in the box, then normalized to give a temperature in Kelvin.

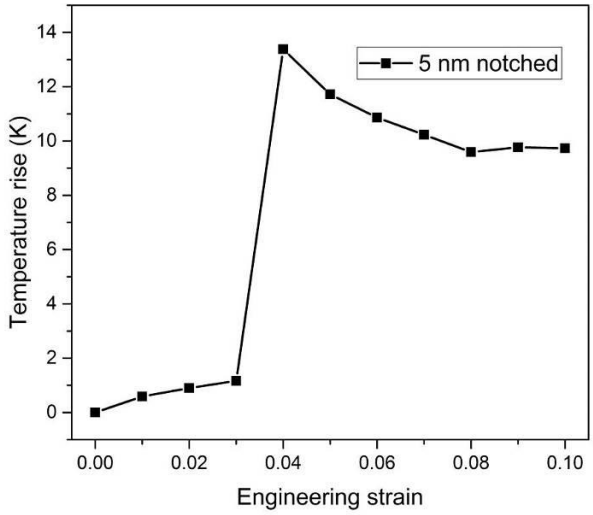

Figure 4.10 Local temperature evolution in the notch center during deformation of 5 nm notched sample. The region selected here is the same as that used in Figure 4.7.

4.4 Discussions

4.4.1 Mechanical properties

From Figure 4.2 and Figure 4.3, it is clear that notch geometry can significantly influence the mechanical strength of CuZr metallic glass. The notch depth can directly determine the triaxiality in the center of the notch region. Based on Bridgeman's analysis [206, 207], the triaxiality on 2 to 5 nm notched samples are simply calculated, with an interval of 1 nm. At the center of the notched bar, the triaxiality can be expressed as:

$$T = \frac{1}{3} + \ln\left(\frac{a}{b} + 1\right) \quad (4.1)$$

where a is the notched bar radius and b is the notch width. Figure 4.11 gives the influence of triaxiality (or notch depth) on the engineering stress and strain. A decrease in engineering stress and plasticity is observed when the triaxiality decreases, or the notch depth increases.

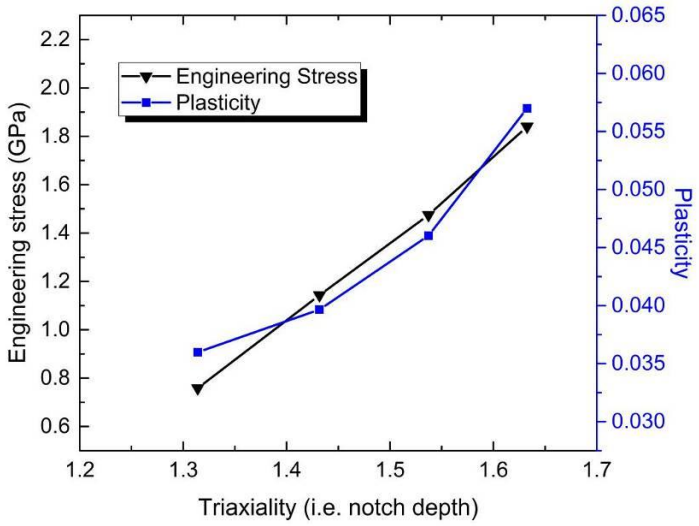

Figure 4.11 Influence of triaxiality (or notch depth) on the engineering stress and plasticity.

The true stress-strain curve in Figure 4.3 and necking mechanism in Figure 4.4 directly prove the notch strengthening phenomenon in our simulated sample, which has good agreement with the experimental findings made by Wang et al. [97]. According to their theoretical analysis, such a strain hardening phenomenon is caused by densification in the notched region and their microhardness tests and DSC tests indirectly demonstrated this densification process. However, due to the limitations of experimental techniques, it is hard

to directly reveal this densification process, or free volume annihilation, during the loading. Yet the Voronoi volume analysis in Figure 4.7 undoubtedly reveal the atomic-level mechanism of this strengthening process, and provide a strong support to the experimental results.

4.4.2 Notch effect on deformation mechanism

Figure 4.5 illustrates the different deformation mechanism in unnotched and deep notched samples. For unnotched sample, a conventional shear banding is observed. However, for deep notched sample, the shear strain is constrained in the notch part and obvious necking is shown, which explains the reduction of cross sectional area in Figure 4.4 from another perspective. Here it is also noticed that η_i^{mises} strain is larger on the notch tip than that at the notch center, as illustrated in Figure 4.5 (c). This is because the stress concentration is more severe on the tip than that in the notch center.

Next the mean local shear strain evolution in the deformed areas on all three samples was calculated, as showed in Figure 4.12. For the unnotched sample, a region in the shear band was selected for local shear strain calculation; while for notched samples, the region at the center of the notch was selected. It is clear that the local shear strain inside the shear band continuously increases along the deformation in the unnotched sample, consistent with the colored distribution map in Figure 4.5 (a). While for 2 nm notched sample, since the two small shear

bands interact outside the notch center, the local shear strain in the notch center basically remains the same as that in the matrix during the deformation. For the 5 nm notched sample, the local shear strain in the center of the notch first increases to its peak value and then decreases, matching exactly the situation what observed in Figure 4.5 (c).

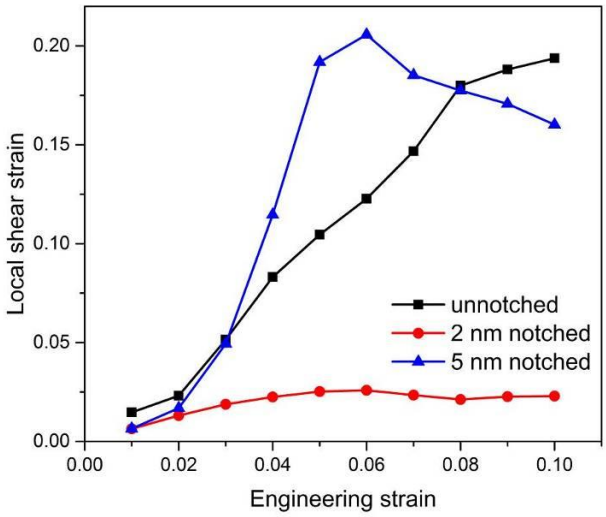

Figure 4.12 Mean local shear strain evolutions in the deformed region during the deformation. The region selected here is the same as that selected in Figure 4.7.

It should be noted that limited sample size could impose constraints on the initiation of shear localization and samples would show necking instead of shear deformation in small-volume amorphous alloys under tension [208]. To eliminate the influence of sample size, additional simulations were also performed (as illustrated in Figure 4.13) on plain pillars with the exact diameter of the notch (i.e. 10 nm). The results show a single shear band penetrating

throughout the sample. These results confirm that the notch diameter used in the simulations is large enough for the shear band formation, which in turn, testifies that the absence of a single shear band in the notched samples is due to the notch geometry in this simulation.

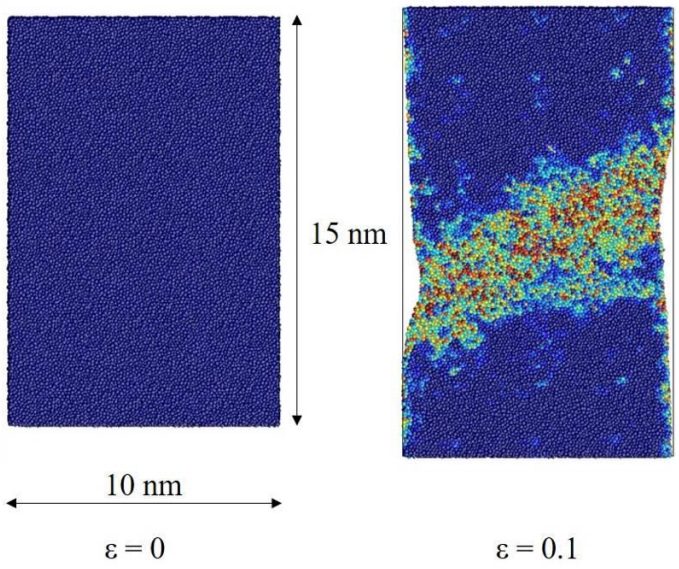

Figure 4.13 Small sample with a diameter of 10 nm before and after the uniaxial tensile simulation.

To further demonstrate the observation on transition of deformation mode influenced by notch geometry, the mechanical behavior of a single-side-notched bar specimen is studied. Figure 4.14 (a) and (b) show projected snapshots from engineering strain ε = 0.052 to 0.076 viewed from different directions. The high stress state area near the notch tip constraining the formation of shear band is further proved. As can be seen, along the direction where no notch is created, a single shear band was formed as usual (starting from the shear transformation

zones preferentially near the surfaces at the elastic regime and propagating throughout the whole body); while along the direction that notch exists, two smaller bands about 45° to the loading direction pop up near the notch tip, grow but then are constrained by the notch geometry, merging into a V-shaped deformed zone in the center, preventing the single shear band to form. These two different deformation modes presented on one sample again demonstrate our observations on the effect of how the notch geometry constrained the growth of shear band.

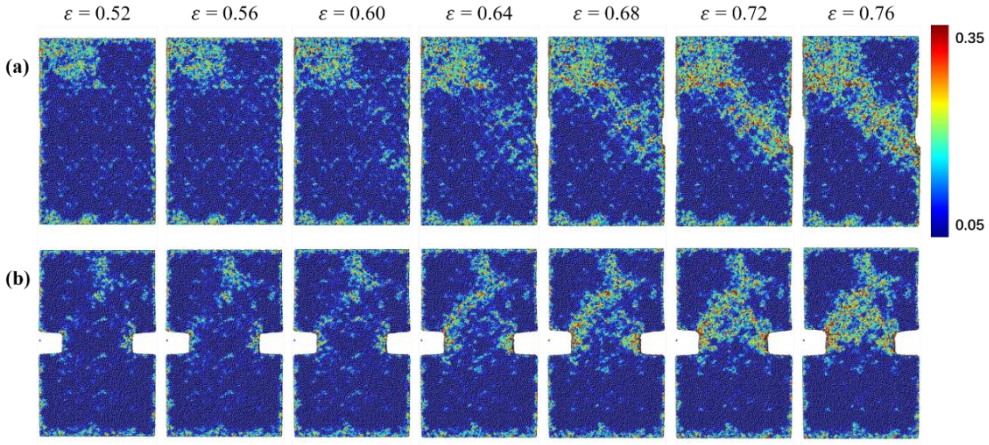

Figure 4.14 Projected snapshots of the η_i^{mises} distribution of single-side-notched sample viewed from x-direction (a) and y-direction (b). The strain ranges from engineering strain of 0.052 to 0.076, at a strain interval of 0.04.

Combining Figure 4.3 and Figure 4.5, it is obvious that from unnotched sample to deep-notched sample, there exists a transition from a brittle tensile behavior due to shear banding induced catastrophic failure to a ductile tensile behavior caused by necking induced plastic deformation. This prediction is in excellent agreement with a wide range of experiments and simulations that show MGs

deformation mode of shear banding, necking or a transition from brittle to ductile [209-216]. The brittleness usually comes from the spontaneous strain localization in the early stage of the loading. The deep-notched sample can lead to a reduced effective shear stress in the center of the notched region before the failure, as proved in Figure 4.12, therefore, considerably hindering the activation and propagation of shear band. Under this triaxiality condition, the material is able deform continuously [217].

Ordinarily, the existence of notched or any other surface imperfections in brittle material could cause catastrophic brittle failure [218]. Thus, it is natural to suspect that introduction of notch geometry on MG samples would lead to brittle fracture and decrease in yielding strength. However, recent MD simulations have illustrated that CuZr MG thin film is fairly insensitive to the presence of notch geometry [219]. While at the same time, the notch region can generate a high stress state in the notch center of the pillar samples in this thesis. As we have calculated in Chapter 1.3.3 using free volume theory, the high stress state can create a substantially higher mean stress and a substantially lower shear stress. Therefore, a large free volume annihilation and a smaller free volume generation could be possible, leading to the ductile phenomenon of CuZr MG.

4.4.3 Densification under multiaxial stress state

Figure 4.7 demonstrates the Voronoi volume annihilation phenomenon during

the plastic deformation. It is interesting to note that in deep-notched samples, the inflection points of transition from Voronoi increase to decrease is exactly where their stresses reach the peak on the engineering stress-strain curve. For example, the average Voronoi volume evolution of 4 nm notched sample reaches its peak at the engineering strain around 0.05, which corresponds to the yield strain, as showed in Figure 4.2. This phenomenon suggests that a structural relaxation occurs inside the notch center during the plastic deformation, which leads to a recovery of atomic structure and also a decrease in Voronoi volume [110]. Also, the decrease in Cu-centered Voronoi volume during the plastic deformation is larger than that of the Zr-centered Voronoi volume. This suggests that during the plastic deformation, Cu-centered Voronoi polyhedra plays a more important role than the Zr- centered ones [108].

To further prove that this densification is only caused by the notch geometry and multiaxial stress state and only takes place in the notched center, the linear scans of mean Voronoi volume distribution along the Z-direction in Figure 4.15 (a)-(f) further confirm this phenomenon. It is obtained by dividing the sample into a number of thin slices (~1 nm) parallel to the shear plane. The v_{voro} for each atom is calculated and averaged in each slice at each strain. The dotted line represents the average Voronoi volume of Cu and Zr atoms in the undeformed sample. The mean Voronoi volume expansion of Cu and Zr atoms in the unnotched sample is accompanied with the formation of a shear band. At

engineering strain ε = 0.1, the mean volume expansion at the peak is about 2~3% with respect to the mean Voronoi volume in the undeformed sample, as shown in Figure 4.15 (a) and (b), respectively. For the region beyond the shear band, Voronoi volume only increases by less than 0.05% as referenced to the undeformed sample. This much gentler generation is caused by the expansion of the whole sample volume during elastic deformation.

For 2 nm notched sample, as illustrated in Figure 4.15 (c) and (d), the generation of Voronoi volume is much gentler compared to an unnotched sample. We can see that during the plastic deformation, the Voronoi volume inside and outside the notch region both increase but in a much gentler way, and no Voronoi volume annihilation is observed. This is because during mechanical deformation, only two small shear bands were formed and then alleviated the severe shear transition, resulting to a gentle structural evolution.

While for 5nm notched sample, as shown in Figure 4.15 (e) and (f), the Voronoi volume in the center of the notch first reaches its peak value when the engineering strain is equal to 0.04 with an increase from 14.5 $Å^3$ to 15.1 $Å^3$ (for Cu atoms) and from 17.9 $Å^3$ to 18.7 $Å^3$ (for Zr atoms), after which started to decrease during the further plastic deformation. At engineering strain ε = 0.1, the mean Voronoi volume in the notch center reduced significantly, from 15.1 $Å^3$ to 14.7 $Å^3$ (for Cu atoms) and from 18.7 $Å^3$ to 18.4 $Å^3$ (for Zr atoms),

showing an obvious annihilation behavior. Both Cu and Zr Voronoi volumes show the same trend which is consistent with Voronoi volume evolution shown in Figure 4.7. Meanwhile, the pattern of Voronoi volume distribution of Cu-atoms changes from an "A" shape to an "M" shape during the loading suggesting that Voronoi volume decrease is larger in the notch center compared to that of notch tips. This observation is consistent with the local shear strain distribution in Figure 4.5 where the local strain around notch tips is larger than that of the notch center. For the region beyond notch part, the changes of Voronoi volume are also hardly noticeable, since the deformation is constrained only in the notch region.

As discussed in Chapter 1.3.4, the realistic free volume is hard to define and calculate in computer simulations, and therefore, it can usually be substituted by the Voronoi volume of an atom used in this thesis. Thus, the Voronoi decrease during plastic deformation inside the center of the notch region can be treated as a strong support to the free volume annihilation phenomenon found in the experimental results [97].

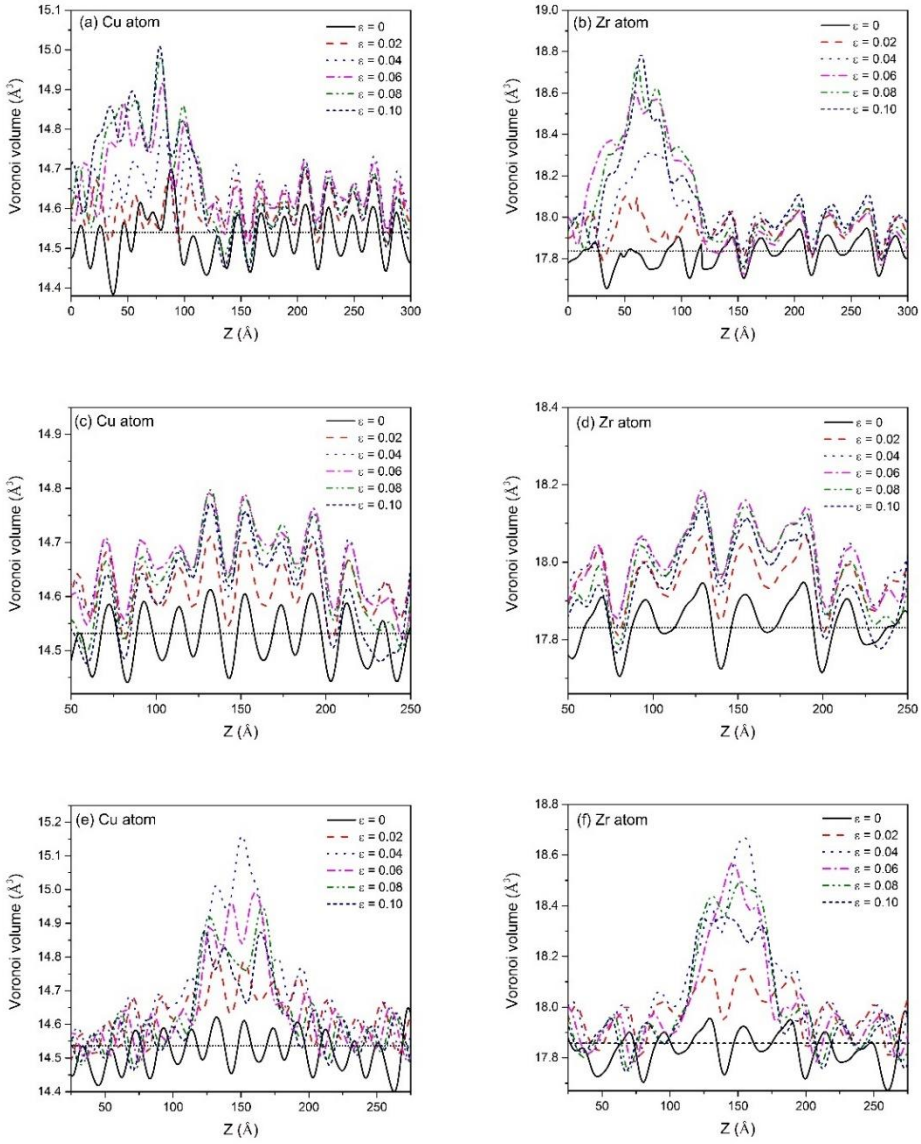

Figure 4.15 Distribution of mean Voronoi volumes along Z-direction at different engineering strains in the unnotched (a) (b) 2 nm notched (c) (d) and 5 nm notched (e) (f) samples.

The idea that deformation can lead to densification have been seen on previous studies on amorphous materials [220-222]. Bridgman and Šimon reported the densification of amorphous silica under pressure and indentation [220]; Rouxel et al. [221] found that $Zr_{35}Cu_{30}Al_{10}Ni_5$ BMG can be densified udner high

pressure. However, to the author's knowledge, no experiments on mechanical densification has been previously reported in states of net tension besides Wang et al.'s study [97]; and also no previous simulations have been reported on densification of MG during plastic deforamtion either. The simulation results presented in this thesis, combined with expereimental results carried out by Wang et al. [97] reveals an entirely different machanism of MGs.

4.4.4 Short-range-order structural evolution

Figure 4.8 shows the differences of Cu-centered FI fraction evolution among samples without notch and with different notch depth. For the unnotched sample, the fraction of Cu-centered FI keeps decreasing, showing an undoubtedly disordering phenomenon. But for 5 nm notched sample, a slight but obvious recovery of Cu-centered FI fraction is monitored during the plastic deformation. Among all the Cu-centered polyhedra. the full-icosahedra (FI), with a Voronoi index of <0, 0, 12, 0> and CN = 12, is the type most resistant to STs [34], so this can be used to characterize the glass structure. The reduction in FI fraction is closely related to the increase in shear stress [223-225]. It has been reported that metallic glasses derive their exceptional strength from a percolating backbone of short-range-order clusters, which have to be destroyed to enable deformation [226]. According to the work by Cao et al. [108], during severe shear localization, structural ordered FI will be transformed to geometrically

disordered motifs. They identified that this structural disordering process is accompanied by generation of local excess volume, and followed by temperature increase due to the energy generation caused by plastic deformation [108]. However, in the present 5 nm notched sample, clear FI fraction recovery is observed during the plastic deformation in the notch center. The present results are quite different from those of previous simulation works where Voronoi volume generation in the shear band region is dominant. Instead, the present observations suggest that during plastic deformation, the notched geometry may create a condition where the annihilation of Voronoi volume caused by diffusion can surpass its generation caused by shear banding. This will be reflected as an ordering process of the atomic structure and a recovery in FI fraction.

Such an ordering phenomenon can also be proved by the local temperature evolution in Figure 4.10. By reference to the mean Voronoi volume evolution presented in Figure 4.7 and Cu-centered FI fraction changes in Figure 4.8, it can be seen that the decrease in local temperature is accompanied by the annihilation of Voronoi volume and recovery in FI fraction. It has been reported that thermal softening is the consequence of shear localization and structural disordering [108, 227, 228], here inside the notch center, the decrease in local temperature further reinforces the present observation of structural ordering in the previous Voronoi method analysis.

4.4.5 Relationship between structure and mechanical properties

Combined all the results and discussions together, the links between notched geometry (multiaxial stress states), the topological structure inside the deformed region and the mechanical properties of $Cu_{64}Zr_{36}$ become more clear.

For the unnotched samples under uniaxial tensile loading, the destruction of Cu-centered FIs with high packing density and the creation of excess volume during the plastic deformation is obvious. During the propagation of shear band, excess volume is generated which is seen as an increase of the Voronoi volumes inside the shear band. According to Figure 4.8 (a) and the studies performed by Cao et al. [108], the Cu-centered FIs with high packing density would be disrupted during plastic deformation and the change of the cluster shape is anisotropic since the force applied on is anisotropic, as shown in Figure 1.8. Due to the uniaxial stress state (Figure 4.16 (a)), these transformations from high packing density clusters to low packing density clusters will follow the maximum shear stress direction. Once the shape and symmetry of these clusters has been altered, they are more prone to continuously shearing along the same direction, which will facilitate the propagation of the localization [108]. Eventually, the breakdown of these high packing density clusters will lead to the generation of Voronoi volume, or free volume, shown in Figure 4.7. This will in turn cause the softening of CuZr MGs, as proved in true stress-strain curves in Figure 4.3.

However, for the deep-notched samples, the center region of the notch is one of the triaxial stress states, as shown in Figure 4.16 (b). Under this loading condition, the force applied on is nearly isotropic. Therefore, such changes of FI cluster shapes along maximum shear stress condition will hardly happen when the stress state is triaxial. With the shape and symmetry of these clusters undisrupted, the backbone of Cu-centered FI will be reserved during plastic deformation, showing a relieved decrease or even recovery of Cu-centered FI fraction, as illustrated in Figure 4.8 (c). Moreover, these high packing density clusters can hinder the propagation of the localization and the deformation will be constrained in the notched region. At the same time, the deep-notched samples will exhibit a Voronoi volume or free volume annihilation phenomenon and also a densification and hardening mechanism. Therefore, the effect of notch geometry on the deformation behavior of $Cu_{64}Zr_{36}$ MGs can be fairly explained.

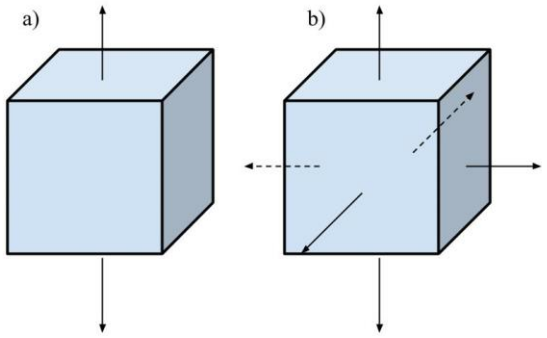

Figure 4.16 The comparison between uniaxial (a) and triaxial (b) stress states.

4.5 Conclusions

In summary, a Voronoi volume annihilation phenomenon in metallic glass by using MD simulation method has been revealed. By introducing a notched geometry into CuZr metallic glass samples, the propagation of shear band is suppressed and obvious Voronoi volume annihilation is observed in the notch center region during plastic deformation. Instead of forming a single shear band along 45° to the loading direction, necking deformation takes place on deep notched samples. Structural analysis demonstrates a recovery of Cu-centered FI fraction in the same region during plastic deformation along with the decrease in local temperature. The links between multiaxial stress states, structural evolution and mechanical behavior is revealed.

Even though the MD simulation cannot completely simulate the experimental conditions in the laboratory, it still suggests that during the plastic deformation, notch geometry can lead to free volume annihilation surpassing its generation, causing a structure ordering phenomenon. On the other hand, the simulation presented in this thesis have overcame the spatial and temporal limitations of experimental techniques and indisputably demonstrate the free volume annihilation during plastic deformation from a detailed atomic-level perspective. The deformation mechanism in the deep-notched samples, is different from that in the unnotched sample with shear banding, which enriches our understanding

of the deformation mechanism of metallic glasses.

Chapter 5 Effect of strain rate on the deformation behavior of CuZr metallic glasses

5.1 Introduction

In the previous chapter, the effect of notch geometry and multiaxial stress state on the deformation behavior of CuZr metallic glass have been discussed. It was proved that in the deep notched specimens, the recovery of Cu-centered full-icosahedra and annihilation of Voronoi volume can take place during the plastic deformation process. However, other factors, such as strain rate, can also affect the deformation mechanism of MGs. Even though many experimental and simulation studies have been carried out to investigate the strain rate sensitivity of MGs [126-128, 135, 136], the structural nature of this sensitivity still remains somewhat unknown. A few simulation studies have looked at the effect of strain rate on the mechanical behavior of MGs under shear conditions [134, 137, 138], yet none of them have covered the condition of tensile loading, not to mention the influences of notch geometry. Thus, it is necessary to investigate the effect of atomic level structural evolution under these conditions in order to understand the intrinsic mechanical nature of CuZr metallic glasses.

In this chapter, tensile testing with different strain rates will be simulated on samples without notch and with different notch depths. In order to analyze the

structural changes during plastic deformation, Voronoi methods will be applied to monitor the free volume and Cu-centered FI evolution. Cooperative shear model will be adopted to explain the strain rate effect on the yielding stress of metallic glasses.

5.2 Simulation details

For the mechanical simulation, large cylinder samples containing ~ 600,000 atoms are constructed by replications of the small configurations (13,500 atoms) performed in Chapter 3 with a cooling rate of 5×10^{10} K/s and then annealed for 200 ps. Notches are created by eliminating atoms in the center of the sample. The final cylindrical sample has a diameter of 20 nm in X- and Y- directions and length of 30 nm in the Z-direction, with notch depth of 2 nm, 4 nm and 6 nm, respectively. The notch width is 3 nm for each sample. PBCs are applied in the Z-direction while free surface was used in the X- and Y- directions to allow shear band to take place. Uniaxial loading is employed in Z-direction with strain rate ranging from 10^7 s^{-1} to 10^9 s^{-1}, as listed in Table 5.1. The stress is calculated from the normal tensor component of virial stress along the loading Z-direction. Atomic configurations analysis is done by using Voronoi Tessellation method for full-icosahedra statistics and Voronoi volume calculation. For each geometry, simulations were carried out three times and different initial configurations are used each time to ensure data accuracy.

Table 5.1 Summary of simulation setups in Chapter 5

	10^7 s^{-1}	5×10^7 s^{-1}	10^8 s^{-1}	5×10^8 s^{-1}	10^9 s^{-1}
Unnotched	TU7	TU 5.7	TU 8	TU 5.8	TU 9
2nm notched	T2_7	T2_5.7	T2_8	T2_5.8	T2_9
4nm notched	T4_7	T4_5.7	T4_8	T4_5.8	T4_9
6nm notched	T6_7	T6_5.7	T6_8	T6_5.8	T6_9

5.3 Results

5.3.1 Stress-strain curves

Figure 5.1 shows the engineering stress (σ) –strain (ε) curve of samples without notch and with different notch depths under various tensile strain rates. Firstly, we can see that the yielding tensile strength decreases as the notch depth increases, which is consistent with that have discussed in Chapter 4. For samples with the same configuration and notch geometry, when the strain rate ranges from 10^7 s^{-1} to 10^8 s^{-1}, the yielding tensile strength basically remains unchanged, suggesting that at low strain rates, the influence of loading rate is subtle to the sample. As the strain rate continuously increases to 5×10^8 s^{-1} and 10^9 s^{-1}, the yielding strength increases coordinately, which means that a high-strain-rate can lead to the strengthening of metallic glasses. For example, for the unnotched sample, the engineering yielding stress at strain rate equals to 10^7 s^{-1}, 5×10^7 s^{-1} and 10^8 s^{-1} are almost the same, while increases to 2.15 GPa (strain rate equals to 5×10^8 s^{-1}) and 2.20 GPa (strain rate equals to 10^9 s^{-1}). Also, the engineering

strain at which the tensile stress reaches to its maximum tends to be larger under the high-strain-rate, showing an increase in both yielding stress and strain.

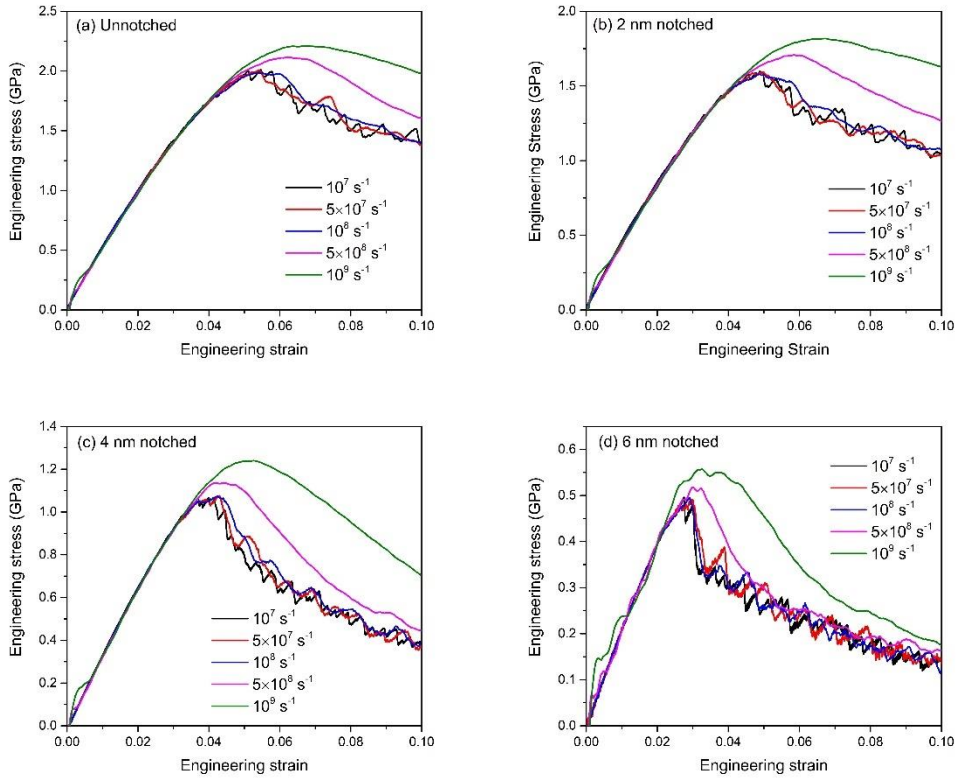

Figure 5.1 The simulated engineering stress-strain curves of cylindrical samples with different notch depths and different strain rates. The unnotched sample and three samples with notch depth in ascending order (2 nm, 4 nm and 6 nm) are marked in separate colors. The strain rate varies from 10^7 s^{-1} (slowest) to 10^9 s^{-1} (fastest).

As shown in Figure 5.2, the true stress-strain curves of the 4 nm notched sample were also calculated in the same way as presented in Chapter 4. As can be seen, similar to Figure 4.3, the curves first show a linear increase until the true strain equals to 0.04 with a true stress above 2.5 GPa and then gradually decrease. For the three samples with relatively low-strain-rates, the maximum stress basically

remains unchanged; while for the other two samples, the maximum stress increase with the increase of strain rate.

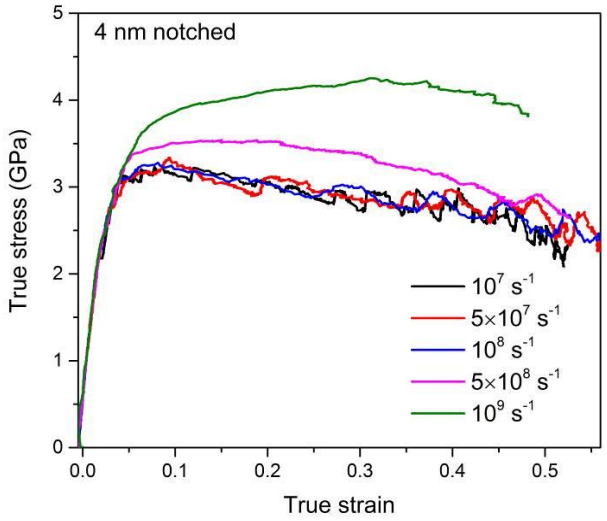

Figure 5.2 The simulated true stress-strain curves for 4 nm notched samples under different strain rates.

5.3.2 Local strain distribution

Figure 5.3 and Figure 5.4 show the projected view of atom configurations of unnotched and 4 nm notched samples under different strain rates, with the local shear strain distributions also being presented. Figure 5.3 clearly demonstrates the different deformation modes of the unnotched sample under various strain rates. For the samples with relatively slow strain rates, such as 10^7 s^{-1}, 10^8 s^{-1}, a single shear band was formed, relatively 45° to the loading direction. However, the shear band in the sample with a strain rate of 10^7 s^{-1} is relatively wider than that in the sample with a strain rate of 10^8 s^{-1}. For sample with high strain rate

of 10^9 s^{-1}, no shear banding is observed. Instead, more spread-out plastic deformed region is shown in Figure 5.3 (c), showing a more uniform spatial distribution of localization.

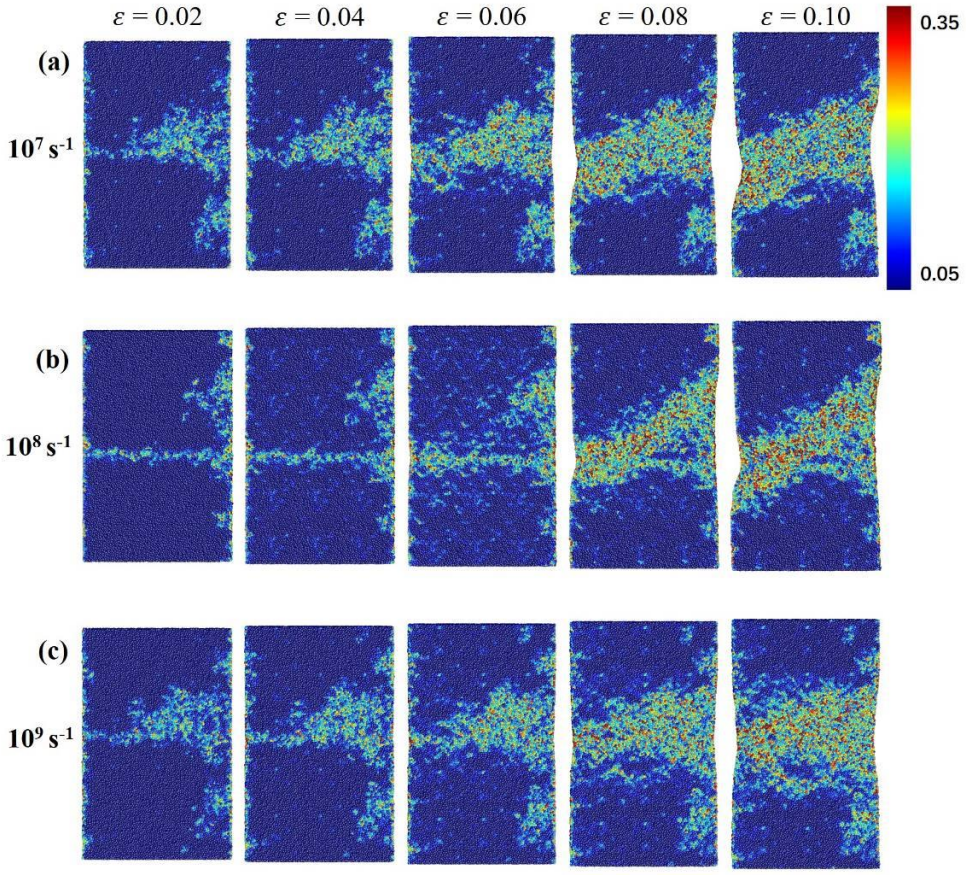

Figure 5.3 Projected views of the atom configurations at different engineering strains of the unnotched sample with three different strain rates: 10^7 s^{-1}, 10^8 s^{-1} and 10^9 s^{-1}, respectively. The color indicates the local von Mises strain.

For the 4 nm notched samples presented in Figure 5.4, even though these samples under different strain rates all show a similar necking mechanism, they still exhibit some differences. As the strain rate increases, the formation of plastic region near the notch tip is delayed. At an engineering strain rate equals

to 0.06, the plastic deformed region has already penetrated the whole notch part in the sample under a strain rate of 10^7 s^{-1}, while for the sample under a strain rate of 10^9 s^{-1}, the notch tip just begins to deform and the local shear strain in the notch center is still relatively low. This observation is consistent with our engineering stress strain curve illustrated in Figure 5.1 (d).

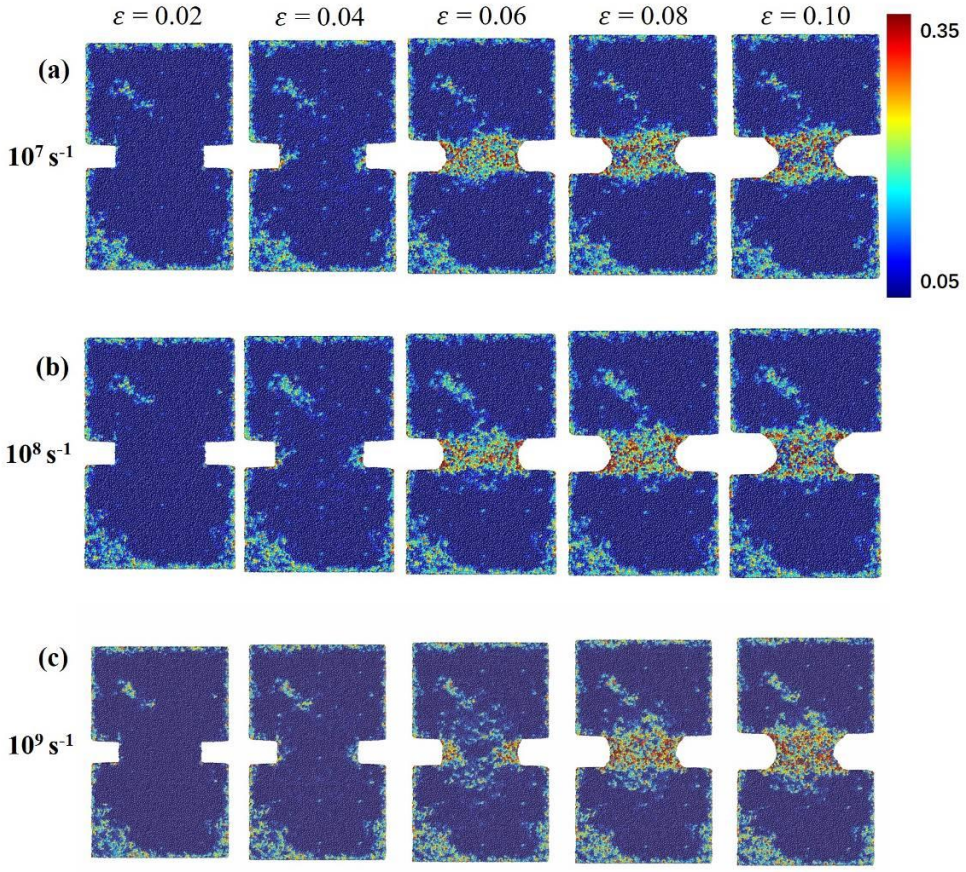

Figure 5.4 Projected views of the atom configurations at different engineering strains of the 4 nm notched sample with three different strain rates: 10^7 s^{-1}, 10^8 s^{-1} and 10^9 s^{-1}, respectively. The color indicates the local von Mises strain.

5.3.3 Voronoi volume evolution

Figure 5.5 illustrates the mean Voronoi volume evolution of Cu- and Zr-atoms

in unnotched and 4 nm notched samples under different strain rates. The calculation method is the same as used for Figure 4.7. For the unnotched sample, during the elastic deformation period, the increase of Voronoi volume basically remains the same among samples under different strain rates. While since the plastic deformation begins, samples with high-strain-rate tend to show a more dramatic increase in Voronoi volume. Based on Figure 5.5 (a) and (b), it is obvious that high strain rate can lead to a larger Voronoi volume generation on both Cu and Zr atoms in the unnotched samples.

For the 4 nm notched samples in Figure 5.5 (c) and (d), similar to the Voronoi volume evolution in Figure 4.7, the annihilation of Voronoi volume during plastic deformation is further proved. At the beginning of elastic deformation, the increase of Cu- and Zr-atoms Voronoi volume maintains the same among samples under different strain rates. However, as the plastic deformation starts, deviations begin to emerge. For samples under low-strain-rate, the Voronoi volume decreases noticeably during the plastic deformation process. In Figure 5.5 (c), samples with a strain rate below 10^8 s^{-1} all show a decrease of mean Cu-atoms Voronoi volume from 15.05 $Å^3$ to around 14.9 $Å^3$, from engineering strain equals to 0.05 to 0.10. For Zr-atoms Voronoi volume in Figure 5.5 (d), the decrease is less obvious, as observed in Chapter 4. However, it is clear that inside the sample under a strain rate of 10^9 s^{-1} in Figure 5.5 (c), the reduction of Cu-atoms Voronoi volume is almost negligible. From engineering strain equals

to 0.06 to 0.10, the mean Voronoi volume only decrease from 15.09 $Å^3$ to 15.06 $Å^3$. For Zr-atoms Voronoi volume in Figure 5.5 (d), no decrease is shown for 4 nm notched samples under strain rate of 10^9 s^{-1}. Thus, the strain rate effect on the evolution of Voronoi volumes is proved. The Voronoi annihilation phenomenon inside deep-notched samples observed in Chapter 4 can only happen under low-strain-rate.

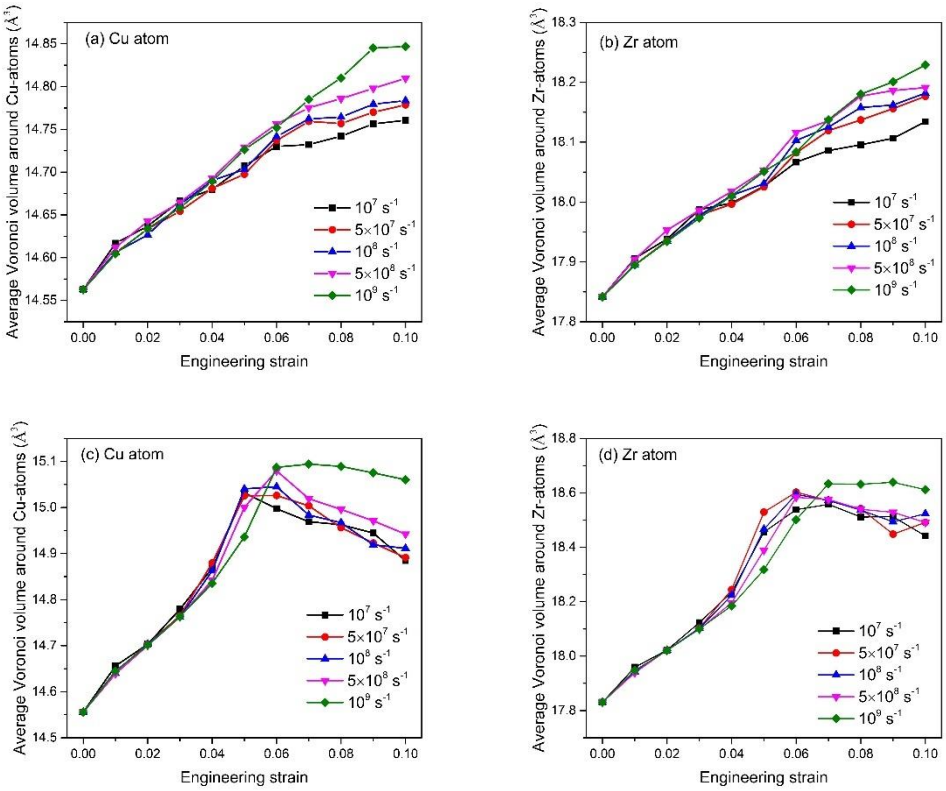

Figure 5.5 Average Voronoi volume around Cu-atoms and Zr-atoms during tensile deformation of unnotched ((a) and (b)) and 4 nm notched sample ((c) and (d)). The calculation method is the same as presented in Figure 4.7.

5.3.4 Voronoi tessellation analysis

Figure 5.6 presents the evolution of Cu-centered FI fraction during tensile

deformation of 4 nm notched samples under different strain rates. During the elastic deformation period, the changes in Cu-centered FI fraction basically remain the same among all these samples. For samples with relatively low-strain-rate, similar to Figure 4.8, a recovery of Cu-centered FI fraction is shown during the plastic deformation. The samples with slowest strain rate of 10^7 s^{-1} show the most obvious recovery, from a fraction of 0.10 to 0.12. While for samples with higher strain rates, such as the situation in the 5×10^8 s^{-1} and 10^9 s^{-1} samples, such a recovery cannot be observed. Instead, the Cu-centered FI fraction continuously decreases, just like what has been monitored in the shear band of unnotched samples in Chapter 4. The difference between samples under low-strain-rate and high-strain-rate is clearly shown.

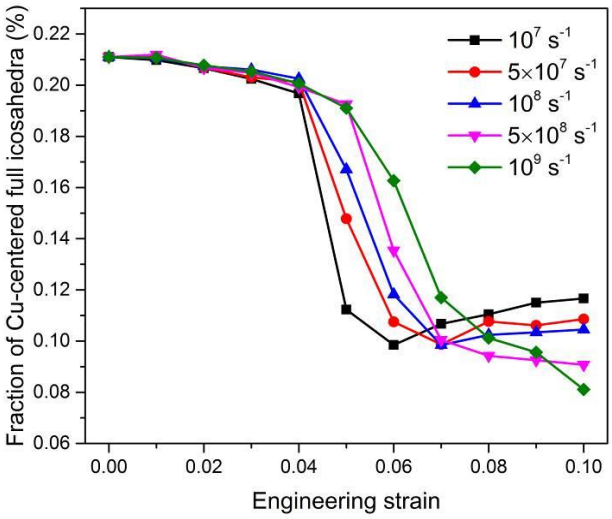

Figure 5.6 The Cu-centered full-icosahedra fraction in the notched center during the deformation of 4 nm notched samples under different strain rates. The region selected is consistent with that in Figure 5.5.

5.3.5 Local temperature evolution

Figure 5.7 presents the local temperature distribution of 4 nm notched samples under different strain rates during tensile loading. The calculation method is the same as presented in Chapter 4. From the figure, it is clear to see that the local temperature distribution is consistent with von Mises strain distribution. The local temperature rises inside the plastic deformed region. As the strain rate increases, a "hotter" notched region is illustrated in Figure 5.7 (b) and (c), suggesting that high strain rate can cause a more dramatic local temperature rise inside the notched region.

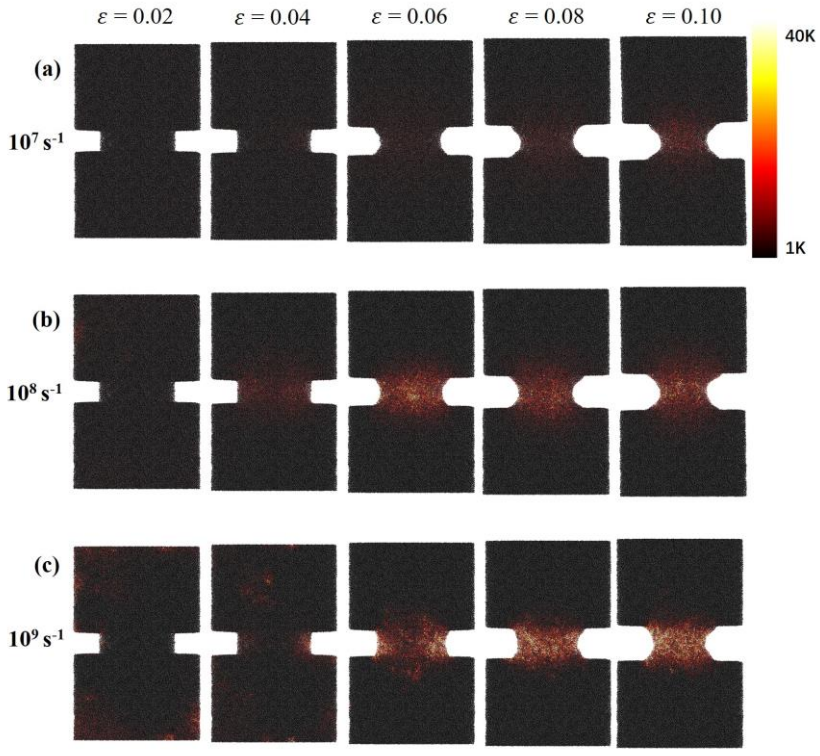

Figure 5.7 The local temperature rises in the notch center during tensile simulation of 4 nm notched samples under different strain rates. The calculation method is consistent with Figure 4.9.

5.4 Discussions

5.4.1 Mechanical properties

Figure 5.1 illustrates that with the increase of strain rate, the engineering yielding stress and strain increase accordingly. Such observations are consistent with the MD simulation performed by Cheng et al. [134] and can be well explained by using the cooperative shear model (CSM) [135, 136, 229]. The CSM of metallic glasses is based on the potential energy landscape described by Frenkel [230]. If we link the yield point to a critical activation rate of shear transformation zones, the strength of metallic glasses can be expressed as a function of temperature and strain rate. The equation of CSM can be written as:

$$\sigma_{CT} = \sigma_{C0} - \sigma_{C0}\left[\left(kT/W_{Tg}\right)\ln\left(\omega_0/C\gamma\right)\left(G_{0T}/G_{0Tg}\right)\right]^{2/3} \qquad (5.1)$$

where σ_{CT} is the yielding stress at Temperature T corresponding to the critical activation rate of shear transformation zones relative to the strain rate γ, σ_{C0} is the yield stress without thermal activation, which means (T = 0), W_{Tg} is the local megabasin barrier [231], ω_0 and C are constants. G_{0T} and G_{0Tg} are the zero-stress moduli at T and T_g, respectively.

Rearrangement of the above equation isolates and highlights the two key parameters: temperature and strain rate.

$$\sigma_{CT} = a_1\left\{1 - [a_2(a_3 - \ln\gamma)T]^{2/3}\right\} \quad (5.2)$$

where $a_1 = \sigma_{C0}$, $a_2 = \left(k/W_{Tg}\right)\left(G_{0T}/G_{0Tg}\right)$ and $a_3 = \ln(\omega_0/C)$. From the above equation, since the temperature in the simulations is constant, one can easily figure out that with the increase in strain rate, the yielding stress increases accordingly. Furthermore, by using nonlinear fitting method on MATLAB and setting the three parameters as $a_1 = 2.18$ GPa, $a_2 = 0.0074\,K^{-1}$ and $a_3 = 20.69$, all data in Figure 5.1 (a) can nicely fall on the predicted curves of CSM. The fitting results are shown in Figure 5.8. This means that the CSM can confidently explain our observations here. Also, as shown in Figure 5.8, other previous simulations on the yielding stress of $Cu_{64}Zr_{36}$ MGs (or a similar composition of $Cu_{65}Zr_{35}$) under different strain rate at low temperatures (below 50 K) are presented [36, 62, 134, 232-234]. It should be noted that there are many factors besides strain rate and temperature that can influence the yielding stress of simulated MGs, such as atom numbers, sample shapes, boundary conditions, the potential used in the simulation, cooling histories, and etc. which often result in dissimilarity among these works. However, despite of these differences, the trend is consistent that with the increase of strain rate, the yielding stress can increase correspondingly.

The fitted curve using CSM model on 4nm notched sample is also presented in Figure 5.9. The three parameters according to equation (5.2) are a_1 = 1.227

GPa, a_2 = 0.0118 K^{-1} and a_3 = 20.69, respectively. Compared to the fitted curve of unnotched samples, only a_1 (σ_{C0}, the yielding stress without thermal activations) exhibits obvious differences.

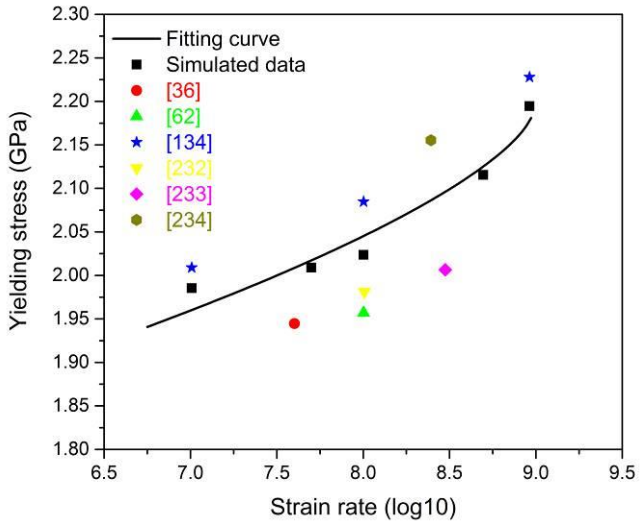

Figure 5.8 Strain rate dependence of the simulated yield stress of unnotched samples, as well as the fitted curves using CSM and results of previous simulations.

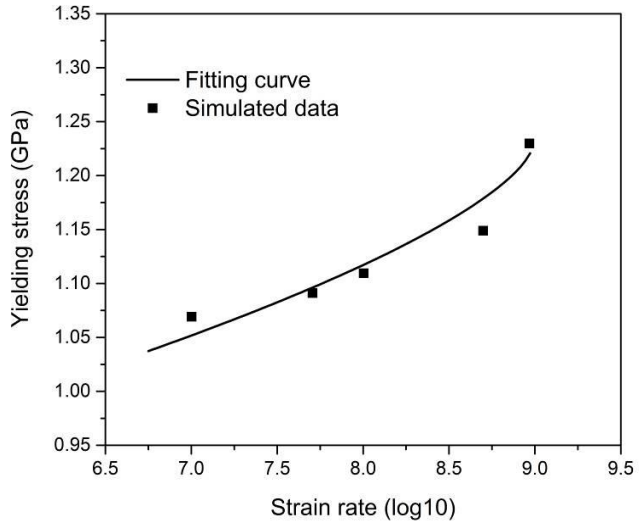

Figure 5.9 Strain rate dependence of the simulated yield stress of 4 nm notched samples, as well as the fitted curves using CSM

There are also two interesting phenomena that need to be discussed here. First, for samples under relatively slow strain rates, such as 10^7 s^{-1} and 5×10^7 s^{-1}, a serrated flow was observed during the plastic deformation period, which is in agreement with many experimental works [123, 124, 235, 236]. According to the studies made by Wright et al. [235] and Mukai et al. [123], a serrated flow on metallic glasses was observed under quasistatic loading conditions, but gradually diminishes with increasing strain rate. Although a strain rate of 10^7 s^{-1} cannot be counted as a quasistatic loading condition in terms of experimental conditions; however, it is still quite slow for MD simulations, which suggest a certain degree of consistency. This observation suggests that the atomic level structure inside the plastic deformed region is different between that in samples under low-strain-rate and high-strain-rate, resulting in two distinct mechanisms.

The second interesting phenomena is that in the stress-strain curves of samples under strain rate of 10^9 s^{-1}, there exist some fluctuations in the beginning of the deformation. This may be because that the initial structure of the undeformed sample cannot respond quickly enough at such a high strain rate, causing the fluctuations in the early period of the deformation. After that, the atomic structure has been adjusted in order to follow the rapid loading.

For the true stress strain curves presented in Figure 5.2, it is noticed that for the sample with high strain rates, there exists an increase in the yielding true strain.

Based on the present calculation method, this may be because that the cross sectional area in these samples under high strain rates reduce slower than that of samples with low strain rates. As the true strain here is defined as $(S - S(t))/S$, when the cross sectional area decreases at a slower rate, which will lead to a larger $S(t)$ and thus a smaller increase in true strain. The cross sectional area evolution in the notch part presented in Figure 5.10 further proves this suggestion. As showed in the figure, all samples exhibit a clear necking phenomenon. However, with the increase in strain rate, the reduction, or the necking of notch part gradually tends to be slower.

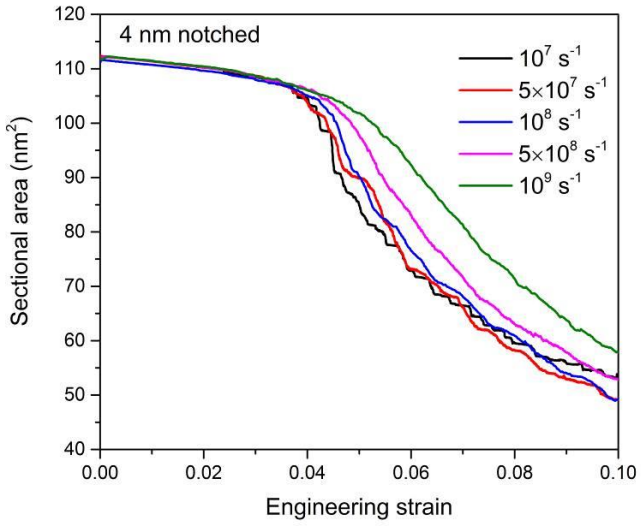

Figure 5.10 The change of cross sectional area of 4 nm notched sample during loading under different strain rates.

The shrinkage of cross sectional area in the notch part is a process of rearrangement of atoms. As the loading rate increases, atoms inside the notch

part cannot respond quickly enough at such high strain rates for the rearrangement to accomplish, which then leads to the cross sectional area to decreasing slower. This also suggests that the free volume generation inside the notch part of high-strain-rate samples may be more severe than that of the low-strain-rate samples.

5.4.2 Strain rate effect on deformation mode

Comparing Figure 5.3 (a) and (b), the shear band formed in the sample with lower strain rate is obviously wider than that formed in the sample with higher strain rate. This observation is closely related to the serrated flow in the stress strain curves of samples under low-strain-rate. As found by Li et al. [124], under a low strain rate, the atoms inside the shear band have more time to interact with each other and propagate throughout the sample, resulting in the shear band being fully developed, leading to a wider shear band. Combined with the stress-strain curve with the local shear strain distribution, the strain rate effect on the mechanical strength and deformation mode is clearly illustrated. Such a high-strain-rate strengthening effect has also been seen on some MD simulations of crystalline and multicrystalline metal nanowires [237-239]. Although they have different atomic structure compared to MGs, their ideas can still be borrowed to explain the strengthening phenomenon under higher strain rates. At high strain rates, a single shear localization event cannot keep up with the high strain

applied. Therefore, many plastic events are needed, which will lead to a more uniform spatial distribution of strain. While higher strain rate should lead to some subtle strengthening, the catastrophic shear banding can then be suppressed, and then will cause the strengthening phenomenon observed at strain rate = 10^9 s^{-1}.

For Figure 5.4, the 4 nm notched samples under different strain rates, the necking is relatively alleviated in high-strain-rate samples. By comparing the width of the notch part among these three samples, the final width at an engineering strain equal to 0.1 for the sample under a strain rate of 10^9 s^{-1} is obviously the largest. Referenced to the cross sectional area evolution in Figure 5.10, the results are self-explained. Also, as indicated in Chapter 4, the plastic deformation is alleviated in the notch center during the plastic deformation, compared to that of the notch tips. This finding is illustrated in the low-strain-rate samples (10^7 s^{-1} and 10^8 s^{-1}) as more blue colored region (meaning a low local shear strain) is shown in the notch center and more red colored region (a high local shear strain) in the notch tips. However, for the high-strain rate sample (10^9 s^{-1}), such a similar phenomenon disappears. The local shear strain distribution around the notch center and tips basically remains the same.

Based on Figure 5.4, the mean local shear strain evolution in the notch center for the three samples under different strain rates was further calculated, as

illustrated in Figure 5.11. It is clear that for samples under low strain rates, like 10^7 s^{-1} and 10^8 s^{-1}, obvious local strain reduction is observed during the plastic deformation process. However, for the sample under high-strain-rate of 10^9 s^{-1}, the local shear strain in the notch center continuously increases, resulting in a higher local shear strain at $\varepsilon = 0.1$. Combined with the results concluded in Chapter 4, these findings suggest that the Voronoi volume annihilation and full icosahedra recovery may not exist under the high-strain-rate condition. The Voronoi analysis later will further prove this suggestion.

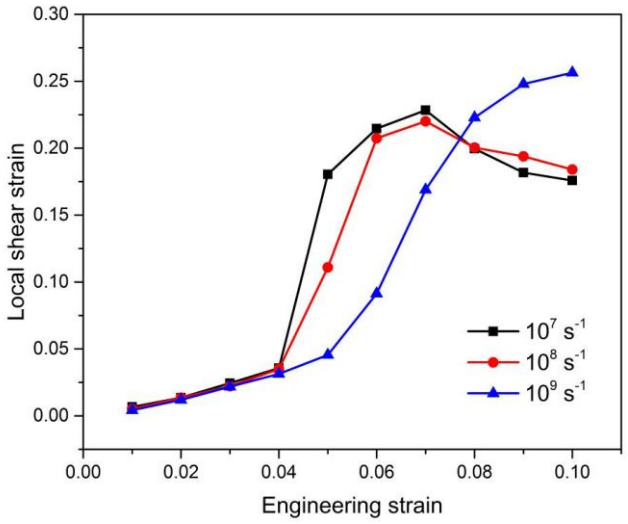

Figure 5.11 Mean local shear strain evolutions in the notch center during the deformation for samples under different strain rates, a 4 nm × 4 nm × 4 nm cubic region in the center of the notch is selected for calculation.

5.4.3 Strain rate effect on the Voronoi volume annihilation

Referred to Figure 5.5 (c) and (d), it is clear that the Voronoi volume annihilation

in samples with lower strain rate is more obvious than that in the samples with higher strain rate. This discovery, again, suggests that the findings of free volume annihilation may not be applied under high strain rates. As discussed in Chapter 4, the annihilation of Voronoi volume, or free volume is caused by diffusion, which needs enough time to take place. However, under high strain rates, the structural ordering process inside the notch part cannot react quickly enough to the rapid loading, and the diffusion rate is not high enough to offset the rapid generation caused by shear deformation. Thus, the annihilation of Voronoi volume may diminish or vanish.

The linear scan of mean Voronoi volume distribution of Cu-atoms along the Z-direction further proves this suggestion, as shown in Figure 5.12 of the 4 nm notched samples under different strain rates. In this figure, only Voronoi volume around Cu-atoms is presented; the situation for Zr-atoms is similar to Cu-atoms and not presented here. The dotted straight line shows the mean Cu-atoms Voronoi volume before loading starts. During the beginning of deformation (engineering strain equals to 0.02), the distribution line is basically the same among all three samples. In samples under low-strain-rates, palpable Voronoi volume annihilation can be seen in Figure 5.12 (a) and (b) during the plastic deformation. For strain rate equals to 10^7 s^{-1} and 10^8 s^{-1}, the highest mean Voronoi volume distribution line all appear at an engineering strain of 0.06, and then begin to decrease afterwards, with is consistent with Figure 5.5. While for

sample with a strain rate of 10^9 s^{-1}, during the plastic deformation, the Voronoi volume distribution around the notch center basically remains unchanged at engineering strain rate equals to 0.06, 0.08 and 0.1, which means that in these samples, the Voronoi volume annihilation is almost negligible. Combined with Figure 5.5, it is confident to draw the conclusion that high strain rate can hinder the annihilation of Voronoi volume, as the annihilation rate caused by diffusion cannot surpass its generation rate caused by rapid loading.

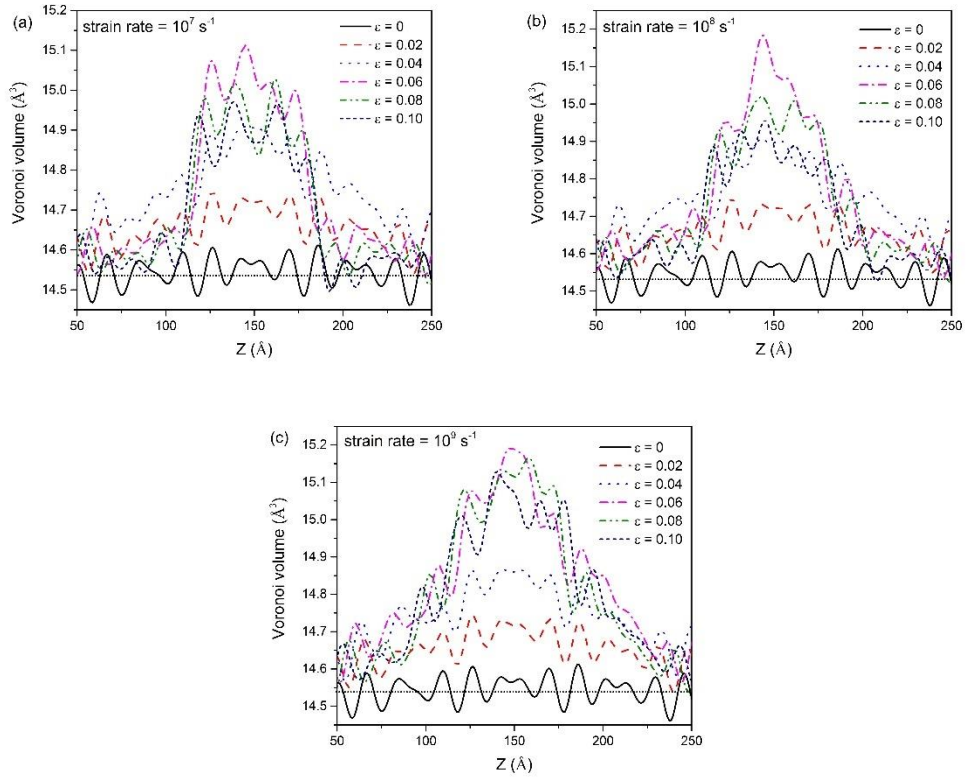

Figure 5.12 Distribution of mean Voronoi volumes of Cu-atoms along Z direction at different engineering strains for 4 nm notched sample under different strain rates. The calculation method is the same as that presented in Figure 4.15.

Combined with the results and discussion presented above, we can figure out the relationship between strain rate, yielding stress and average Cu-Voronoi volume in the center of the notch region at engineering strain = 0.1, as shown in Figure 5.13. The increase of yielding stress with increasing the strain rate can be fairly explained by the CSM theory; and the rapid loading causes Voronoi volume generation overtaking its annihilation, which lead to the increase of average Cu-Voronoi volume at engineering strain = 0.1. The relationship observed here is clear and consistent, revealing the influence of strain rate on the deformation mechanism of CuZr MG under multiaxial stress state.

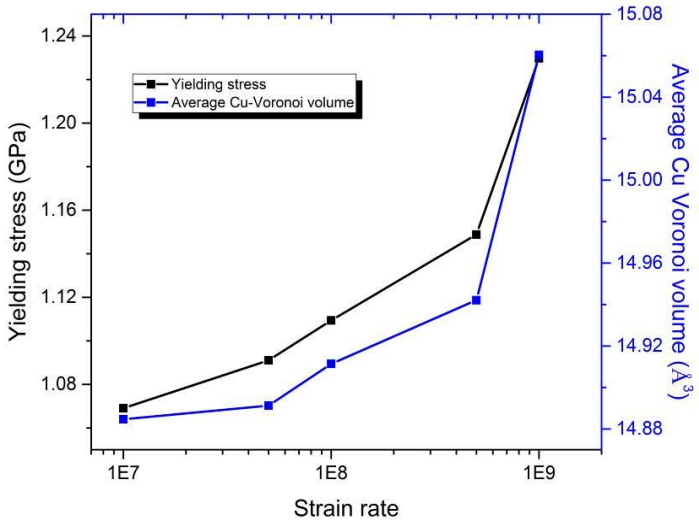

Figure 5.13 Effect of strain rate on the yielding stress and average Cu-Voronoi volume in the center of the notch at engineering strain = 0.1

5.4.4 Strain rate effect on the short-range-order evolution

Figure 5.6 demonstrates that the Cu-centered FI fraction recovery phenomenon

is not observed in samples with high strain rates. As discussed in Chapter 4, the annihilation of Voronoi volume and the recovery of Cu-centered FI fraction is a cooperated process during the plastic deformation under multiaxial stress state with relatively slow strain rate. It is now obvious that under high strain rate, both these two phenomena can vanish as the rapid loading causes the rate of Voronoi generation to be higher than that of its annihilation and the full-icosahedra backbone can be severely disrupted with no recovery monitored.

Such a phenomenon can also be explained in the view of local temperature rise. Figure 5.14 shows the local temperature evolution in the notch center. We can see that for samples with relatively low-strain-rates, as plastic deformation starts, a clear decrease in local temperature is found in the notch center; while for samples with high strain rates, the local temperature continuously increases. As mentioned in Chapter 4, the local temperature reduction in the notch center under low-strain-rate is a result of atomic rearrangement and structure ordering process. This demonstrates that the high strain rate can lead to a huge increase in atomic kinetic energy while ordering process can hardly take place. Combined with the Voronoi volume evolution and the fraction of full-icosahedra changes, it is safe to draw the conclusion that the strain rate can greatly influence the deformation mechanism of the MGs.

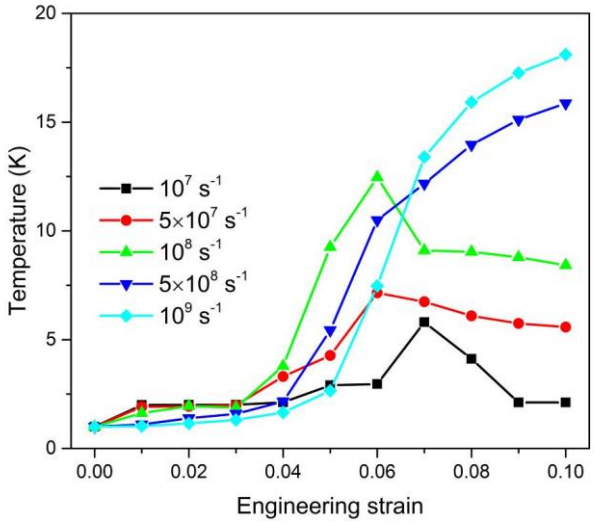

Figure 5.14 Local temperature evolution in the notch center during deformation of 4 nm notched samples. The region selected is consistent with that in Figure 5.6.

5.5 Conclusion

In this chapter, MD simulations have been performed under various strain rates and the strain rate effect on the deformation behavior of both unnotched and notched samples with different geometry have been investigated. Results show that an increase in yielding stress is observed with the increasing strain rate on both notched and unnotched samples, which can be well explained by the CSM theory. For the unnotched sample, a high strain rate can cause the deformation mode transits from shear banding to a more uniform strain distribution, and there is also a more severe Voronoi volume generation inside the plastic deformed region. While for deep-notched samples, the high-strain-rate can lead to an alleviated reduction of cross sectional area. More importantly, the

annihilation of Voronoi volume, recovery of Cu-centered FI and decrease in local temperature during the plastic deformation can vanish inside the notch center. The rapid loading can cause the generation of free volume higher than its annihilation assisted by notch geometry. The deformation mechanism of CuZr metallic glasses under high-strain-rate and low-strain-rate is quite different, which enriches the understanding of the structure-properties relationship of the MGs.

Chapter 6 Effect of temperature on the deformation behavior of CuZr metallic glasses

6.1 Introduction

In the previous chapters, the effect of notch geometry and strain rate on the deformation mechanism of metallic glasses have been presented. The results testified that both notch geometry and strain rate can have great impact on the tensile strength, evolution of Voronoi volume, local short-range-order structure and local temperature. Meanwhile, other factors that can influence the atomic level mechanisms must be taken into consideration. Temperature is a crucial factor that can influence the deformation behavior of metallic glasses because it can affect both the generation and annihilation rate of free volume during the deformation [75, 81, 85, 88]. Therefore, it is necessary to study the effect of temperature on the atomic level structural evolution, which could help us to better understand the intrinsic mechanical nature of CuZr metallic glasses.

In this chapter, different temperature will be applied on samples both without notch and with different notch depths during the tensile simulation. In order to analyze the structural changes during plastic deformation, the Voronoi method will be used to investigate the Voronoi volume and Cu-centered FI evolution. Cooperative shear model will be adopted to explain the temperature sensitivity

on the mechanical properties of CuZr metallic glasses.

6.2 Simulation details

Small $Cu_{64}Zr_{36}$ samples containing 13,500 atoms are simulated with cooling rate of 5×10^{10} K/s and quenched from 2000 K to 300 K, 200 K, 100 K or 1 K. The large cylinder-shape samples containing ~ 600,000 atoms for the mechanical simulation are constructed by replications of the small configurations and then annealed for 200 ps. Notches are created by eliminating atoms in the center of the sample. The final cylinder samples have a diameter of 20 nm in X- and Y- directions and length of 30 nm in the Z- direction, with a notch depth of either 2 nm and 4 nm. The notch width is 3 nm for each sample. PBCs are applied in the Z-direction while free surface is used in the X- and Y-directions to allow shear band to take place. Uniaxial loading is employed in Z-direction with a constant strain rate of 10^8 s^{-1}, which is relatively slow for MD simulations. The stress is calculated from the normal tensor component of virial stress along the loading Z-direction. Atomic configurations analysis is performed by using Voronoi Tessellation method for full-icosahedra statistics and Voronoi volume calculation. For each geometry, simulations are carried out three times and different initial configurations are used each time to ensure the data accuracy. A summary of simulated samples is listed in Table 6.1.

Table 6.1 Summary of simulation setups in Chapter 6

	1 K	100 K	200 K	300 K
Unnotched	TU_1K	TU_100K	TU_200K	TU_300K
2nm notched	T2_1K	T2_100K	T2_200K	T2_300K
4nm notched	T4_1K	T4_100K	T4_200K	T4_300K

6.3 Results

6.3.1 Stress-strain curves

Figure 6.1 shows the engineering stress-strain curves of the unnotched and notched samples with different notch depths under various loading temperatures. It is clear that under the same temperature, the yielding stress decreases with increasing notch depth, which is consistent with the phenomena seen in Chapter 4 and 5. For samples with same notch configuration, the yielding stress decreases accordingly with the increase of loading temperature. For example, the yielding stress of the unnotched sample under 1 K is about 2 GPa at engineering stain equals to 0.05 and then decreases with the increase of temperature. The yielding stress is only about 1.5 GPa under 300 K. For 2 nm notched and 4 nm notched samples, similar phenomenon is observed.

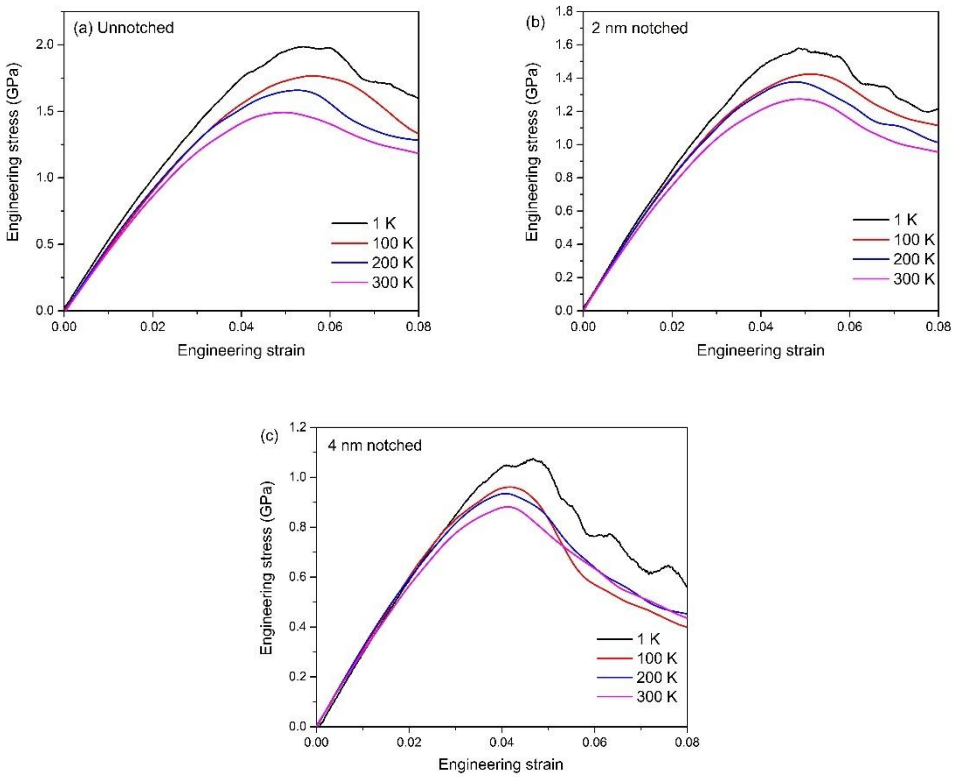

Figure 6.1 The engineering stress-strain curves of the unnotched, 2 nm notched and 4 nm notched samples under different temperatures, respectively.

The true stress-strain curves of the 4 nm notched samples were also performed, as illustrated in Figure 6.2. The calculation is similar to which has been presented in Chapter 4. As we can see, with the increase in temperature, the true yielding stress decreases accordingly. For the sample under 1 K, the true yielding stress is about 3.25 GPa; while for the sample under 300 K, the true yielding stress decreases to only 2.6 GPa. Moreover, a decrease in modulus is also observed. This suggests that the sample tends to show a softening phenomenon with increasing temperature. The present results are in agreement with the experimental results performed by Lee et al. [139] and Lu et al. [15].

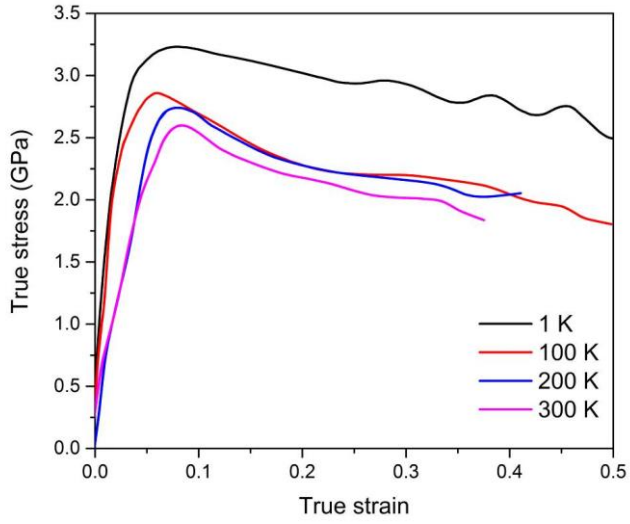

Figure 6.2 The true stress-strain curves of 4 nm notched samples under different loading temperatures.

Figure 6.3 shows the cross sectional area changes of 4 nm notched sample during deformation. In the beginning of the deformation, the cross sectional areas of samples under various temperature exhibit subtle differences; those under high temperatures show a large initial cross sectional area which is simply because of the volume differences caused by different annealing temperatures. With the increase in the temperature, the absolute decrease of cross sectional area, or the necking of the notch part gradually tends to be smaller. Along with the loading, the necking phenomenon under low temperature is more dramatic.

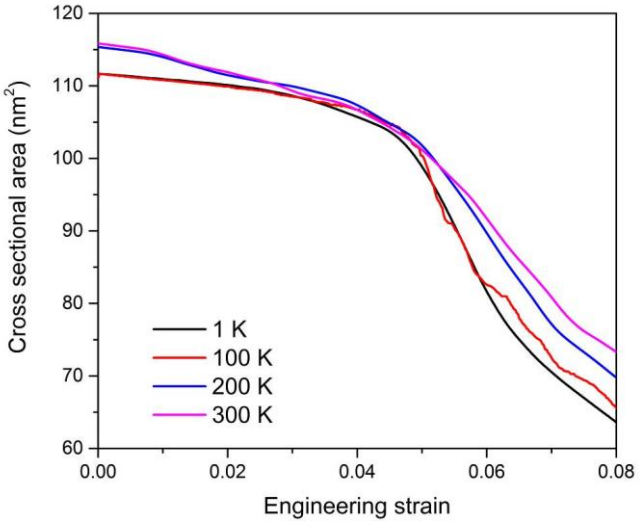

Figure 6.3 The change of cross sectional area of 4 nm notched samples under different loading temperatures.

6.3.2 Local strain distributions

Figure 6.4 and Figure 6.5 show the local atomic strain distributions of unnotched and 4 nm notched samples under different loading temperatures during the tensile simulation, respectively. From Figure 6.4, we can see that for samples at lower temperature (1 K and 100 K), the deformation mode is shear banding with a single shear band approximately 45° relative to the loading direction. While for samples at higher temperatures (200 K and 300 K), the deformation mode tends to be a near-necking mechanism. The plastic deformed region is nearly perpendicular to the Z- direction.

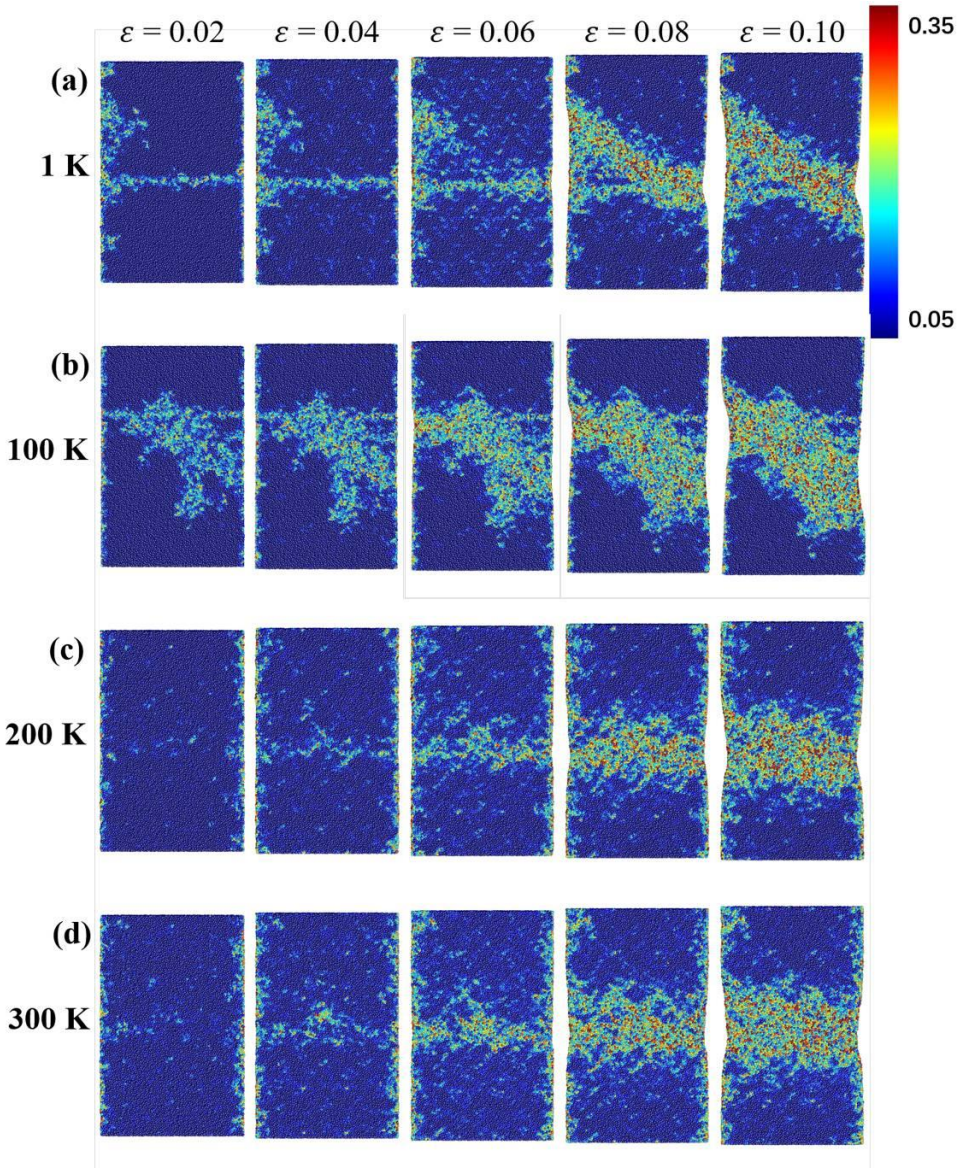

Figure 6.4 Projected views of the atom configurations at different engineering strain of the unnotched samples under four different loading temperatures: 1 K (a), 100 K (b), 200 K (c) and 300 K (d). The color indicates the local von Mises strain.

In Figure 6.5, all the 4 nm notched samples show a necking mechanism although the loading temperature is different. However, it is clear that with the increase in loading temperature, the initiation of necking tends to be delayed. For example, at an engineering strain equal to 0.06, under 1 K, the severe deformed

region has already penetrated through the notched part; while under 300 K, only the notch tip shows severe deformation.

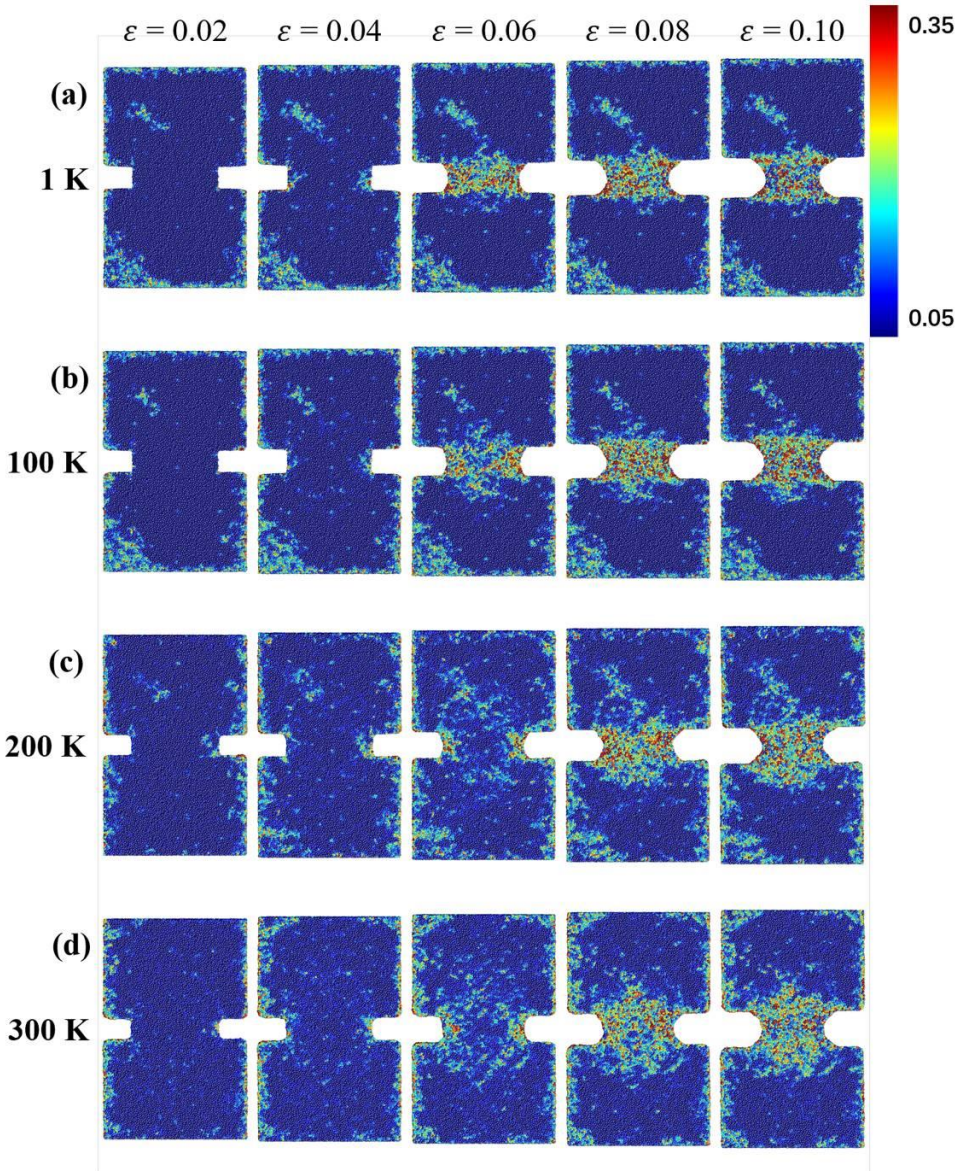

Figure 6.5 Projected views of the atom configurations at different engineering strain of the 4 nm notched samples under four different loading temperatures: 1 K (a), 100 K (b), 200 K (c) and 300 K (d). The color indicates the local von Mises strain.

6.3.3 Voronoi volume evolution

Figure 6.6 shows the mean Voronoi volume evolution of Cu- and Zr-atoms in

the unnotched and 4 nm notched samples under different loading temperatures. The method for calculation is the same as that presented in Figure 4.7. As for Figure 6.6 (a) and (b), in the unnotched samples, the initial Voronoi volumes of the Cu and Zr atoms present a subtle difference. This is because these samples have different initial Voronoi volume under different temperatures. Samples at high temperatures have a larger initial Voronoi volume. Along with the deformation, both the mean Voronoi volume of Cu atoms and Zr atoms increase, which is consistent with the observations presented in Chapter 4. This means that they all show a clear strain softening phenomenon as proved by the significant Voronoi volume generation inside the shear band.

For 4 nm notched samples, Figure 6.6 (c) and (d), under different temperature, they all exhibit an increase in the Voronoi volume around Cu-atoms and Zr-atoms in the beginning of the loading. After that they reach their peak values and then start to decrease. The peak point is consistent with the local shear strain distribution map shown in Figure 6.5. Moreover, the Voronoi volume around Cu-atoms tends to decrease more dramatically than that around Zr-atoms, which is consistent with the phenomenon monitored in Chapter 4. For samples under lower temperatures such as 1 K and 100 K, the evolution of Voronoi volume is similar to that presented in Chapter 4. However, for samples under higher temperature, the decreases in Voronoi volumes tend to be less obvious, showing that high temperature can hinder the annihilation of Voronoi volume.

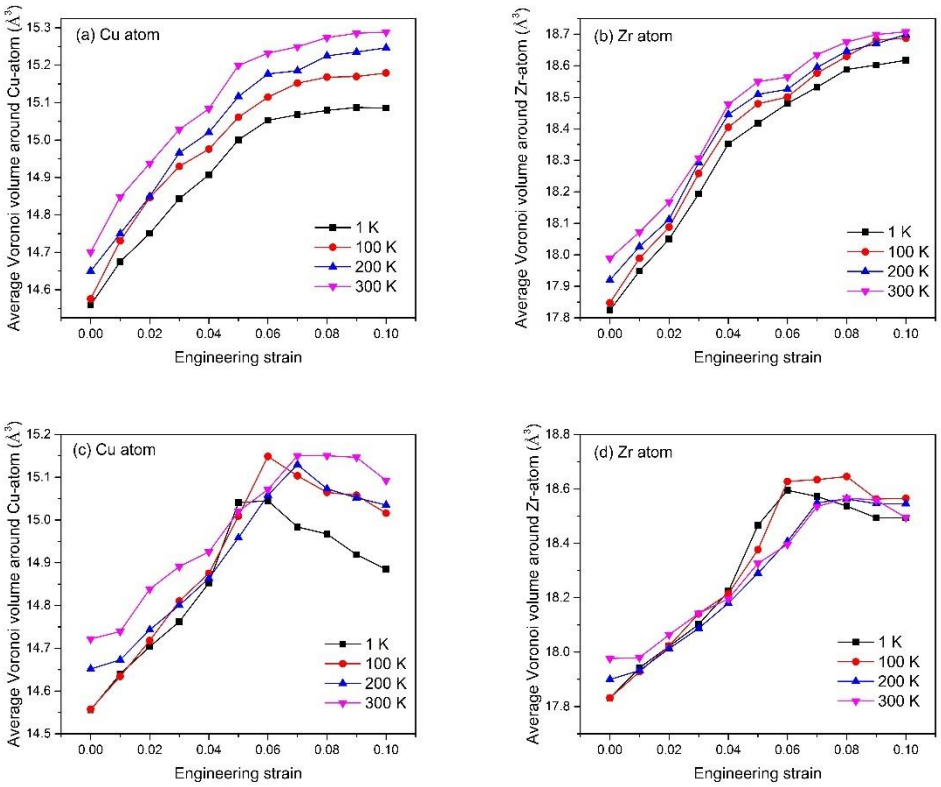

Figure 6.6 Average Voronoi volume around Cu- and Zr-atoms during tensile simulation of unnotched (a), (b) and 4 nm notched samples (c), (d) under different temperatures. The calculation method is the same as that presented in Figure 4.7.

6.3.4 Voronoi tessellation analysis

Figure 6.7 presents the evolution of Cu-centered FI fraction during the tensile simulation for 4 nm notched sample under different temperatures. The region selected is in the center of the notch, the same as presented in Figure 4.7. For samples with relatively low temperatures, a clear recovery of the Cu-centered FI fraction is illustrated in the plastic deformation period. For example, under a loading temperature of 1 K, after the severe drop during elastic deformation

period, the Cu-centered FI fraction starts to recovery at an engineering strain equal to 0.07. However, for sample under higher temperatures (200 K and 300 K), such a recovery is less obvious.

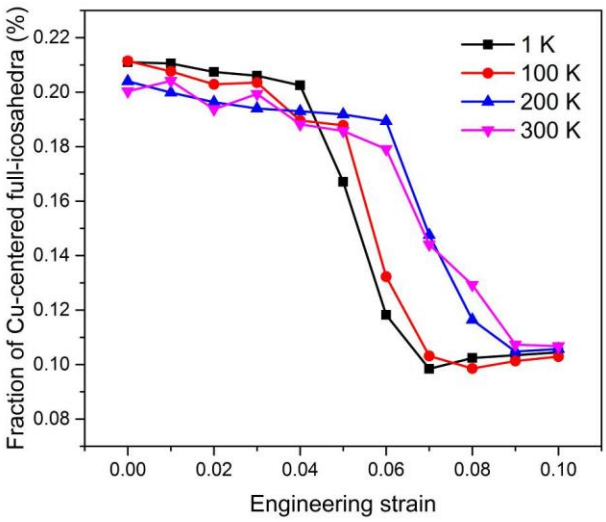

Figure 6.7 The Cu-centered full-icosahedra fraction in the center of 4 nm notched samples during the deformation under different loading temperatures. The region selected is the same as that in Figure 6.6.

6.4 Discussions

6.4.1 Effect of temperature on the mechanical properties

Figure 6.1 demonstrates the decrease of tensile yielding stress with increasing the temperature. This observation is consistent with the work performed by Cheng et al. [134]. As mentioned in Chapter 5, the dependence of yielding stress on the temperature and strain rate can be described as the following equation:

$$\sigma_{CT} = a_1\left\{1 - [a_2(a_3 - \ln\gamma)T]^{2/3}\right\} \quad (6.1)$$

where $a_1 = \sigma_{C0}$, $a_2 = \left(k/W_{Tg}\right)\left(G_{0T}/G_{0Tg}\right)$ and $a_3 = \text{in}(\omega_0/C)$.

Since the strain rate in this simulation is set to be consistent (10^8 s^{-1}), one can easily figure that the yielding stress decreases with increasing the temperature. Figure 6.8 shows the simulated yielding stress of unnotched and 4 nm notched samples as well as the fitted curve using CSM theory. For unnotched samples, the three parameters are a_1 = 2.011 GPa, a_2 = 7.602×10^{-5} K/s, a_3 = 23.7061, respectively. For 4 nm notched samples, the three parameters are a_1 = 1.069 GPa, a_2 = 5.8261×10^{-5} K/s, a_3 = 22.473, respectively. Only a_1 exhibits considerable differences due to the notch geometry.

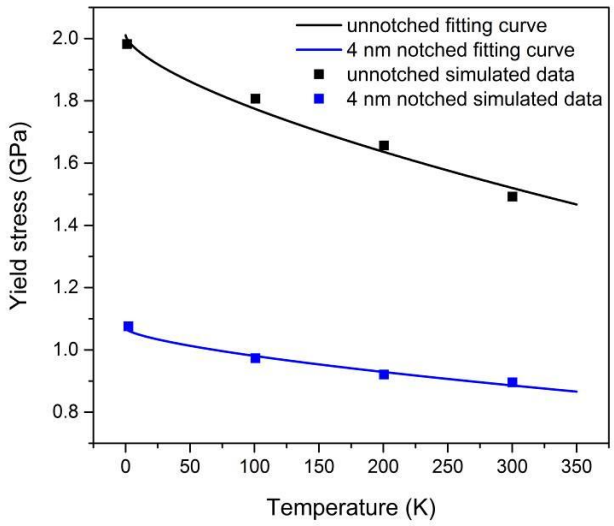

Figure 6.8 Temperature dependence of the simulated yielding stress in unnotched samples and 4 nm notched samples, as well as the fitted curve using CSM.

Combined with the results presented in Chapter 5, it is clear that CSM theory [135] can efficiently explain the effect of strain rate and temperature on the mechanical properties of CuZr metallic glass. In fact, Johnson and Samwer [135] have applied on series of Zr-based, Pd-based and other MGs, and found a well agreement with the experimental data.

6.4.2 Temperature effect on deformation mode

From Figure 6.5, it is clear that the local shear strain distribution can be different among samples under different loading temperatures. To further investigate the loading temperature effect on samples under multiaxial stress states, the center of the notch region should be focused. As illustrated in Figure 6.9, the local shear strain in the notch center of 4 nm notched samples under different temperatures is further calculated. For samples under 1 K and 100 K, a significant local strain reduction is observed during the plastic deformation, similar to the phenomenon observed in Figure 4.12. While for samples under 200 K and 300 K, the local shear strain continuously increases, resulting in a much more seriously deformed region. As we have discussed in Chapter 5, the severe deformed region is a reflection of the disordering atomic structure inside the sample. Here it is demonstrated that at the same engineering strain, the local shear strain in the notch center of samples under relatively high temperature can be higher than that in the samples under low temperature. Thus, such a higher

local shear strain may suggest a more disordered structure in the notch center for samples under high loading temperature.

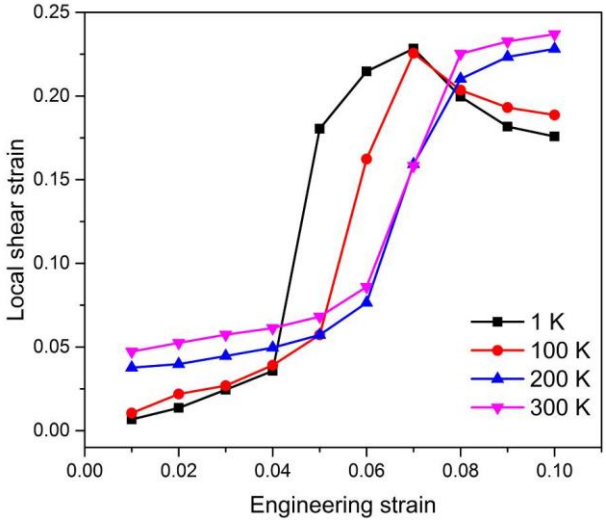

Figure 6.9 Mean local shear strain evolutions in the notch center during the deformation for samples under different temperatures. The calculation method is same as that presented in Figure 4.12.

6.4.3 Effect of temperature on the Cu-centered Voronoi volume evolution and SRO structure

Figure 6.6 presents that the annihilation of Cu-centered Voronoi volume in the center of the notched samples can be hindered under high temperatures. To further demonstrate this trend, the linear scan of average Voronoi volume distributions along Z-direction in 4 nm notched samples under different temperatures are illustrated in Figure 6.10. Only Cu-atoms Voronoi volume is presented here. It can be seen that for samples under lower temperatures, the Voronoi volume annihilation during the plastic deformation period is much

more obvious. For example, under 1 K, a comparison of the Voronoi volume distribution lines at engineering strain equals to 0.06 and 0.1 clearly shows the annihilation in Cu-centered Voronoi volume during plastic deformation. However, for the samples under 300 K, the decrease of Cu-centered Voronoi volume between engineering strains equal to 0.06 and 0.1 can be almost negligible. Therefore, the temperature influences on the Voronoi volume evolution is demonstrated. This suggests that with the increasing temperature, the Voronoi volume generation rate in the notch center is higher than the annihilation rate, which results in a structural disordering process, rather than the structural ordering process observed in Chapter 4.

As for the SRO structure, Figure 6.7 already demonstrated that under high temperatures, no recovery of Cu-centered FI fraction recovery is observed. This could be explained by that the high temperature could lead to a higher local shear strain in the center of the notch. Therefore, the structure ordering process observed in Chapter 4 could be hindered, which reflected as a continuous decrease in Cu-centered FI fraction.

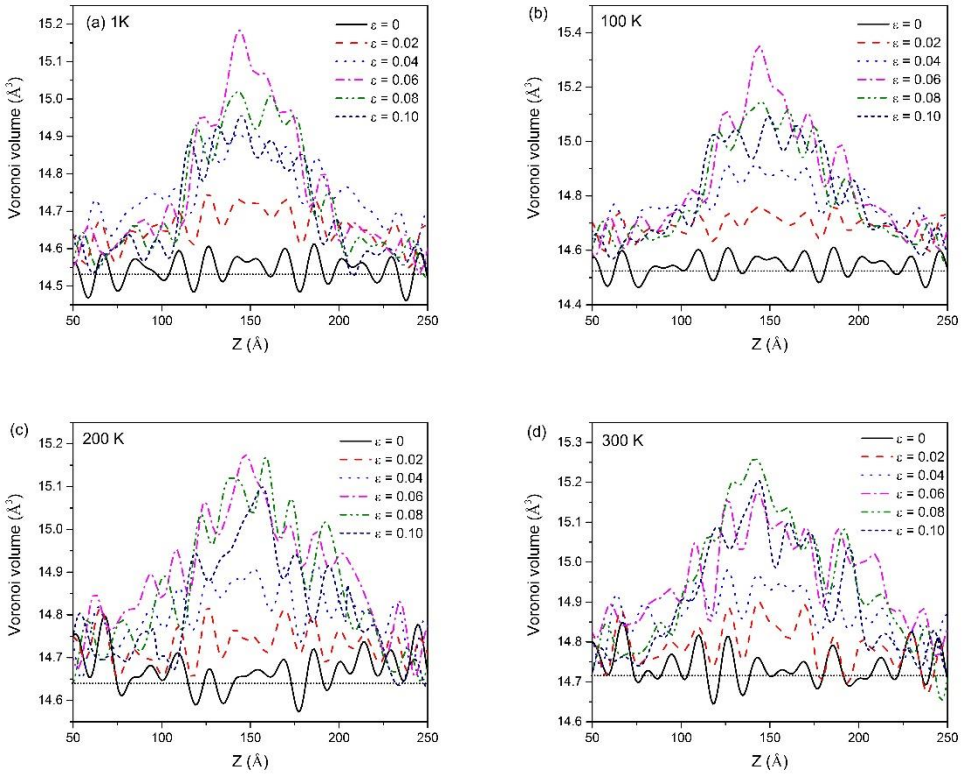

Figure 6.10 Distribution of mean Voronoi volumes along Z-direction at different engineering strains for 4 nm notched samples under different temperatures.

Combined with the results and discussions above, the relationship between loading temperature, yielding stress and average Cu-Voronoi volume in the center of the notch at engineering strain = 0.1 is shown in Figure 6.11. The decrease of yielding stress with increasing the temperature is caused by thermal softening, which can be explained by CSM theory. For the average Cu-Voronoi volume in the center of the notch at engineering strain = 0.1, the high loading temperature can cause a larger initial Voronoi volume, as well as a reduced Voronoi volume phenomenon.

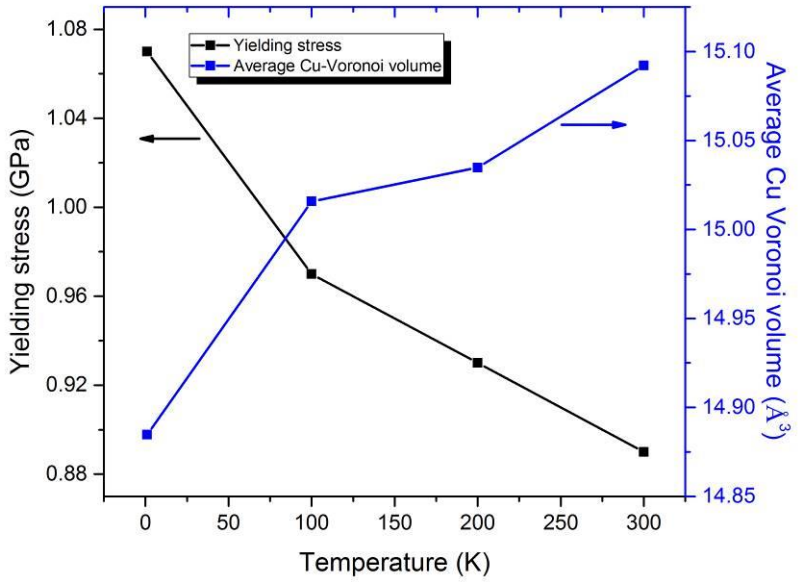

Figure 6.11 Effect of loading temperature on the yielding stress and average Cu-Voronoi volume in the center of the notch at engineering strain = 0.1.

6.5 Conclusions

In this chapter, MD simulations were performed under various temperatures and the effect of temperature on the deformation behavior in both unnotched and notched samples has been investigated. The results demonstrate there is a decrease in engineering yielding stress when the temperature increases, which can be well explained by CSM theory. For all the samples, an increase of temperature can cause a decrease in modulus and a softening phenomenon. For deep notched samples, an alleviated cross sectional area reduction is observed at higher temperatures and structural analysis showed that the structure ordering process observed in Chapter 4 at low temperatures and low strain rates diminished. Under higher temperatures, the annihilation of Voronoi volume and

the recovery of Cu-centered FI fraction can vanish. The deformation mechanism of CuZr metallic glasses can be quite different under different temperatures and the rate of free volume generation can be more rapid than its annihilation at high temperatures.

Chapter 7 Conclusions and future work

7.1 Conclusions

The primary objective of this thesis is to investigate the mechanical behaviors of CuZr metallic glasses under different situations based on molecular dynamics simulation and relate them to the atomic-level structural evolution. Using the Voronoi tessellation method for structural analysis, the effects of notch geometry, strain rate and temperature on the deformation mechanism of $Cu_{64}Zr_{36}$ metallic glasses under net tensile loading has been studied.

In Chapter 3, the melt-quenching process of $Cu_{64}Zr_{36}$ glass with different cooling rates was successfully simulated. The effect of cooling rates on the atomic−level structure of the metallic glass has been investigated and the results testified that a fully amorphous structure has formed. The atomic density, mass density and mean nearest neighbor distance extracted from PDF patterns are found to have good agreement with experimental data. It is also demonstrated that samples with the slower quenching rates have a larger Cu-centered FI fraction and a more ordered short-range structure compared to those formed at a faster quenching rates. For these reasons, the $Cu_{64}Zr_{36}$ metallic glass with a cooling rate of 5×10^{10} K/s simulated in this chapter was used to build up larger samples in the following tensile simulations.

In Chapter 4, a Voronoi volume annihilation phenomenon is revealed by introducing notched geometry into the cylinder $Cu_{64}Zr_{36}$ metallic glass samples. Compared to the unnotched sample whose deformation is dominated by shear banding and structure softening, the deep-notched samples exhibit a necking mechanism. Contrary to the obvious Voronoi volume generation inside the shear band, a clear Voronoi volume annihilation is observed in the center of notched region during the plastic deformation, together with a Cu-centered FI fraction recovery and a decrease in local temperature. It has been demonstrated that in the center of the deep notched sample, the rate of free volume annihilation can surpass the rate of its generation, causing a structural hardening phenomenon. The links between multiaxial stress states, structural evolution and mechanical behavior is revealed.

In Chapter 5, the deformation behaviors of unnotched and notched samples with different notch depth under various strain rates have been studied. The results reveal an increase in yielding stress with increasing strain rate. CSM theory was successfully applied to explain such phenomena and non-linear fitted curves showed good agreement with simulated results. High-strain-rate can cause the deformation mechanism to transit from shear banding to a more uniform deformation for the unnotched samples. A more dramatic generation of Voronoi volume is monitored inside the plastic deformed regions. For deep notched samples, the necking of the notched part seems to be alleviated under high-

strain-rate due to atoms inside the notched part not being able to respond quickly enough for atomic rearrangement to be accomplished. Also, the local shear strain in the center of the notch keeps increasing during the deformation under high-strain-rates, instead of the reduction seen under low-strain rates. More importantly, the annihilation of Voronoi volume, recovery of Cu-centered FI and decrease of local temperature during the plastic deformation can vanish inside the notch center. The rapid loading can cause the generation rate of free volume to be higher than its annihilation assisted by notched geometry. It was demonstrated that the Voronoi volume annihilation can only be observed under low-strain-rate condition and may not be applied under high-strain-rate tensile loading.

In Chapter 6, the deformation mechanism of samples with and without notch under various loading temperatures has been investigated. CSM theory has been found to well explain the decrease in engineering yielding stress when the temperature increases. Also, a softening phenomenon of decrease in modulus has been observed when the loading temperature increases. An alleviated cross sectional area reduction on deep-notched samples was testified. Likewise, the structural ordering process under low temperature and low strain rate can diminish or vanish under high loading temperature. It was demonstrated that the generation of free volume is faster than its annihilation under higher temperature.

The major contribution of this work is the demonstration of Voronoi volume annihilation phenomenon on the deep notched samples when strain rate and temperature are both low. By using MD simulation, previous experimental findings [97] are supported in a view of atomic-level mechanisms. This work can enrich the understanding of the structure-property relationship of metallic glasses.

7.2 Recommendations for future work

To fully understand the deformation mechanism of CuZr metallic glasses, it is not enough to merely pay attention to the SRO structure. Moreover, the MRO structure during the deformation process must be taken into consideration. Many previous simulations have paid their attentions on the MRO of the CuZr metallic glasses [25, 33, 37, 191] and pointed out that during the deformation, the breakdown of the Cu-centered FI backbone is the key factor that influences the mechanical behavior of CuZr MGs. However, no one has ever studied the MRO structural evolution under notched geometry and multiaxial stress state. In the future work, it would be useful to investigate the MRO structural evolution during the plastic deformation, and find out the role of Cu-centered FI backbone under multiaxial stress state. Moreover, the effects of strain rate and temperature on the Cu-centered FI backbone transition need to be studied.

Furthermore, the effect of strain rate and temperature in this study were covered

over a wide range. In future works, the mechanical behavior of CuZr metallic glass under more various strain rates and temperatures should be investigated in order to build up a strain rate-temperature map and find out the critical condition for the Voronoi volume annihilation phenomenon to vanish. Moreover, it will be necessary conduct experimental works and theoretical calculations in order to support the simulation results.

List of Publication

Wang Cui, Jie Pan, Daniel John Blackwood, Yi Li, Voronoi volume annihilation during plastic deformation in deep-notched metallic glasses, Acta Materialia (2016), submitted

Yuxing Tian, Zhentao Yu, Chun Yee Aaron Ong, Wang Cui, Nonlinear elastic behavior induced by nano-scale α phase in β matrix of β-type Ti–25Nb–3Zr–2Sn–3Mo titanium alloy, Materials Letters 145 (2015) 283-286.

Shengjin Wang, Dechang Jia, Wang Cui, Zhihua Yang, Xiaoming Duan, Yingfeng Shao, Yu Zhou, Effect of starting PMMA content on microstructure and properties of gel casting BN/Si_3N_4 ceramics with spherical-shaped pore structures, Journal of Material Science, 48 (2013) 7974-7980.

Shengjin Wang, Zhihua Yang, Xiaoming Duan, Dechang Jia, Wang Cui, Boqian Sun, Yu Zhou, Effects of pore size on microstructure, mechanical and dielectric properties of gel casting BN/Si_3N_4 ceramics with spherical-shaped pore structures, Journal of Alloys and Compounds, 581 (2013) 46-51.

References

[1] F. Luborsky. Amorphous metallic alloys, Butterworth and Co (Publishers): London, UK, 1983.

[2] J. Schroers. Processing of bulk metallic glass, Advanced Materials 22 (2010) 1566-1597.

[3] J.R. Scully, A. Gebert, J.H. Payer. Corrosion and related mechanical properties of bulk metallic glasses, Journal of Materials Research 22 (2007) 302-313.

[4] M. Chen. Mechanical behavior of metallic glasses: microscopic understanding of strength and ductility, Annual Review of Materials Research 38 (2008) 445-469.

[5] W.L. Johnson. Bulk glass-forming metallic alloys: Science and technology, MRS Bulletin 24 (1999) 42-56.

[6] P. Chaudhari, D. Turnbull. Structure and properties of metallic glasses, Science 199 (1978) 11-21.

[7] P. Duwez, R. Willens, W. Klement Jr. Metastable electron compound in Ag-Ge alloys, Journal of Applied Physics 31 (1960) 1137-1137.

[8] A. Inoue, T. Zhang, T. Masumoto. Zr–Al–Ni amorphous alloys with high glass transition temperature and significant supercooled liquid region, Materials Transactions, JIM 31 (1990) 177-183.

[9] A. Peker, W.L. Johnson. A highly processable metallic glass: Zr41. 2Ti13. 8Cu12. 5Ni10. 0Be22. 5, Applied Physics Letters 63 (1993) 2342-2344.

[10]Z. Sha, Y. Feng, Y. Li. The fundamental structural factor in determining the glass-forming ability and mechanical behavior in the Cu–Zr metallic glasses, Materials Chemistry and Physics 127 (2011) 292-295.

[11]Z. Sha, Y. Feng, Y. Li. Statistical composition-structure-property correlation and glass-forming ability based on the full icosahedra in Cu-Zr metallic glasses, Applied Physics Letters 96 (2010) 1903.

[12]Q.-K. Li, M. Li. Atomistic simulations of correlations between volumetric

change and shear softening in amorphous metals, Physical Review B 75 (2007) 094101.

[13]A. Greer, Y. Cheng, E. Ma. Shear bands in metallic glasses, Materials Science and Engineering: R: Reports 74 (2013) 71-132.

[14]Q.K. Li, M. Li. Free volume evolution in metallic glasses subjected to mechanical deformation, Materials Transactions 48 (2007) 1816-1821.

[15]J. Lu, G. Ravichandran, W.L. Johnson. Deformation behavior of the Zr 41.2 Ti 13.8 Cu 12.5 Ni 10 Be 22.5 bulk metallic glass over a wide range of strain-rates and temperatures, Acta Materialia 51 (2003) 3429-3443.

[16]J.R. Telle, N.A. Pearlstine. Amorphous materials: research, technology and applications, Nova Science Publishers, 2009.

[17]W. Klement, R. Willens, P. Duwez. Non-crystalline structure in solidified gold–silicon alloys, Nature 187 (1960) 869-870.

[18]H. Chen, C. Miller. Centrifugal spinning of metallic glass filaments, Materials Research Bulletin 11 (1976) 49-54.

[19]A. Drehman, A. Greer, D. Turnbull. Bulk formation of a metallic glass: Pd40Ni40P20, Applied Physics Letters 41 (1982) 716-717.

[20]H. Chen. Thermodynamic considerations on the formation and stability of metallic glasses, Acta Metallurgica 22 (1974) 1505-1511.

[21]H. Chen. Glassy metals, Reports on Progress in Physics 43 (1980) 353.

[22]H. Kui, A.L. Greer, D. Turnbull. Formation of bulk metallic glass by fluxing, Applied Physics Letters 45 (1984) 615-616.

[23]A. Inoue, T. Zhang, J. Saida, M. Matsushita, M.W. Chen, T. Sakurai. Formation of icosahedral quasicrystalline phase in Zr–Al–Ni–Cu–M (M= Ag, Pd, Au or Pt) systems, Materials Transactions, JIM 40 (1999) 1181-1184.

[24]T. Zhang, A. Inoue, T. Masumoto. Amorphous Zr–Al–TM (TM= Co, Ni, Cu) alloys with significant supercooled liquid region of over 100 K, Materials Transactions, JIM 32 (1991) 1005-1010.

[25]Y. Cheng, E. Ma. Atomic-level structure and structure–property

relationship in metallic glasses, Progress in Materials Science 56 (2011) 379-473.

[26]R. O'Handley. Magnetostriction of ferromagnetic metallic glasses, Solid State Communications 21 (1977) 1119-1122.

[27]B.W. Kennedy. Energy efficient transformers, McGraw-Hill Professional Publishing, 1998.

[28]J. Li. Use of energy efficient transformers in Asia. Asian Energy Conference, 2000.

[29]W.-H. Wang, C. Dong, C. Shek. Bulk metallic glasses, Materials Science and Engineering: R: Reports 44 (2004) 45-89.

[30]S. Ashley. Metallic glasses bulk up, Mechanical Engineering 120 (1998) 72.

[31]E. Hand. The solar system's first breath, Nature 452 (2008) 259-259.

[32]A. Sypien, M. Stoica, T. Czeppe. Properties of the Ti40Zr10Cu36Pd14 BMG modified by Sn and Nb additions, Journal of Materials Engineering and Performance 25 (2016) 800-808.

[33]H. Sheng, W. Luo, F. Alamgir, J. Bai, E. Ma. Atomic packing and short-to-medium-range order in metallic glasses, Nature 439 (2006) 419-425.

[34]Y. Cheng, H. Sheng, E. Ma. Relationship between structure, dynamics, and mechanical properties in metallic glass-forming alloys, Physical Review B 78 (2008) 014207.

[35]Y. Cheng, E. Ma, H. Sheng. Atomic level structure in multicomponent bulk metallic glass, Physical Review Letters 102 (2009) 245501.

[36]Y. Cheng, A. Cao, E. Ma. Correlation between the elastic modulus and the intrinsic plastic behavior of metallic glasses: The roles of atomic configuration and alloy composition, Acta Materialia 57 (2009) 3253-3267.

[37]M. Li, C. Wang, S. Hao, M. Kramer, K. Ho. Structural heterogeneity and medium-range order in Zr x Cu 100− x metallic glasses, Physical Review B 80 (2009) 184201.

[38]W. Luo, H. Sheng, F. Alamgir, J. Bai, J. He, E. Ma. Icosahedral short-range

order in amorphous alloys, Physical Review Letters 92 (2004) 145502.

[39]N. Mattern, P. Jóvári, I. Kaban, S. Gruner, A. Elsner, V. Kokotin, H. Franz, B. Beuneu, J. Eckert. Short-range order of Cu–Zr metallic glasses, Journal of Alloys and Compounds 485 (2009) 163-169.

[40]A. Hirata, P. Guan, T. Fujita, Y. Hirotsu, A. Inoue, A.R. Yavari, T. Sakurai, M. Chen. Direct observation of local atomic order in a metallic glass, Nature Materials 10 (2011) 28-33.

[41]P. Gaskell. A new structural model for transition metal–metalloid glasses, Nature 276 (1978) 484-485.

[42]J.D. Bernal. A geometrical approach to the structure of liquids, Nature 183 (1959).

[43]D. Miracle. The efficient cluster packing model–An atomic structural model for metallic glasses, Acta Materialia 54 (2006) 4317-4336.

[44]P. Gaskell. Similarities in amorphous and crystalline transition metal–metalloid alloy structures, (1981).

[45]D. Miracle, W. Sanders, O. Senkov. The influence of efficient atomic packing on the constitution of metallic glasses, Philosophical Magazine 83 (2003) 2409-2428.

[46]D.B. Miracle. A structural model for metallic glasses, Nature Materials 3 (2004) 697-702.

[47]D. Adams, A. Matheson. Computation of dense random packings of hard spheres, The Journal of Chemical Physics 56 (1972) 1989-1994.

[48]J.L. Finney. Random packings and the structure of simple liquids. I. The geometry of random close packing, Proceedings Of the Royal Society Of London Series a-Mathematical And Physical Sciences 319 (1970) 479-493.

[49]D. Miracle. Efficient local packing in metallic glasses, Journal of Non-Crystalline Solids 342 (2004) 89-96.

[50]D.B. Miracle, E.A. Lord, S. Ranganathan. Candidate atomic cluster configurations in metallic glass structures, Materials Transactions 47 (2006) 1737-1742.

[51]D. Wang, Y. Li, B. Sun, M. Sui, K. Lu, E. Ma. Bulk metallic glass formation in the binary Cu–Zr system, Applied Physics Letters 84 (2004) 4029-4031.

[52]D. Xu, B. Lohwongwatana, G. Duan, W.L. Johnson, C. Garland. Bulk metallic glass formation in binary Cu-rich alloy series–Cu 100− x Zr x (x= 34, 36, 38.2, 40 at.%) and mechanical properties of bulk Cu 64 Zr 36 glass, Acta Materialia 52 (2004) 2621-2624.

[53]T. Mei-Bo, Z. De-Qian, P. Ming-Xiang, W. Wei-Hua. Binary Cu–Zr bulk metallic glasses, Chinese Physics Letters 21 (2004) 901.

[54]Z. Altounian, T. Guo‐hua, J. Strom‐Olsen. Crystallization characteristics of Cu‐Zr metallic glasses from Cu70Zr30 to Cu25Zr75, Journal of Applied Physics 53 (1982) 4755-4760.

[55]Y. Calvayrac, J. Chevalier, M. Harmelin, A. Quivy, J. Bigot. On the stability and structure of Cu—Zr based glasses, Philosophical Magazine B 48 (1983) 323-332.

[56]Z. Altounian, J. Strom-Olsen. Superconductivity and spin fluctuations in M− Z r metallic glasses (M= C u, N i, C o, a n d F e), Physical Review B 27 (1983) 4149.

[57]L. Davis, C.-P. Chou, L. Tanner, R. Ray. Strenghts and stiffnesses of metallic glasses, Scripta Metallurgica 10 (1976) 937-940.

[58]Y. Li, Q. Guo, J. Kalb, C. Thompson. Matching glass-forming ability with the density of the amorphous phase, Science 322 (2008) 1816-1819.

[59]N. Mattern, A. Schöps, U. Kühn, J. Acker, O. Khvostikova, J. Eckert. Structural behavior of CuxZr 100− x metallic glass (x= 35− 70), Journal of Non-Crystalline Solids 354 (2008) 1054-1060.

[60]D. Ma, A.D. Stoica, X.-L. Wang, Z. Lu, M. Xu, M. Kramer. Efficient local atomic packing in metallic glasses and its correlation with glass-forming ability, Physical Review B 80 (2009) 014202.

[61]N. Jakse, A. Pasturel. Glass forming ability and short-range order in a binary bulk metallic glass by ab initio molecular dynamics, Applied Physics Letters 93 (2008) 3104.

[62]Y. Cheng, A.J. Cao, H. Sheng, E. Ma. Local order influences initiation of

plastic flow in metallic glass: Effects of alloy composition and sample cooling history, Acta Materialia 56 (2008) 5263-5275.

[63]J.-C. Lee, K.-W. Park, K.-H. Kim, E. Fleury, B.-J. Lee, M. Wakeda, Y. Shibutani. Origin of the plasticity in bulk amorphous alloys, Journal of Materials Research 22 (2007) 3087-3097.

[64]Z. Zhang, G. He, J. Eckert, L. Schultz. Fracture mechanisms in bulk metallic glassy materials, Physical Review Letters 91 (2003) 045505.

[65]A. Inoue, B. Shen, H. Koshiba, H. Kato, A.R. Yavari. Cobalt-based bulk glassy alloy with ultrahigh strength and soft magnetic properties, Nature Materials 2 (2003) 661-663.

[66]Y.H. Liu, G. Wang, R.J. Wang, M.X. Pan, W.H. Wang. Super plastic bulk metallic glasses at room temperature, Science 315 (2007) 1385-1388.

[67]J. Schroers, W.L. Johnson. Ductile bulk metallic glass, Physical Review Letters 93 (2004) 255506.

[68]C. Hays, C. Kim, W. Johnson. Composite formed by precipitation of dendritic ductile intermetallic in metallic glass, Physical Review Letters 84 (2000) 2901-2904.

[69]K. Kim, J. Das, F. Baier, M. Tang, W. Wang, J. Eckert. Heterogeneity of a Cu 47.5 Zr 47.5 Al 5 bulk metallic glass, Applied Physics Letters 88 (2006) 051911.

[70]K. Yao, F. Ruan, Y. Yang, N. Chen. Superductile bulk metallic glass, Applied Physics Letters 88 (2006) 122106.

[71]J. Das, M.B. Tang, K.B. Kim, R. Theissmann, F. Baier, W.H. Wang, J. Eckert. “Work-hardenable” ductile bulk metallic glass, Physical Review Letters 94 (2005) 205501.

[72]L. Chen, Z. Fu, G. Zhang, X. Hao, Q. Jiang, X. Wang, Q. Cao, H. Franz, Y. Liu, H. Xie. New class of plastic bulk metallic glass, Physical Review Letters 100 (2008) 075501.

[73]L. Chen, A. Setyawan, H. Kato, A. Inoue, G. Zhang, J. Saida, X. Wang, Q. Cao, J. Jiang. Free-volume-induced enhancement of plasticity in a monolithic bulk metallic glass at room temperature, Scripta Materialia 59 (2008) 75-78.

[74]C.A. Schuh, T.C. Hufnagel, U. Ramamurty. Overview No.144 - Mechanical behavior of amorphous alloys, Acta Materialia 55 (2007) 4067-4109.

[75]F. Spaepen. A microscopic mechanism for steady state inhomogeneous flow in metallic glasses, Acta Metallurgica 25 (1977) 407-415.

[76]M. Falk, J. Langer. Dynamics of viscoplastic deformation in amorphous solids, Physical Review E 57 (1998) 7192.

[77]S. Mayr. Activation energy of shear transformation zones: a key for understanding rheology of glasses and liquids, Physical Review Letters 97 (2006) 195501.

[78]A. Argon. Plastic deformation in metallic glasses, Acta Metallurgica 27 (1979) 47-58.

[79]J. Langer. Shear-transformation-zone theory of deformation in metallic glasses, Scripta Materialia 54 (2006) 375-379.

[80]C.A. Schuh, T.C. Hufnagel, U. Ramamurty. Mechanical behavior of amorphous alloys, Acta Materialia 55 (2007) 4067-4109.

[81]M.H. Cohen, D. Turnbull. Molecular Transport in Liquids and Glasses, The Journal of Chemical Physics 31 (1959) 1164-1169.

[82]D. Turnbull, M.H. Cohen. Free‐volume model of the amorphous phase: glass transition, The Journal of Chemical Physics 34 (1961) 120-125.

[83]D. Turnbull, M.H. Cohen. On the free‐volume model of the liquid‐glass transition, The Journal of Chemical Physics 52 (1970) 3038-3041.

[84]P. Steif, F. Spaepen, J. Hutchinson. Strain localization in amorphous metals, Acta Metallurgica 30 (1982) 447-455.

[85]M. Heggen, F. Spaepen, M. Feuerbacher. Creation and annihilation of free volume during homogeneous flow of a metallic glass, Journal of Applied Physics 97 (2005) 33506-33506.

[86]A. Van den Beukel, J. Sietsma. The glass transition as a free volume related kinetic phenomenon, Acta Metallurgica Et Materialia 38 (1990) 383-389.

[87]F. Spaepen. Microscopic mechanism for steady-state inhomogeneous flow

in metallic glasses, Acta Metallurgica 25 (1977) 407-415.

[88]P.A. Duine, J. Sietsma, A. Van den Beukel. Defect production and annihilation near equilibrium in amorphous Pd 40 Ni 40 P 20 investigated from viscosity data, Acta Metallurgica et Materialia 40 (1992) 743-751.

[89]H. Jin, X. Gu, P. Wen, L. Wang, K. Lu. Pressure effect on the structural relaxation and glass transition in metallic glasses, Acta Materialia 51 (2003) 6219-6231.

[90]F. Faupel, W. Frank, M.-P. Macht, H. Mehrer, V. Naundorf, K. Rätzke, H.R. Schober, S.K. Sharma, H. Teichler. Diffusion in metallic glasses and supercooled melts, Reviews of Modern Physics 75 (2003) 237.

[91]H. Schober. Pressure dependence of diffusion in simple glasses and supercooled liquids, Physical Review Letters 88 (2002) 145901.

[92]T. Nieh, J. Wadsworth, C. Liu, T. Ohkubo, Y. Hirotsu. Plasticity and structural instability in a bulk metallic glass deformed in the supercooled liquid region, Acta Materialia 49 (2001) 2887-2896.

[93]M. Bletry, P. Guyot, J.-J. Blandin, J.-L. Soubeyroux. Free volume model: High-temperature deformation of a Zr-based bulk metallic glass, Acta Materialia 54 (2006) 1257-1263.

[94]G.a. Ruitenberg, P. De Hey, F. Sommer, J. Sietsma. Pressure-induced structural relaxation in amorphous Pd 40 Ni 40 P 20: The formation volume for diffusion defects, Physical Review Letters 79 (1997) 4830.

[95]H. Mehrer. Diffusion in solids: fundamentals, methods, materials, diffusion-controlled processes, Springer Science & Business Media, 2007.

[96]M.J. Aziz, P.C. Sabin, G.-Q. Lu. The activation strain tensor: nonhydrostatic stress effects on crystal-growth kinetics, Physical Review B 44 (1991) 9812.

[97]Z.T. Wang, J. Pan, Y. Li, C.A. Schuh. Densification and strain hardening of a metallic glass under tension at room temperature, Physical Review Letters 111 (2013).

[98]H. Neuber. Theory of notch stresses: Principles for exact stress calculation, JW Edwards, 1946.

[99]C. Nagel, K. Rätzke, E. Schmidtke, J. Wolff, U. Geyer, F. Faupel. Free-volume changes in the bulk metallic glass Zr 46.7 Ti 8.3 Cu 7.5 Ni 10 Be 27.5 and the undercooled liquid, Physical Review B 57 (1998) 10224.

[100] P. Donovan, R. Cochrane. Deformation-induced microcracking in Pd 40 Ni 40 P 20 metallic glass, Scripta Metallurgica 22 (1988) 1765-1770.

[101] C. Nagel, K. Rätzke, E. Schmidtke, F. Faupel, W. Ulfert. Positron-annihilation studies of free-volume changes in the bulk metallic glass Zr 65 Al 7.5 Ni 10 Cu 17.5 during structural relaxation and at the glass transition, Physical Review B 60 (1999) 9212.

[102] K.M. Flores, B.P. Kanungo, S.C. Glade, P. Asoka-Kumar. Characterization of plasticity-induced structural changes in a Zr-based bulk metallic glass using positron annihilation spectroscopy, Journal of Non-Crystalline Solids 353 (2007) 1201-1207.

[103] C.A. Pampillo. Flow and fracture in amorphous alloys, Journal of Materials Science 10 (1975) 1194-1227.

[104] Q.K. Li, M. Li. Atomic scale characterization of shear bands in an amorphous metal, Applied Physics Letters 88 (2006).

[105] Y. Cheng, E. Ma. Indicators of internal structural states for metallic glasses: Local order, free volume, and configurational potential energy, Applied Physics Letters 93 (2008) 051910.

[106] D. Chen, X. Gu, Q. An, W. Goddard III, J. Greer. Ductility and work hardening in nano-sized metallic glasses, Applied Physics Letters 106 (2015) 061903.

[107] S. Adibi, P.S. Branicio, Y.-W. Zhang, S.P. Joshi. Composition and grain size effects on the structural and mechanical properties of CuZr nanoglasses, Journal of Applied Physics 116 (2014) 043522.

[108] A. Cao, Y. Cheng, E. Ma. Structural processes that initiate shear localization in metallic glass, Acta Materialia 57 (2009) 5146-5155.

[109] Q.K. Li, M. Li. Atomistic simulations of correlations between volumetric change and shear softening in amorphous metals, Physical Review B 75 (2007) 5.

[110] Y. Ritter, K. Albe. Chemical and topological order in shear bands of Cu64Zr36 and Cu36Zr64 glasses, Journal of Applied Physics 111 (2012) 103527.

[111] W.J. Wright, T. Hufnagel, W. Nix. Free volume coalescence and void formation in shear bands in metallic glass, Journal of Applied Physics 93 (2003) 1432-1437.

[112] M. Launey, R. Busch, J. Kruzic. Effects of free volume changes and residual stresses on the fatigue and fracture behavior of a Zr–Ti–Ni–Cu–Be bulk metallic glass, Acta Materialia 56 (2008) 500-510.

[113] R. Bhowmick, R. Raghavan, K. Chattopadhyay, U. Ramamurty. Plastic flow softening in a bulk metallic glass, Acta Materialia 54 (2006) 4221-4228.

[114] X. Zeng, Q. Hu, M. Fu, S. Xie. Investigation of the free volume change of Fe 41 Co 7 Cr 15 Mo 14 C 15 B 6 Y 2 bulk metallic glass using the cyclic thermal dilatation test, Journal of Non-Crystalline Solids 358 (2012) 2682-2686.

[115] K. Flores, D. Suh, R. Dauskardt, P. Asoka-Kumar, P. Sterne, R. Howell. Characterization of free volume in a bulk metallic glass using positron annihilation spectroscopy, Journal of Materials Research 17 (2002) 1153-1161.

[116] L. Liu, L. Dai, Y. Bai, B. Wei. Initiation and propagation of shear bands in Zr-based bulk metallic glass under quasi-static and dynamic shear loadings, Journal of Non-Crystalline Solids 351 (2005) 3259-3270.

[117] H.A. Bruck, A.J. Rosakis, W.L. Johnson. The dynamic compressive behavior of beryllium bearing bulk metallic glasses, Journal of Materials Research 11 (1996) 503-511.

[118] G. Subhash, R.J. Dowding, L.J. Kecskes. Characterization of uniaxial compressive response of bulk amorphous Zr–Ti–Cu–Ni–Be alloy, Materials Science and Engineering: A 334 (2002) 33-40.

[119] L. Liu, L. Dai, Y. Bai, B. Wei, G. Yu. Strain rate-dependent compressive deformation behavior of Nd-based bulk metallic glass, Intermetallics 13 (2005) 827-832.

[120] Y. Kawamura, T. Shibata, A. Inoue, T. Masumoto. Superplastic deformation of Zr 65 Al 10 Ni 10 Cu 15 metallic glass, Scripta Materialia 37 (1997) 431-436.

[121] J. Zhang, J.M. Park, D.H. Kim, H.S. Kim. Effect of strain rate on compressive behavior of Ti 45 Zr 16 Ni 9 Cu 10 Be 20 bulk metallic glass, Materials Science and Engineering: A 449 (2007) 290-294.

[122] W. Ma, H. Kou, J. Li, H. Chang, L. Zhou. Effect of strain rate on compressive behavior of Ti-based bulk metallic glass at room temperature, Journal of Alloys and Compounds 472 (2009) 214-218.

[123] T. Mukai, T. Nieh, Y. Kawamura, A. Inoue, K. Higashi. Effect of strain rate on compressive behavior of a Pd 40 Ni 40 P 20 bulk metallic glass, Intermetallics 10 (2002) 1071-1077.

[124] H. Li, G. Subhash, X.-L. Gao, L.J. Kecskes, R.J. Dowding. Negative strain rate sensitivity and compositional dependence of fracture strength in Zr/Hf based bulk metallic glasses, Scripta Materialia 49 (2003) 1087-1092.

[125] H. Li, G. Subhash, L.J. Kecskes, R.J. Dowding. Mechanical behavior of tungsten preform reinforced bulk metallic glass composites, Materials Science and Engineering: A 403 (2005) 134-143.

[126] F.H. Dalla Torre, A. Dubach, M.E. Siegrist, J.F. Löffler. Negative strain rate sensitivity in bulk metallic glass and its similarities with the dynamic strain aging effect during deformation, Applied Physics Letters 89 (2006) 091918.

[127] T. Hufnagel, T. Jiao, Y. Li, L. Xing, K. Ramesh. Deformation and failure of Zr 57 Ti 5 Cu 20 Ni 8 Al 10 bulk metallic glass under quasi-static and dynamic compression, Journal of Materials Research 17 (2002) 1441-1445.

[128] X. Gu, T. Jiao, L. Kecskes, R. Woodman, C. Fan, K. Ramesh, T. Hufnagel. Crystallization and mechanical behavior of (Hf, Zr)–Ti–Cu–Ni–Al metallic glasses, Journal of Non-Crystalline Solids 317 (2003) 112-117.

[129] T. Masumoto, R. Maddin. The mechanical properties of palladium 20 a/o silicon alloy quenched from the liquid state, Acta Metallurgica 19 (1971) 725-741.

[130] T. Mukai, T. Nieh, Y. Kawamura, A. Inoue, K. Higashi. Dynamic response of a Pd 40 Ni 40 P 20 bulk metallic glass in tension, Scripta Materialia 46 (2002) 43-47.

[131] J.-f. Sun, M. Yan, J. Shen. High strain rate induced embrittlement of Zr-based bulk metallic glass, Transactions of Nonferrous Metals Society of

China 15 (2005) 115.

[132] A. Sergueeva, N. Mara, J. Kuntz, D. Branagan, A. Mukherjee. Shear band formation and ductility of metallic glasses, Materials Science and Engineering: A 383 (2004) 219-223.

[133] Y. Xue, H. Cai, L. Wang, F. Wang, H. Zhang. Effect of loading rate on failure in Zr-based bulk metallic glass, Materials Science and Engineering: A 473 (2008) 105-110.

[134] Y. Cheng, E. Ma. Intrinsic shear strength of metallic glass, Acta Materialia 59 (2011) 1800-1807.

[135] W. Johnson, K. Samwer. A universal criterion for plastic yielding of metallic glasses with a (T/T g) 2/3 temperature dependence, Physical Review Letters 95 (2005) 195501.

[136] J.S. Harmon, M.D. Demetriou, W.L. Johnson, K. Samwer. Anelastic to plastic transition in metallic glass-forming liquids, Physical Review Letters 99 (2007) 135502.

[137] P. Guan, M. Chen, T. Egami. Stress-temperature scaling for steady-state flow in metallic glasses, Physical Review Letters 104 (2010) 205701.

[138] J. Rottler, M.O. Robbins. Shear yielding of amorphous glassy solids: Effect of temperature and strain rate, Physical Review E 68 (2003) 011507.

[139] K.S. Lee, T.K. Ha, S. Ahn, Y.W. Chang. High temperature deformation behavior of the Zr 41.2 Ti 13.8 Cu 12.5 Ni 10 Be 22.5 bulk metallic glass, Journal of Non-Crystalline Solids 317 (2003) 193-199.

[140] C. Pampillo, H. Chen. Comprehensive plastic deformation of a bulk metallic glass, Materials Science and Engineering 13 (1974) 181-188.

[141] C.A. Schuh, A.C. Lund, T. Nieh. New regime of homogeneous flow in the deformation map of metallic glasses: elevated temperature nanoindentation experiments and mechanistic modeling, Acta Materialia 52 (2004) 5879-5891.

[142] F.H. Dalla Torre, A. Dubach, J.F. Löffler. Deformation kinetics of Zr-based bulk metallic glasses—Temperature and strain rate influences on shear banding, Journal of Alloys and Compounds 495 (2010) 341-344.

[143] M.M. Trexler, N.N. Thadhani. Mechanical properties of bulk metallic glasses, Progress in Materials Science 55 (2010) 759-839.

[144] V. Yamakov, D. Wolf, S.R. Phillpot, A.K. Mukherjee, H. Gleiter. Dislocation processes in the deformation of nanocrystalline aluminium by molecular-dynamics simulation, Nature Materials 1 (2002) 45-49.

[145] W.F. van Gunsteren, H.J. Berendsen. Computer simulation of molecular dynamics: Methodology, applications, and perspectives in chemistry, Angewandte Chemie International Edition in English 29 (1990) 992-1023.

[146] D.C. Rapaport. The art of molecular dynamics simulation, Cambridge university press, 2004.

[147] K. Binder. Monte Carlo and molecular dynamics simulations in polymer science, Oxford University Press New York, 1995.

[148] G. Duan, D. Xu, Q. Zhang, G. Zhang, T. Cagin, W.L. Johnson, W.A. Goddard III. Molecular dynamics study of the binary Cu 46 Zr 54 metallic glass motivated by experiments: Glass formation and atomic-level structure, Physical Review B 71 (2005) 224208.

[149] Y. Qi, T. Çağın, Y. Kimura, W.A. Goddard III. Molecular-dynamics simulations of glass formation and crystallization in binary liquid metals: Cu-Ag and Cu-Ni, Physical Review B 59 (1999) 3527.

[150] H. Sheng, H. Liu, Y. Cheng, J. Wen, P. Lee, W. Luo, S. Shastri, E. Ma. Polyamorphism in a metallic glass, Nature Materials 6 (2007) 192-197.

[151] E. Fermi, J. Pasta, S. Ulam. Studies of nonlinear problems, Los Alamos Report LA-1940 978 (1955).

[152] B.J. Alder, T. Wainwright. Studies in molecular dynamics. I. General method, The Journal of Chemical Physics 31 (1959) 459-466.

[153] B. Alder, T. Wainwright. Phase transition for a hard sphere system, The Journal of Chemical Physics 27 (1957) 1208.

[154] J. Haile. Molecular dynamics simulation: Elementary methods, Computers in Physics 7 (1993) 625-625.

[155] J.E. Jones. On the determination of molecular fields. I. From the

variation of the viscosity of a gas with temperature. Proceedings of the Royal Society of London A: Mathematical, Physical and Engineering Sciences, vol. 106: The Royal Society, 1924. p.441-462.

[156] J.E. Jones. On the determination of molecular fields. II. From the equation of state of a gas. Proceedings of the Royal Society of London A: Mathematical, Physical and Engineering Sciences, vol. 106: The Royal Society, 1924. p.463-477.

[157] W.K. Liu, E. Karpov, S. Zhang, H. Park. An introduction to computational nanomechanics and materials, Computer Methods in Applied Mechanics and Engineering 193 (2004) 1529-1578.

[158] M.S. Daw, M.I. Baskes. Embedded-atom method: Derivation and application to impurities, surfaces, and other defects in metals, Physical Review B 29 (1984) 6443.

[159] M.S. Daw, M.I. Baskes. Semiempirical, quantum mechanical calculation of hydrogen embrittlement in metals, Physical Review Letters 50 (1983) 1285.

[160] J. Winey, A. Kubota, Y. Gupta. A thermodynamic approach to determine accurate potentials for molecular dynamics simulations: thermoelastic response of aluminum, Modelling and Simulation in Materials Science and Engineering 17 (2009) 055004.

[161] R.R. Zope, Y. Mishin. Interatomic potentials for atomistic simulations of the Ti-Al system, Physical Review B 68 (2003) 024102.

[162] H. Chamati, N. Papanicolaou, Y. Mishin, D. Papaconstantopoulos. Embedded-atom potential for Fe and its application to self-diffusion on Fe (100), Surface Science 600 (2006) 1793-1803.

[163] D. Smirnova, A.Y. Kuksin, S. Starikov, V. Stegailov, Z. Insepov, J. Rest, A. Yacout. A ternary EAM interatomic potential for U–Mo alloys with xenon, Modelling and Simulation in Materials Science and Engineering 21 (2013) 035011.

[164] B.-J. Lee, M. Baskes, H. Kim, Y.K. Cho. Second nearest-neighbor modified embedded atom method potentials for bcc transition metals, Physical Review B 64 (2001) 184102.

[165] Y.F. Ouyang, X. Zhong, X. Tao. A general embedded atom method and application to prediction for thermodynamic properties of Fe-Eu system. Materials Science Forum, vol. 502: Trans Tech Publ, 2005. p.57-62.

[166] M. Finnis, J. Sinclair. A simple empirical N-body potential for transition metals, Philosophical Magazine A 50 (1984) 45-55.

[167] F. Willaime, C. Massobrio. Development of an N-body interatomic potential for hcp and bcc zirconium, Physical Review B 43 (1991) 11653.

[168] F. Ducastelle, F. Cyrot-Lackmann. Moments developments and their application to the electronic charge distribution of d bands, Journal of Physics and Chemistry of Solids 31 (1970) 1295-1306.

[169] F. Cleri, V. Rosato. Tight-binding potentials for transition metals and alloys, Physical Review B 48 (1993) 22.

[170] S. Nosé. A unified formulation of the constant temperature molecular dynamics methods, The Journal of chemical physics 81 (1984) 511-519.

[171] W.G. Hoover. Canonical dynamics: equilibrium phase-space distributions, Physical Review A 31 (1985) 1695.

[172] T.I. Cheatham, J. Miller, T. Fox, T. Darden, P. Kollman. Molecular dynamics simulations on solvated biomolecular systems: the particle mesh Ewald method leads to stable trajectories of DNA, RNA, and proteins, Journal of the American Chemical Society 117 (1995) 4193-4194.

[173] M. Neumann. Dipole moment fluctuation formulas in computer simulations of polar systems, Molecular Physics 50 (1983) 841-858.

[174] See http://lammps.sandia.gov for more information; accessed 21 July 2016.

[175] R. Zallen. The physics of amorphous solids, John Wiley & Sons, 2008.

[176] W. Humphrey, A. Dalke, K. Schulten. VMD: visual molecular dynamics, Journal of Molecular Graphics 14 (1996) 33-38.

[177] F. Shimizu, S. Ogata, J. Li. Theory of shear banding in metallic glasses and molecular dynamics calculations, Materials Transactions 48 (2007) 2923-2927.

[178] G. Voronoï. Nouvelles applications des paramètres continus à la théorie des formes quadratiques. Deuxième mémoire. Recherches sur les parallélloèdres primitifs, Journal für die reine und angewandte Mathematik 134 (1908) 198-287.

[179] W. Brostow, M. Chybicki, R. Laskowski, J. Rybicki. Voronoi polyhedra and Delaunay simplexes in the structural analysis of molecular-dynamics-simulated materials, Physical Review B 57 (1998) 13448.

[180] S. Hao, C. Wang, M. Kramer, K. Ho. Microscopic origin of slow dynamics at the good glass forming composition range in Zr1− xCux metallic liquids, Journal of Applied Physics 107 (2010) 053511.

[181] O. Gedeon, M. Liška. Voronoi polyhedra analysis of MD simulated silicate glasses, Journal of Non-Crystalline Solids 303 (2002) 246-252.

[182] K.-W. Park, J.-i. Jang, M. Wakeda, Y. Shibutani, J.-C. Lee. Atomic packing density and its influence on the properties of Cu–Zr amorphous alloys, Scripta Materialia 57 (2007) 805-808.

[183] C. Rycroft. Voro++: A three-dimensional Voronoi cell library in C++, Lawrence Berkeley National Laboratory (2009).

[184] A. Stukowski. Visualization and analysis of atomistic simulation data with OVITO–the Open Visualization Tool, Modelling and Simulation in Materials Science and Engineering 18 (2009) 015012.

[185] M. Segall, P. Linda, M. Probert, C. Pickard, P. Hasnip, S. Clark, M. Payne. Materials studio CASTEP, version 2.2, Accelrys: San Diego, CA (2002).

[186] J. Li. AtomEye: an efficient atomistic configuration viewer, Modelling and Simulation in Materials Science and Engineering 11 (2003) 173.

[187] S.-W. Lee, S.-C. Lee, Y.-C. Kim, E. Fleury, J.-C. Lee. Design of a bulk amorphous alloy containing Cu–Zr with simultaneous improvement in glass-forming ability and plasticity, Journal of Materials Research 22 (2007) 486-492.

[188] X. Cui, F.Q. Zu, W.J. Zhang, Z.Z. Wang, X.Y. Li. Phase competition of Cu64Zr36 and its effect on glass forming ability of the alloy, Crystal Research and Technology 48 (2013) 11-15.

[189] A.R. Yavari, A. Inoue. Volume effects in bulk metallic glass formation. MRS Proceedings, vol. 554: Cambridge Univ Press, 1998. p.21.

[190] J. Finney. Modelling the structures of amorphous metals and alloys, Nature 266 (1977) 309-314.

[191] X.J. Liu, Y. Xu, X. Hui, Z.P. Lu, F. Li, G.L. Chen, J. Lu, C.T. Liu. Metallic liquids and glasses: atomic order and global packing, Physical Review Letters 105 (2010).

[192] F. Frank. Supercooling of liquids, Proceedings of the Royal Society of London. Series A, Mathematical and Physical Sciences 215 (1952) 43-46.

[193] Y. Waseda, T. Egami. Effect of low-temperature annealing and deformation on the structure of metallic glasses by X-ray diffraction, Journal of Materials Science 14 (1979) 1249-1253.

[194] D. Srolovitz, T. Egami, V. Vitek. Radial distribution function and structural relaxation in amorphous solids, Physical Review B 24 (1981) 6936.

[195] W. Dmowski, C. Fan, M. Morrison, P. Liaw, T. Egami. Structural changes in bulk metallic glass after annealing below the glass-transition temperature, Materials Science and Engineering: A 471 (2007) 125-129.

[196] K. Samwer, J. Lasjaunias. On the structure of amorphous sputtered Zr 76 Cu 24 alloy, Solid State Communications 51 (1984) 93-96.

[197] Y. Ritter. Molecular dynamics simulations of structure-property relationships in Cu-Zr metallic glasses, (2012).

[198] C. Hays, C. Kim, W.L. Johnson. Microstructure controlled shear band pattern formation and enhanced plasticity of bulk metallic glasses containing in situ formed ductile phase dendrite dispersions, Physical Review Letters 84 (2000) 2901.

[199] M. Zink, K. Samwer, W. Johnson, S. Mayr. Plastic deformation of metallic glasses: size of shear transformation zones from molecular dynamics simulations, Physical Review B 73 (2006) 172203.

[200] S. Pauly, S. Gorantla, G. Wang, U. Kühn, J. Eckert. Transformation-mediated ductility in CuZr-based bulk metallic glasses, Nature Materials 9 (2010) 473-477.

[201] H. Peng, M. Li, W. Wang. Structural signature of plastic deformation in metallic glasses, Physical Review Letters 106 (2011) 135503.

[202] D. Şopu, Y. Ritter, H. Gleiter, K. Albe. Deformation behavior of bulk and nanostructured metallic glasses studied via molecular dynamics simulations, Physical Review B 83 (2011) 100202.

[203] Z.D. Sha, L.C. He, S. Xu, Q.X. Pei, Z.S. Liu, Y.W. Zhang, T.J. Wang. Effect of aspect ratio on the mechanical properties of metallic glasses, Scripta Materialia 93 (2014) 36-39.

[204] J.X. Zhao, R.T. Qu, F.F. Wu, S.X. Li, Z.F. Zhang. Deformation behavior and enhanced plasticity of Ti-based metallic glasses with notches, Philosophical Magazine 90 (2010) 3867-3877.

[205] Y. Ritter, D. Şopu, H. Gleiter, K. Albe. Structure, stability and mechanical properties of internal interfaces in Cu 64 Zr 36 nanoglasses studied by MD simulations, Acta Materialia 59 (2011) 6588-6593.

[206] P.W. Bridgman. Studies in large plastic flow and fracture, McGraw-Hill New York, 1952.

[207] K. Flores, R. Dauskardt. Mean stress effects on flow localization and failure in a bulk metallic glass, Acta Materialia 49 (2001) 2527-2537.

[208] A. Cao, E. Ma. Sample shape and temperature strongly influence the yield strength of metallic nanopillars, Acta Materialia 56 (2008) 4816-4828.

[209] Z. Shan, J. Li, Y. Cheng, A. Minor, S.S. Asif, O. Warren, E. Ma. Plastic flow and failure resistance of metallic glass: Insight from in situ compression of nanopillars, Physical Review B 77 (2008) 155419.

[210] D. Jang, J.R. Greer. Transition from a strong-yet-brittle to a stronger-and-ductile state by size reduction of metallic glasses, Nature Materials 9 (2010) 215-219.

[211] Q. Deng, Y. Cheng, Y. Yue, L. Zhang, Z. Zhang, X. Han, E. Ma. Uniform tensile elongation in framed submicron metallic glass specimen in the limit of suppressed shear banding, Acta Materialia 59 (2011) 6511-6518.

[212] D. Chen, D. Jang, K. Guan, Q. An, W. Goddard III, J. Greer. Nanometallic glasses: size reduction brings ductility, surface state drives its

extent, Nano letters 13 (2013) 4462-4468.

[213] J. Luo, F. Wu, J. Huang, J. Wang, S. Mao. Superelongation and atomic chain formation in nanosized metallic glass, Physical Review Letters 104 (2010) 215503.

[214] C.Q. Chen, Y.T. Pei, O. Kuzmin, Z.F. Zhang, E. Ma, J.T.M. De Hosson. Intrinsic size effects in the mechanical response of taper-free nanopillars of metallic glass, Physical Review B 83 (2011) 180201.

[215] A. Bharathula, S.-W. Lee, W.J. Wright, K.M. Flores. Compression testing of metallic glass at small length scales: Effects on deformation mode and stability, Acta Materialia 58 (2010) 5789-5796.

[216] A. Yavari, K. Georgarakis, W. Botta, A. Inoue, G. Vaughan. Homogenization of plastic deformation in metallic glass foils less than one micrometer thick, Physical Review B 82 (2010) 172202.

[217] J. Pan, H. Zhou, Z. Wang, Y. Li, H. Gao. Origin of anomalous inverse notch effect in bulk metallic glasses, Journal of the Mechanics and Physics of Solids 84 (2015) 85-94.

[218] G.I. Barenblatt. The mathematical theory of equilibrium cracks in brittle fracture, Advances in applied mechanics 7 (1962) 55-129.

[219] Z.-D. Sha, Q.-X. Pei, V. Sorkin, P.S. Branicio, Y.-W. Zhang, H. Gao. On the notch sensitivity of CuZr metallic glasses, Applied Physics Letters 103 (2013) 081903.

[220] P. Bridgman, I. Šimon. Effects of very high pressures on glass, Journal of Applied Physics 24 (1953) 405-413.

[221] T. Rouxel, H. Ji, T. Hammouda, A. Moréac. Poisson's ratio and the densification of glass under high pressure, Physical Review Letters 100 (2008) 225501.

[222] A.D. Drozdov. Stress‐induced densification of glassy polymers in the subyield region, Journal of Applied Polymer Science 74 (1999) 1705-1718.

[223] J. Ding, Y.-Q. Cheng, E. Ma. Full icosahedra dominate local order in Cu 64 Zr 34 metallic glass and supercooled liquid, Acta Materialia 69 (2014) 343-354.

[224] L. Zhang, Y.-Q. Cheng, A.-J. Cao, J. Xu, E. Ma. Bulk metallic glasses with large plasticity: Composition design from the structural perspective, Acta Materialia 57 (2009) 1154-1164.

[225] M. Lee, C.-M. Lee, K.-R. Lee, E. Ma, J.-C. Lee. Networked interpenetrating connections of icosahedra: Effects on shear transformations in metallic glass, Acta Materialia 59 (2011) 159-170.

[226] Y. Shi, M. Falk. Does metallic glass have a backbone? The role of percolating short range order in strength and failure, Scripta Materialia 54 (2006) 381-386.

[227] J. Lewandowski, A. Greer. Temperature rise at shear bands in metallic glasses, Nature Materials 5 (2006) 15-18.

[228] B. Yang, M.L. Morrison, P.K. Liaw, R.A. Buchanan, G. Wang, C.T. Liu, M. Denda. Dynamic evolution of nanoscale shear bands in a bulk-metallic glass, Applied Physics Letters 86 (2005) 141904.

[229] M.D. Demetriou, J.S. Harmon, M. Tao, G. Duan, K. Samwer, W.L. Johnson. Cooperative shear model for the rheology of glass-forming metallic liquids, Physical Review Letters 97 (2006) 065502.

[230] F.H. Stillinger. A topographic view of supercooled liquids and glass formation, Science 267 (1995) 1935.

[231] W.L. Johnson, M.D. Demetriou, J.S. Harmon, M.L. Lind, K. Samwer. Rheology and ultrasonic properties of metallic glass-forming liquids: A potential energy landscape perspective, MRS Bulletin 32 (2007) 644-650.

[232] J. Ding, Y.Q. Cheng, E. Ma. Quantitative measure of local solidity/liquidity in metallic glasses, Acta Materialia 61 (2013) 4474-4480.

[233] D.L. Henann, L. Anand. A large strain isotropic elasticity model based on molecular dynamics simulations of a metallic glass, Journal of Elasticity 104 (2011) 281-302.

[234] Q. Zhang, Q.-K. Li, M. Li. Internal stress and its effect on mechanical strength of metallic glass nanowires, Acta Materialia 91 (2015) 174-182.

[235] W.J. Wright, R.B. Schwarz, W.D. Nix. Localized heating during serrated plastic flow in bulk metallic glasses, Materials Science and Engineering:

A 319 (2001) 229-232.

[236] J. Li, G. Shan, K. Gao, L. Qiao, W. Chu. In situ SEM study of formation and growth of shear bands and microcracks in bulk metallic glasses, Materials Science and Engineering: A 354 (2003) 337-343.

[237] T.J. Rupert. Strain localization in a nanocrystalline metal: Atomic mechanisms and the effect of testing conditions, Journal of Applied Physics 114 (2013) 033527.

[238] Y.-H. Wen, Z.-Z. Zhu, R.-Z. Zhu. Molecular dynamics study of the mechanical behavior of nickel nanowire: Strain rate effects, Computational Materials Science 41 (2008) 553-560.

[239] S. Koh, H. Lee, C. Lu, Q. Cheng. Molecular dynamics simulation of a solid platinum nanowire under uniaxial tensile strain: Temperature and strain-rate effects, Physical Review B 72 (2005) 085414.